

# Exchange Bias in Ferro-/Antiferromagnetic Bilayers

ausgeführt am Institut für  
Festkörperphysik  
der Technischen Universität Wien

unter der Anleitung von  
Univ.Doiz. Dipl.Ing. Dr.techn. Thomas Schrefl

durch

Markus Kirschner  
Angergasse 61  
7123 Mönchhof  
Matr.Nr. 9525261

Wien, am 30. Jänner 2003

---

# Abstract

In this work a granular model for exchange bias of ferro-/antiferromagnetic bilayers for the investigation of magnetization processes on a mesoscopic length scale is presented. The model assumes  $90^\circ$  or spin flop coupling at interfaces perfectly compensated on an atomic scale. The antiferromagnetic grains with randomly distributed easy directions are treated as single domain particles, justified by the finite element approach for rather thin antiferromagnetic films. A Monte Carlo algorithm was used to simulate the field cooling process. The mechanism leading to the hysteresis shift is similar to that proposed by Malozemoff, but the presented interacting grain model describes both coercivity and exchange bias by domain walls localized between antiferromagnetic grains. Changes in the antiferromagnetic domain structure during the reversal of the ferromagnet directly account for the hysteresis shift. The antiferromagnetic intergrain exchange coupling is therefore necessary to obtain exchange bias because it suppresses the out-of-plane rotation of antiferromagnetic spins. The results are strictly valid only for weak intergrain exchange coupling so that the assumption of uniformly magnetized antiferromagnetic grains is fulfilled.

It will be pointed out that the relatively simple interacting grain model can be used to quantify exchange bias and coercivity with predicted magnitudes of an order comparable to those observed experimentally. The dependencies of the bias field on the film thicknesses are in excellent agreement with experimental data. Furthermore, the behavior of the hysteresis shift and the coercive field for varying system parameters, such as the exchange stiffness and anisotropy constants, are discussed. For certain material parameters extremely stable  $360^\circ$  domain walls appeared within the ferromagnet in accordance with experimental observations.

Due to the fact that several experimental samples show on average a preferred orientation of the antiferromagnetic easy directions, simulations of bilayers with textured antiferromagnetic films were performed. The maximum bias field shifts towards lower antiferromagnetic thicknesses for textured films compared with untextured antiferromagnets. This is confirmed by experimental data.

# Kurzfassung

In dieser Diplomarbeit wird ein granulares Modell zur Erklärung des Exchange Bias-Effektes in ferro-/antiferromagnetischen Schichtsystemen diskutiert. Das vorgestellte Modell erlaubt die Untersuchung von Magnetisierungsprozessen auf einer mesoskopischen Längenskala. Es setzt  $90^\circ$ - oder Spin-flop-Kopplung an Zwischenschichten voraus, die auf einer mikroskopischen Ebene perfekt kompensiert sind. Die antiferromagnetischen Körner mit zufällig verteilten leichten Richtungen weisen eine homogene Magnetisierung auf. Die letzte Annahme ist für eher dünne antiferromagnetische Filme gültig und wird durch Berechnungen gerechtfertigt, die auf der Methode der finiten Elemente basieren. Das Kühlen des Schichtsystems in einem äußeren Magnetfeld wird durch einen Monte Carlo Algorithmus simuliert. Der Mechanismus, der zu der Verschiebung der Hystereseschleife führt, ähnelt dem von Malozemoff mit dem Unterschied, dass Koerzitivfeldstärke und Exchange Bias durch Domänenwände zwischen den antiferromagnetischen Körnern erklärt werden. Der Grund für die Verschiebung der Magnetisierungskurve sind Veränderungen in der antiferromagnetischen Domänenstruktur während des Ummagnetisierungsprozesses des Ferromagneten. Voraussetzung für Exchange Bias ist eine intergranuläre Austauschkopplung im Antiferromagneten, da diese die notwendigen Umklappprozesse antiferromagnetischer Spins erst ermöglicht. Die intergranuläre Kopplung muss aber schwach sein, um die Annahme der homogen magnetisierten antiferromagnetischen Körner zu rechtfertigen.

In der vorliegenden Arbeit wird gezeigt, dass das relativ einfache granulare Modell in der Lage ist, Bias-Felder und Koerzitivfeldstärken in der richtigen Größenordnung zu liefern. Die Verschiebung der Hysterese in Abhängigkeit von den Schichtdicken stimmt sehr gut mit experimentell gefundenen Daten überein. Weiters wird das Verhalten des Bias-Feldes und der Koerzitivfeldstärke als Funktion der verschiedenen Systemparameter, wie z.B. der Austausch- und Anisotropiekonstanten, dargestellt. Für bestimmte Materialparameter wurden in Übereinstimmung mit Experimenten extrem stabile  $360^\circ$ -Domänenwände im Ferromagneten gefunden.

Da die leichten Richtungen der antiferromagnetischen Schicht in realen Proben oft eine bestimmte Vorzugsorientierung zeigen (textured films), wurden auch entsprechende Simu-

lationen durchgeführt. Ein Vergleich der Ergebnisse mit jenen für Schichtsysteme mit zufällig verteilten leichten Richtungen zeigt eine Verschiebung des maximalen Bias-Feldes hin zu kleineren antiferromagnetischen Filmdicken. Dieses Resultat wird von experimentellen Ergebnissen bestätigt.

# Danksagung

Ich möchte mich bei Prof. Josef Fidler und Doz. Thomas Schrefl und allen anderen Mitgliedern der Arbeitsgruppe für Mikromagnetismus für das ausgezeichnete Arbeitsklima und die keineswegs selbstverständliche Hilfsbereitschaft bedanken. Mein Betreuer Thomas Schrefl war stets eine Quelle für neue Ideen und nahm sich immer Zeit, um meine Fragen zu beantworten. Bei Problemen mit dem Computer konnte ich mir sicher sein, von Werner Scholz mit seinen fundierten Kenntnissen eine passende Lösung zu bekommen. Dieter Süss danke ich dafür, dass ich auf seiner Arbeit über Exchange Bias aufbauen durfte.

Im Rahmen meiner Diplomarbeit hatte ich die großartige Gelegenheit, zusammen mit Josef Fidler, Thomas Schrefl und Rok Dittrich an der MMM'02-Konferenz in Tampa/Florida teilzunehmen. Dafür möchte ich mich nochmals herzlich bedanken.

Meinen Eltern und meiner Freundin Regina möchte ich dafür danken, dass sie immer für mich da sind.

# Contents

|   |           |
|---|-----------|
| <b>Abstract</b>   | <b>2</b>  |
| <b>Kurzfassung</b>  | <b>3</b>  |
| <b>Danksagung</b>   | <b>5</b>  |
| <b>Introduction</b>   | <b>8</b>  |
| <b>1 Basics of Magnetism</b>  | <b>11</b> |
| 1.1 Maxwell's Equations of Magnetostatics . . . . .                       | 11        |
| 1.2 Gibbs Free Energy . . . . .   | 12        |
| 1.2.1 Exchange Energy . . . . .   | 13        |
| 1.2.2 Magnetocrystalline Anisotropy Energy . . . . .                      | 13        |
| 1.2.3 Strayfield Energy or Magnetic Self Energy . . . . .                 | 14        |
| 1.2.4 Magnetic Field Energy or Zeeman Energy . . . . .                    | 15        |
| 1.3 Landau-Lifshitz-Gilbert Equation . . . . .                            | 16        |
| <b>2 Exchange Bias – an Overview</b>                                      | <b>18</b> |
| 2.1 Introduction . . . . .  | 18        |
| 2.2 Meiklejohn and Bean and their Intuitive Picture . . . . .             | 20        |
| 2.3 Domain Wall Model of Mauri . . . . .                                  | 22        |
| 2.4 Malozemoff's Random Field Model . . . . .                             | 24        |
| 2.5 Koon's Spin Flop Coupling at Compensated Interfaces . . . . .         | 25        |
| 2.6 Polycrystalline Antiferromagnets of Stiles and<br>McMichael . . . . . | 26        |
| <b>3 Interacting Grain Model</b>  | <b>29</b> |
| 3.1 Introduction . . . . .  | 29        |
| 3.2 The Model . . . . .   | 29        |
| 3.3 Implementation . . . . .  | 36        |

|          |  |           |
|----------|--|-----------|
| <b>4</b> | <b>Results of the Interacting Grain Model</b>                  | <b>39</b> |
| 4.1      | Conventions and Methods . . . . .                              | 39        |
| 4.1.1    | Magnetization States . . . . .                                 | 39        |
| 4.1.2    | Irreversible Switching . . . . .                               | 39        |
| 4.1.3    | Centerline of the Hysteresis Cycle . . . . .                   | 41        |
| 4.1.4    | Designation of the Bias Fields . . . . .                       | 44        |
| 4.2      | Results for the Standard Parameters . . . . .                  | 44        |
| 4.2.1    | Hysteresis . . . . .   | 44        |
| 4.2.2    | Energy terms . . . . .   | 46        |
| 4.2.3    | Magnetization Configuration . . . . .                          | 51        |
| 4.3      | Variation of Parameters . . . . .                              | 57        |
| 4.3.1    | Exchange Constant of the Ferromagnet . . . . .                 | 57        |
| 4.3.2    | Thickness of the Ferromagnet . . . . .                         | 62        |
| 4.3.3    | Exchange Constant of the Antiferromagnet . . . . .             | 66        |
| 4.3.4    | Thickness of the Antiferromagnet . . . . .                     | 68        |
| 4.3.5    | Anisotropy Constant of the Antiferromagnet . . . . .           | 73        |
| 4.3.6    | Interface Coupling . . . . .                                   | 74        |
| 4.3.7    | Grain Size . . . . .   | 75        |
| 4.3.8    | Remarks on the Antiferromagnetic Anisotropy . . . . .          | 77        |
| 4.4      | Textured films . . . . .                                       | 78        |
| 4.4.1    | General Aspects of Arbitrarily Distributed Easy Axes . . . . . | 78        |
| 4.4.2    | Uniform and Gaussian Distributions . . . . .                   | 81        |
|          | <b>Outlook</b>   | <b>88</b> |
|          | <b>List of Figures</b>   | <b>89</b> |
|          | <b>Bibliography</b>  | <b>91</b> |
|          | <b>Lebenslauf</b>  | <b>95</b> |

# Introduction

“A new type of magnetic anisotropy has been discovered which is best described as an exchange anisotropy. This anisotropy is the result of an interaction between an antiferromagnetic material and a ferromagnetic material. The material that exhibits this exchange anisotropy is a compact of fine particles of cobalt with a cobaltous oxide shell. The effect occurs only below the Néel temperature of the antiferromagnetic material [...]”

Meiklejohn and Bean, 1956 [21, 22]

In the year 1956 Meiklejohn and Bean studied small Co particles surrounded with the antiferromagnetic oxide CoO [21, 22]. They discovered the phenomena of exchange anisotropy and exchange bias – a shift of the hysteresis loop along the field axis. Usually exchange bias requires that the ferro-/antiferromagnetic bilayer is cooled below the Néel temperature of the antiferromagnet in the presence of an external field. This procedure is called field cooling. The magnetic field needed to switch the ferromagnet from the field cooled state into the reversed state is then larger than the field needed to rotate the ferromagnet back to its original direction. Moreover, such bilayer systems show an enhancement of the coercive field even if no bias occurs.

Since the introduction of giant magnetoresistive (GMR) spin-valve heads in magnetic recording the bias effect has been used widely in modern technology. Commonly used sensors are bilayers of FeMn/FeCo, IrMn/NiFe and IrMn/FeCo [33]. The pinned layer of a spin valve sensor is stabilized due to the coupling to an antiferromagnetic film (see Fig. 1). The spin-valve sensor consists of four metal layers: an antiferromagnetic pinning layer, a pinned layer whose magnetization is fixed due to the pinning effect of the antiferromagnet, a Cu interlayer, and a free layer whose magnetization rotates according to the signal field from the disk media [12]. The electrical resistance of the film is low when the magnetization directions of the pinned layer and the free layer are parallel and high when they are antiparallel.

Despite the application of exchange bias in magnetic field sensors, the physical mechanisms leading to the hysteresis shift are still in discussion. Various theories explain



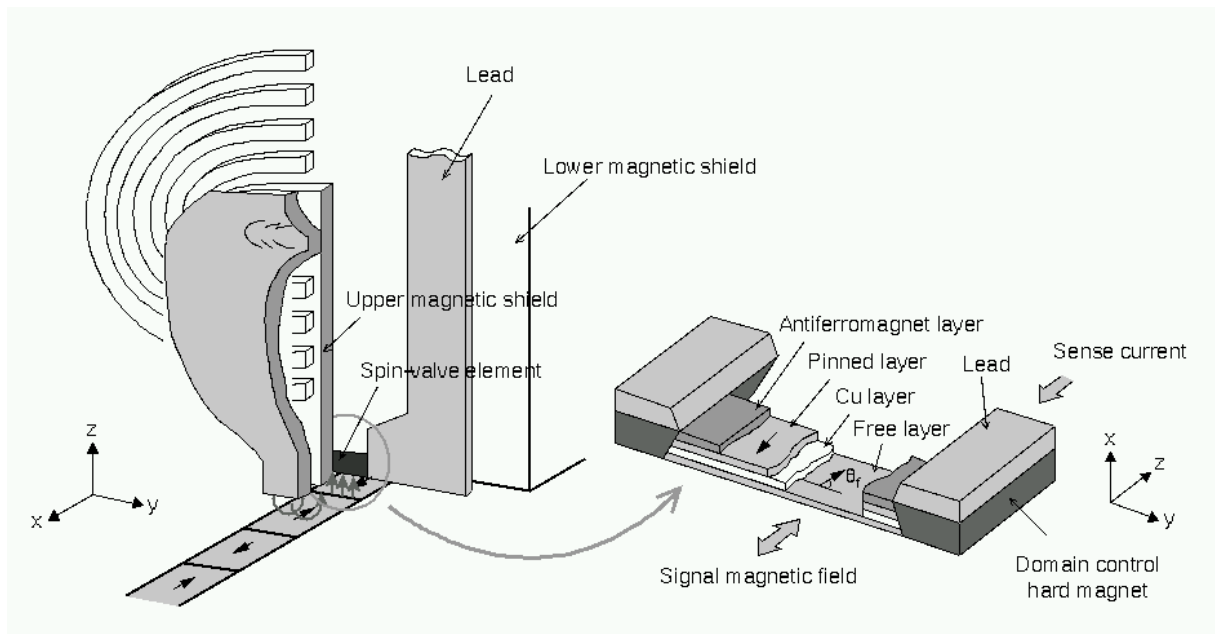


**Figure 1:** Schematic illustration of a giant magnetoresistive (GMR) spin-valve head. From Ref. [12].

particular aspects of the bias effect [1, 27], but nevertheless many issues remain to be solved. One of the most striking experimental fact is the presence of exchange bias at fully compensated interfaces in which the net spin averaged over a microscopic length scale is zero. Intuitively, one might expect that for compensated interfaces the bias effect vanishes as the spins pinning the ferromagnetic layer cancel out each other. Therefore, various models of exchange bias assume at least partly uncompensated interfaces [1].

Originally, Koon [16] proposed a mechanism for exchange bias at fully compensated interfaces. Using an atomistic model, Koon showed that a perfectly compensated interface will lead to a  $90^\circ$  coupling between the antiferromagnet and the ferromagnet because of canted antiferromagnetic spins. Indeed  $90^\circ$  coupling has been observed experimentally [26]. Koon's model is able to explain exchange bias with the assumption that the antiferromagnetic spins are restricted to planes parallel to the interface. The loop shift can be attributed to partial domain walls wound up in the antiferromagnet. Allowing full three dimensional rotations of the antiferromagnetic spins, Schulthess and Butler [29] showed that these domain walls are unstable due to out of plane rotations of the antiferromagnetic spins. They conclude that spin flop coupling at compensated interfaces enhances the coercivity but does not lead to exchange bias. Stiles and McMichael [31] came to a similar conclusion introducing spin flop coupling in their model of polycrystalline films.

Nowak et al. [28] proposed the so-called domain state model for exchange bias. In their

model the antiferromagnet breaks up into domains due to domain wall pinning at random defects. The domains may carry a surplus magnetization. This small net magnetic moment provides coupling across the interface. The authors find exchange bias for directions parallel to the antiferromagnetic anisotropy axis for spins in a single crystal lattice. After a short introduction to the basics of magnetism in Chap. 1, we give a more detailed survey of the developments of exchange bias during the last 40 years in Chap. 2.

In Chap. 3 we discuss the Interacting Grain (IG) model and its implementation. The IG model was proposed by Suess et al. [33] to explain exchange bias at perfectly compensated interfaces with spin flop or  $90^\circ$  coupling between the ferromagnet and the antiferromagnet. The antiferromagnet consists of uniformly magnetized grains with randomly oriented anisotropy directions. In contrast to the model of Stiles and McMichael [31] we assume weak exchange coupling between the grains. The weak intergranular coupling suppresses out-of-plane rotations of the antiferromagnetic moments and provides the wall energy between lateral antiferromagnetic domains. The simulations show that the reversal of the ferromagnet causes the formation of domains within the antiferromagnet. Some of the antiferromagnetic grains switch irreversibly when the ferromagnet reverses, whereas another part of the antiferromagnetic grains remain stable. After reversal of the ferromagnet the system stores energy in antiferromagnetic domain walls perpendicular to the interface, giving rise to the observed loop shift.

The numerical results of Chap. 4 are obtained by solving the Landau-Lifshitz-Gilbert equation and compared with experimental data from recent literature. Contrary to previous theories which require some sort of imperfections to generate exchange bias, we show that bilayers with perfectly compensated interfaces, free of imperfections and defects are also able to show exchange bias.

# Chapter 1

## Basics of Magnetism

### 1.1 Maxwell's Equations of Magnetostatics

Maxwell's equations of magnetostatics can be generally written as (in SI units)

$$\nabla \cdot \mathbf{B} = 0 \quad (1.1)$$

$$\nabla \times \mathbf{B} = \mu_0 \mathbf{j} \quad , \quad (1.2)$$

where  $\mathbf{B}$  is the magnetic induction (or flux density, in T),  $\mu_0 = 4\pi/10^7$  Vs/Am the permeability of free space and  $\mathbf{j}$  the current density (in A/m<sup>2</sup>).

In the presence of matter we have to distinguish between the magnetic induction  $\mathbf{B}_{\text{free}}$  due to free current densities  $\mathbf{j}_{\text{free}}$  and  $\langle \mathbf{B}_{\text{mat}} \rangle$  due to bound current densities  $\langle \mathbf{j}_{\text{mat}} \rangle$ . Quantities in  $\langle \cdot \rangle$  represent the spatial averages. Fluctuations on an atomic length scale are thus not taken into consideration. These quantities satisfy the relations

$$\nabla \cdot \mathbf{B}_{\text{free}} = 0 \quad (1.3)$$

$$\nabla \times \mathbf{B}_{\text{free}} = \mu_0 \mathbf{j}_{\text{free}} \quad (1.4)$$

and

$$\nabla \cdot \langle \mathbf{B}_{\text{mat}} \rangle = 0 \quad (1.5)$$

$$\nabla \times \langle \mathbf{B}_{\text{mat}} \rangle = \mu_0 \langle \mathbf{j}_{\text{mat}} \rangle \quad . \quad (1.6)$$

The total field  $\mathbf{B} = \mathbf{B}_{\text{free}} + \langle \mathbf{B}_{\text{mat}} \rangle$  fulfills the equations

$$\nabla \cdot \mathbf{B} = 0 \quad (1.7)$$

$$\nabla \times \mathbf{B} = \mu_0 \mathbf{j}_{\text{free}} + \mu_0 \langle \mathbf{j}_{\text{mat}} \rangle \quad . \quad (1.8)$$

$\langle \mathbf{j}_{\text{mat}} \rangle$  generates the magnetization  $\mathbf{M}$  (in A/m) within the body, whereas  $\mathbf{M} = 0$  per definition outside. The correlation of both quantities is given by

$$\nabla \times \mathbf{M} = \langle \mathbf{j}_{\text{mat}} \rangle \quad . \quad (1.9)$$

If we define the so-called magnetic field  $\mathbf{H}$  (in A/m)

$$\mathbf{H} = \frac{1}{\mu_0} \mathbf{B} - \mathbf{M} \quad , \quad (1.10)$$

or

$$\mathbf{B} = \mu_0(\mathbf{H} + \mathbf{M}) = \mu_0 \mathbf{H} + \mathbf{J} \quad (1.11)$$

( $\mathbf{J}$  is the magnetic polarization, in T), we obtain Maxwell's macroscopic equations of magnetostatics

$$\nabla \cdot \mathbf{B} = 0 \quad (1.12)$$

$$\nabla \times \mathbf{H} = \mu_0 \mathbf{j}_{\text{free}} \quad . \quad (1.13)$$

The great advantage of these expressions is that the bound current density does not appear anymore.

For the important case of no free current densities, the remaining Maxwell's equations are

$$\nabla \cdot \mathbf{B} = 0 \quad (1.14)$$

$$\nabla \times \mathbf{H} = 0 \quad . \quad (1.15)$$

## 1.2 Gibbs Free Energy

The Gibbs free energy  $E$  of the system must be a minimum during an isothermal and isobaric changing of the magnetization state in a constant external field. Therefore, the state of the magnetic equilibrium can be calculated according to the variation  $\delta E = 0$  (*static* energy minimization proposed by Brown [3]).

When we neglect magnetostrictive effects, there are four important contributions to Gibbs free energy: the exchange energy, the magnetocrystalline anisotropy energy, the strayfield energy, and the Zeeman energy in an external field. So, Gibbs free energy reads

$$E = E_{\text{ex}} + E_{\text{ani}} + E_{\text{S}} + E_{\text{H}} \quad . \quad (1.16)$$

### 1.2.1 Exchange Energy

In the approach of micromagnetics the spin operators are replaced by classical vectors. Therefore, the exchange energy in the Heisenberg model (direct exchange coupling) can be written in the form

$$E_{\text{ex}} = - \sum_{i=1}^N \sum_{j \neq i}^N J^{ij} \mathbf{S}^i \cdot \mathbf{S}^j \quad . \quad (1.17)$$

$J^{ij}$  denotes the exchange integral and can be derived using quantum mechanics. For ferromagnetic ordering the exchange constants are positive.  $\mathbf{S}^i$  and  $\mathbf{S}^j$  are the classical total angular momenta at the lattice sites  $i$  and  $j$ , respectively.

The exchange energy decreases rapidly with increasing distance between the atoms. So, it is usually a good approximation to take the inner sum only for nearest neighbors (n.n.). Supposing an isotropic exchange constant  $J$ , the exchange energy becomes

$$E_{\text{ex}} = -J \sum_{i=1}^N \sum_{j \text{ n.n.}} \mathbf{S}^i \cdot \mathbf{S}^j \quad . \quad (1.18)$$

The exchange energy given in Eq. (1.18) is isotropic in space. That is, the expression is independent of the angles between the spins and the crystal axes. Therefore, additional terms must be taken into account to give a more realistic model.

### 1.2.2 Magnetocrystalline Anisotropy Energy

The energy of interaction between two spins depends on their absolute orientation. The reason for that is the asymmetric overlap of electron density distributions of neighboring lattice sites. Due to spin-orbit coupling the charge density of the electrons is not spherical but reflects the crystal structure of the lattice. This asymmetry and the direction of the magnetization vector are tied together by spin-orbit coupling. Hence, if one changes the spin direction, the overlap energy changes, too. Experimentally, many ferro- and ferri-magnetic materials exhibit easy and hard directions. More energy (or a higher external field) is required to saturate the crystal in a hard direction than in an easy one.

For crystals with *uniaxial anisotropy* (e.g. hexagonal crystals such as Co) the anisotropy energy has the form

$$E_{\text{ani}} = K_0 V + K_1 V \sin^2 \theta \quad + \text{higher order terms} \quad . \quad (1.19)$$

$K_0$  and  $K_1$  are the anisotropy constants (in J/m<sup>3</sup>),  $V$  the volume of the sample and  $\theta$  the angle between the easy direction and the magnetization. The higher order terms (a series of even powers of  $\sin \theta$ ) are often small and thus negligible.

The magnetocrystalline anisotropy energy for *cubic crystals* (Fe, Ni) is given by

$$E_{\text{ani}} = K_{c0}V + K_{c1}V(\alpha_1^2\alpha_2^2 + \alpha_2^2\alpha_3^2 + \alpha_1^2\alpha_3^2) + K_{c2}V\alpha_1^2\alpha_2^2\alpha_3^2 + \text{higher order terms} \quad , \quad (1.20)$$

where  $\alpha_1$ ,  $\alpha_2$  and  $\alpha_3$  designate the direction cosines of the direction of magnetization with respect to the cubic lattice vectors. Analogously,  $K_{c2}$  and higher order terms can be neglected in most cases. Naturally, uniaxial anisotropies are much stronger than cubic ones.

Since the constants  $K_0$  and  $K_{c0}$  add only a constant offset to the energy, they are usually omitted. The remaining first anisotropy constants cover several orders of magnitude ( $10^2$  -  $10^7$  J/m<sup>3</sup>) and are temperature dependent.

### 1.2.3 Strayfield Energy or Magnetic Self Energy

The strayfield energy is connected with the magnetic field generated by the magnetized body itself. Each lattice site is occupied by a magnetic dipole moment

$$\boldsymbol{\mu} = -\frac{ge}{2m_e} \mathbf{S} \quad , \quad (1.21)$$

where  $\mathbf{S}$  denotes the total angular momentum. The Landé factor  $g$  is close to 2 for many ferromagnetic materials.  $\boldsymbol{\mu}$  and the magnetic polarization  $\mathbf{J}$  are correlated via

$$\mathbf{J} = \mu_0 n \boldsymbol{\mu} = -\mu_0 g n \mu_B S \mathbf{u} = -J_S \mathbf{u} \quad . \quad (1.22)$$

$n$  is the number of spins per volume (for a simple cubic lattice  $n = 1/a^3$ ),  $\mu_B = e\hbar/2m_e \approx 9.274 \cdot 10^{-24}$  J/T the Bohr magneton,  $S$  the quantum number of the total angular momentum and  $J_S$  the spontaneous polarization.  $\mathbf{u}$  is a unit vector pointing in the direction of  $\mathbf{S}$ .

Let us consider a magnetic body, successively built up by adding magnetic dipoles [17].  $E^j(i)$  denotes the required energy to put the dipole  $i$  into the field of dipole  $j$ . Since no energy is needed for the positioning of the first dipole, the magnetic strayfield or self energy follows as

$$\begin{aligned} E_S = & E^1(2) \\ & + E^1(3) + E^2(3) \\ & \vdots \\ & + E^1(N) + E^2(N) + \dots + E^{N-1}(N) \quad . \end{aligned} \quad (1.23)$$

However, one can also put together the magnet in reversed order, obtaining

$$\begin{aligned}
E_S = & E^N(N-1) \\
& + E^N(N-2) + E^{N-1}(N-2) \\
& \vdots \\
& + E^N(1) \quad + E^{N-1}(1) + \dots + E^2(1) \quad .
\end{aligned} \tag{1.24}$$

Hence, we find

$$\begin{aligned}
2E_S = & 0 \quad + E^2(1) \quad + \dots + E^{N-1}(1) + E^N(1) \\
& + E^1(2) \quad 0 \quad + \dots + E^{N-1}(2) + E^N(2) \\
& \vdots \\
& + E^1(N) + E^2(N) + \dots + E^{N-1}(N) + 0 \quad .
\end{aligned} \tag{1.25}$$

When we rewrite Eq. (1.25) we get for the magnetic strayfield

$$E_S = \frac{V}{2} \sum_{i=1}^N E(i) \quad , \tag{1.26}$$

where

$$E(i) = -J_S \mathbf{H}_d^i \cdot \mathbf{u}^i \tag{1.27}$$

designates the energy of the dipole  $i$  in the field

$$\mathbf{H}_d^i = -\frac{J_S}{4\pi\mu_0} \sum_{j \neq i} \left\{ \frac{\mathbf{u}^j}{(R^{ij})^3} - \frac{\mathbf{R}^{ij}(\mathbf{u}^j \cdot \mathbf{R}^{ij})}{(R^{ij})^5} \right\} \quad , \tag{1.28}$$

generated by the other ones.

#### 1.2.4 Magnetic Field Energy or Zeeman Energy

The interaction energy of a magnetized body of the volume  $V$  with a uniform external field  $\mathbf{H}$  is

$$E_H = -V J_S \mathbf{H} \cdot \sum_{i=1}^N \mathbf{u}^i \quad . \tag{1.29}$$

It depends only on the average magnetization and not on the domain structure or the sample shape.

### 1.3 Landau-Lifshitz-Gilbert Equation

The starting point of any *dynamic* description of micromagnetic processes at zero temperature is the equation

$$\frac{\partial \mathbf{J}}{\partial t} = -\gamma \mathbf{J} \times \mathbf{H}_{\text{eff}} \quad , \quad (1.30)$$

which can be obtained with basic principles of quantum mechanics.  $\mathbf{J}$  denotes the magnetic polarization vector,  $\mathbf{J} = \mu_0 \mathbf{M}$ .  $\mathbf{H}_{\text{eff}}$  is the effective field and  $\gamma = \mu_0 g e / 2 m_e = g \cdot 1,105 \cdot 10^5 \text{ m/As}$  the gyromagnetic ratio ( $\gamma > 0$ ).

$\mathbf{J}$  is presumed to be a continuous function in space. This is valid because the spins do not vary significantly from lattice point to lattice point due to ferromagnetic exchange coupling. At first sight it is not apparent how this concept can be applied to antiferromagnets. But if one subdivides the antiferromagnet into sublattices (in the simplest case two) the direction of magnetization within each sublattice varies slowly again.

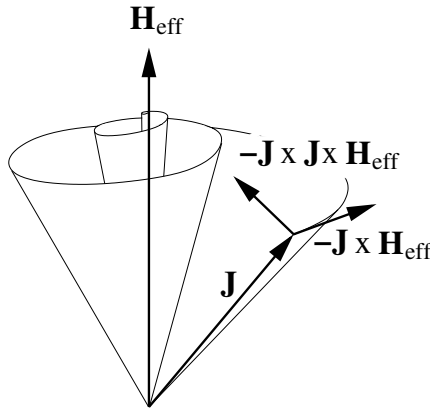


**Figure 1.1:** Illustration of the LLG Eq. (1.33).

Eq. (1.30) describes the well known Larmor precession of the magnetization around the effective field with the Larmor frequency  $\omega = \gamma \mathbf{H}_{\text{eff}}$ . Since no losses have been taken into account the angle between  $\mathbf{J}$  and  $\mathbf{H}_{\text{eff}}$  does not change. In the so-called Gilbert equation

$$\frac{\partial \mathbf{J}}{\partial t} = -\gamma \mathbf{J} \times \mathbf{H}_{\text{eff}} + \frac{\alpha}{J_S} \mathbf{J} \times \frac{\partial \mathbf{J}}{\partial t} \quad (1.31)$$

a dimensionless damping factor  $\alpha$  is introduced to describe dissipative phenomena, like eddy currents or macroscopic discontinuities for example.  $J_S$  is the spontaneous polarization. To obtain the general form

$$\frac{d\mathbf{y}}{dt} = f(t, \mathbf{y}) \quad (1.32)$$

for an ordinary differential equation (ODE), we rewrite Eq. (1.31) and find the mathe-



matically equivalent Landau-Lifshitz-Gilbert (LLG) equation

$$\frac{\partial \mathbf{J}}{\partial t} = -\frac{\gamma}{1+\alpha^2} \mathbf{J} \times \mathbf{H}_{\text{eff}} - \frac{\alpha}{1+\alpha^2} \frac{\gamma}{J_{\text{S}}} \mathbf{J} \times \mathbf{J} \times \mathbf{H}_{\text{eff}} \quad . \quad (1.33)$$

As a result of the damping term the magnetization vector turns towards the effective field until both vectors align parallel (see Fig. 1.1). The effective field is given by

$$\mathbf{H}_{\text{eff}} = -\left(\frac{\delta E}{\delta \mathbf{J}}\right)_T \quad , \quad (1.34)$$

where  $E$  denotes the total Gibbs free energy. Thus,  $\mathbf{H}_{\text{eff}}$  points in the direction of the gradient of  $E$ . Note that  $\mathbf{H}_{\text{eff}}$  is only a helpful definition and not actually a physical field [3].

Dynamic approaches based on the LLG equation are probably the most common method for the simulation of magnetization processes.

# Chapter 2

## Exchange Bias – an Overview

### 2.1 Introduction

The coupling of a ferromagnetic film to an antiferromagnetic material significantly changes some of the properties of the ferromagnet. When the bilayer system is cooled below the Néel temperature ( $T_N$ ) of the antiferromagnet, starting at a temperature  $T_i$  ( $T_N < T_i < T_C$ ,  $T_C$  is the Curie temperature of the ferromagnet), a *unidirectional anisotropy* is induced in the ferromagnet. Usually an external field is applied to fix the direction of the ferromagnet during the cooling process. This procedure is called *field cooling*. The antiferromagnet chooses the state that minimizes the energy due to the coupling to the ferromagnet. After field cooling the antiferromagnet “remembers” the initial ferromagnetic direction, even if the ferromagnet is reversed later.

One of the consequences of the coupling is the displacement of the magnetization curve along the field axis (Fig. 2.1), characterized by the *exchange bias field*  $H_{\text{eb}}$ . Normally,  $H_{\text{eb}}$  is calculated via [14]

$$H_{\text{eb}} = \frac{H^+ + H^-}{2} \quad , \quad (2.1)$$

where  $H^+$  and  $H^-$  denote the right and the left intersection of the hysteresis curve and the field axis.  $H_{\text{eb}}$  opposes the external field, applied during field cooling. However, positive exchange bias fields were also obtained in experiments [26].

Another effect is the increase of the *coercivity*  $H_C$  as shown in Fig. 2.1.  $H_C$  can be calculated with the formula [14]

$$H_C = \frac{H^+ - H^-}{2} \quad . \quad (2.2)$$

Almost all ferromagnetic films coupled to an antiferromagnet exhibit an enlargement of their coercive field, even when the bilayer system does not show bias.

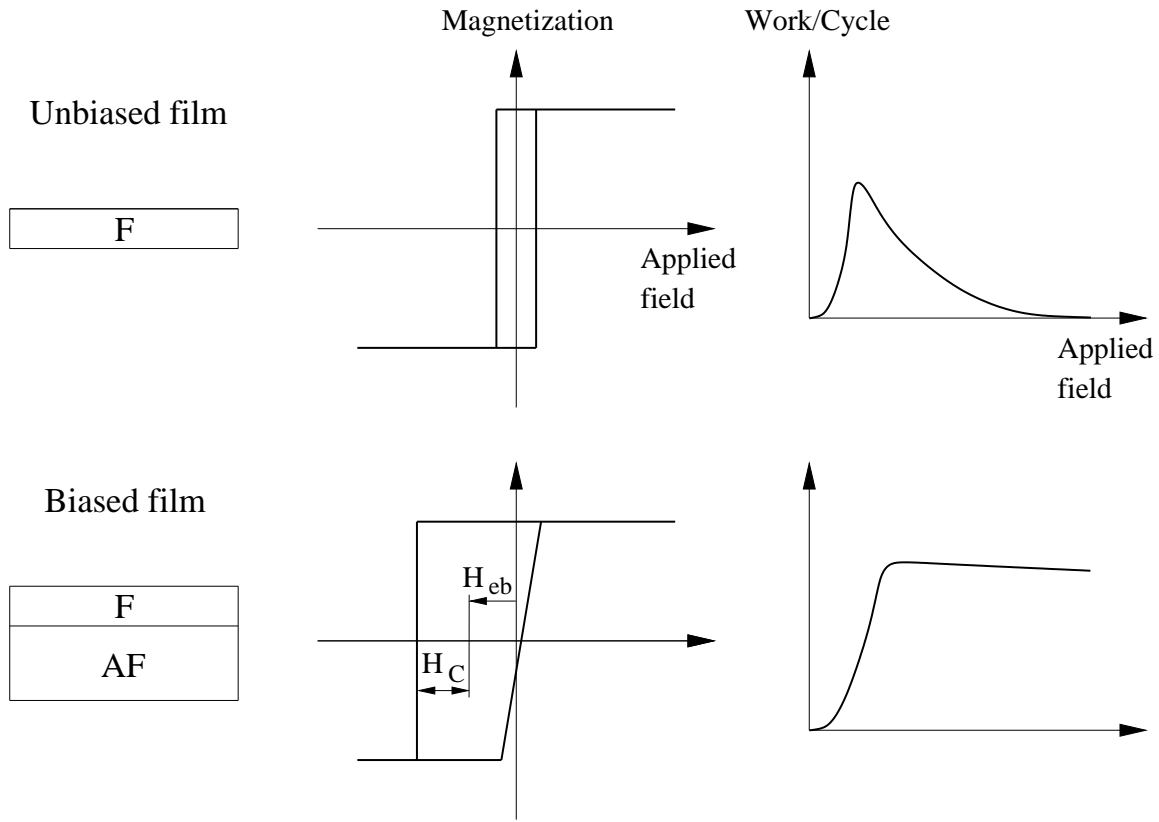


**Figure 2.1:** Experimental characteristics of exchange biased systems. The upper pictures show typical results of free ferromagnetic films, whereas the lower represent those of exchange coupled bilayer systems. Compared with the hysteresis cycle of an unbiased ferromagnetic film, the magnetization curve of the biased ferromagnet exhibits a displacement along the field axis and an enhanced coercivity. Rotational hysteresis measurements (on the right hand side) indicate dissipative mechanisms in bilayer systems. In contrast, the work per cycle integrate to zero over a full rotation of unbiased films and for external fields high enough to saturate the ferromagnet.

$H_{eb}$  and  $H_C$  are often found to be inversely proportional to the thickness of the ferromagnet [24]. This points out that the phenomenon of unidirectional anisotropy is strongly localized at the interface. Of course, deviations are observed below a certain ferromagnetic thickness.

Most experiments show that the antiferromagnet has to exceed a critical thickness to provide exchange bias. Usually, the exchange bias field as a function of the antiferromagnetic thickness attains a maximum and then decreases with increasing thickness [33].

As depicted in Fig. 2.1 for the biased film, different reversal mechanisms are observed for increasing and decreasing fields [31]. That is, the common way to calculate the exchange bias field (Eq. (2.1)) yields possibly not a reliable measure of the size of the unidirectional anisotropy. Therefore, we propose a new method to determine the exchange bias field.

The so called *high field rotational torque* experiment shows that *irreversible losses* occur in the exchange coupled system. The sample is rotated in a fixed external field, high enough to saturate the ferromagnet, and the torque as a function of the angle  $\theta$  is measured. In unbiased ferromagnets the torque integrates to zero over a full rotation. However, exchange biased films exhibit a different behavior. The torque does not integrate to zero over a full cycle, even in very high external fields (see Fig. 2.1). This indicates a dissipative mechanism in the bilayer system [31]. Additionally, the results of high field rotational torque measurements depend on the previous history of the sample. This *training effect* leads to a decrease of  $H_{\text{eb}}$  and  $H_C$  with the number of hysteresis cycles. Experimentally, the relation

$$H_{\text{eb},n} - H_{\text{eb},\infty} \propto \frac{1}{\sqrt{n}} \quad (2.3)$$

is often found [24], where  $n$  designates the number of hysteresis cycles.

The following sections give a short introduction to the best-known models of exchange biased systems.

## 2.2 Meiklejohn and Bean and their Intuitive Picture

Meiklejohn and Bean tried to explain the observed displacement of the hysteresis loop of Co coupled to CoO with a unidirectional anisotropy [21, 22]. They presumed that the interface between Co and the antiferromagnetic CoO is the uncompensated (111) plane of CoO.

Let us consider an applied field in the temperature range  $T_N < T < T_C$ , strong enough to saturate the ferromagnet, while the antiferromagnetic spins remain in a disordered state [27]. Assuming ferromagnetic interactions between the ferromagnet and the antiferromagnet, Fig. 2.2 shows the system after field cooling ( $T < T_N$ ). The antiferromagnetic spins at the interface align parallel to those of the ferromagnet, whereas the others arrange in a way to produce no net magnetization.

When the external field is reversed the ferromagnet switches. However, for sufficiently high antiferromagnetic anisotropy the antiferromagnetic spins do not switch. Due to the ferromagnetic coupling the antiferromagnetic spins at the interface try to keep the ferromagnetic spins in their original position. That is to say, the coupling between the ferromagnet and the antiferromagnet induces a *unidirectional anisotropy* in the ferromagnetic layer. To reverse an exchange biased ferromagnet one needs a larger field than one needs for a single ferromagnetic layer. When the external field is rotated back to its original direction, the ferromagnet switches at a smaller field than for an uncoupled ferromagnetic layer. Therefore, the magnetization curve exhibits a shift in the field axis,

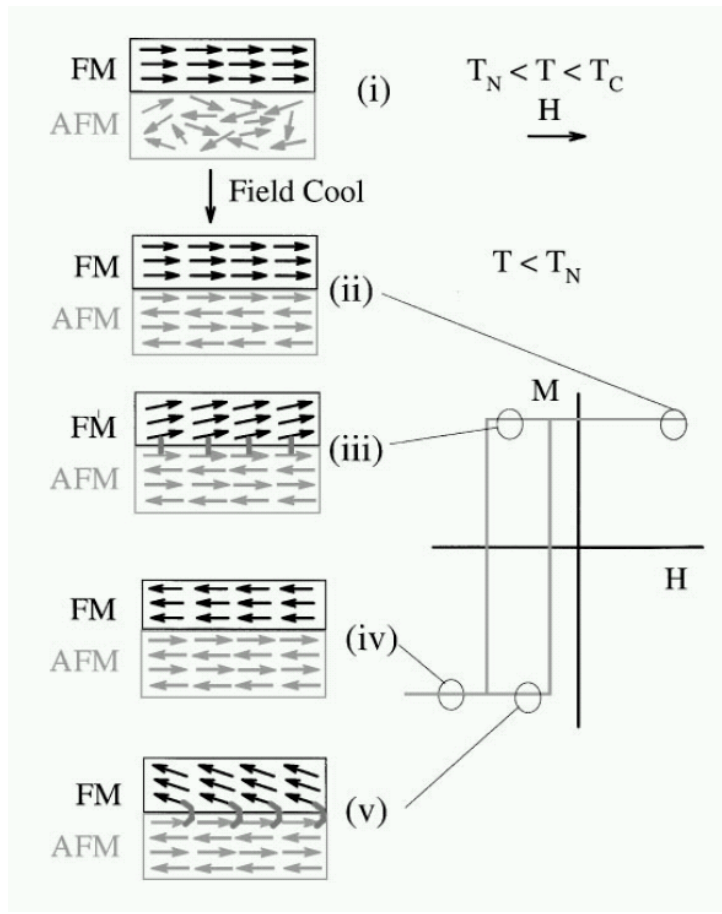


**Figure 2.2:** A schematic illustration of the spin configuration of a ferro-/antiferromagnetic bilayer at different stages of the displaced hysteresis loop. From Ref. [27].

i.e. exchange bias.

In this simple model the total free energy per unit area can be written as [23]

$$E = -\mu_0 H M_F t_F \cos(\theta - \beta) + K_F t_F \sin^2 \beta + K_{AF} t_{AF} \sin^2 \alpha - J_{INT} \cos(\beta - \alpha) \quad , \quad (2.4)$$

where  $H$  is the external field,  $M_F$  the saturation magnetization of the ferromagnet,  $t_F$  the thickness of the ferromagnet,  $t_{AF}$  the thickness of the antiferromagnetic layer,  $K_F$  the anisotropy constant of the ferromagnet,  $K_{AF}$  the anisotropy constant of the antiferromagnet, and  $J_{INT}$  the interface coupling constant.  $\beta$  is the angle between the magnetization and the easy axis of the ferromagnet.  $\alpha$  denotes the angle between the antiferromagnetic sublattice magnetization and the antiferromagnetic anisotropy axis, whereas  $\theta$  indicates the angle between the external field and the ferromagnetic anisotropy axis.

If one neglects the ferromagnetic anisotropy, one finds for the exchange bias field after

minimizing the energy with respect to  $\alpha$  and  $\beta$  [23]

$$H_{\text{eb}} = \frac{J_{\text{INT}}}{\mu_0 M_{\text{F}} t_{\text{F}}} \propto \frac{1}{t_{\text{F}}} \quad . \quad (2.5)$$

If the antiferromagnetic spins are no longer restricted to the anisotropy axis, the important result required for the observation of exchange anisotropy

$$K_{\text{AF}} t_{\text{AF}} \geq J_{\text{INT}} \quad (2.6)$$

can be numerically obtained. If this condition is not fulfilled, the antiferromagnetic spins follow the rotation of the ferromagnet. Hence, no exchange bias occurs.

Although this model gives an intuitive insight into the phenomena of exchange bias, it is too simple to account for the various experimental results. In particular, it predicts an exchange bias field several orders of magnitude larger than all experimentally measured values. Moreover, exchange bias was found experimentally for uncompensated as well as for fully compensated interfaces [1, 27].

## 2.3 Domain Wall Model of Mauri

Mauri et al. [20] proposed a mechanism resulting in a lower interfacial energy than the model of Meiklejohn and Bean. They suggested the formation of a planar domain wall at the interface as the ferromagnet rotates. Depending on the domain wall energies, the domain wall could be formed in the antiferromagnet or in the ferromagnet, respectively. Mauri et al. considered the case that the domain wall energy in the antiferromagnet is much lower than in the ferromagnet. Therefore, the domain wall is formed in the antiferromagnet.

The antiferromagnet is assumed to be infinitely thick, and the spins are restricted to planes perpendicular to the  $z$ -axis. In these planes the spins of one sublattice are parallel (Fig. 2.3).

Since the thickness of the ferromagnetic layer  $t_{\text{F}}$  is assumed to be small, all the ferromagnetic spins are parallel. One therefore finds for the total free energy per unit area [24]

$$\begin{aligned} E = & 2 \sqrt{A_{\text{AF}} K_{\text{AF}}} (1 - \cos \alpha) + \frac{A_{\text{AF-F}}}{\xi} (1 - \cos(\alpha - \beta)) + K_{\text{F}} t_{\text{F}} \cos^2 \beta + \\ & + \mu_0 H M_{\text{F}} t_{\text{F}} \cos(\theta - \beta) \quad . \end{aligned} \quad (2.7)$$

$K_{\text{AF}}$  and  $A_{\text{AF}}$  denote the anisotropy constant and the exchange stiffness of the antiferro-

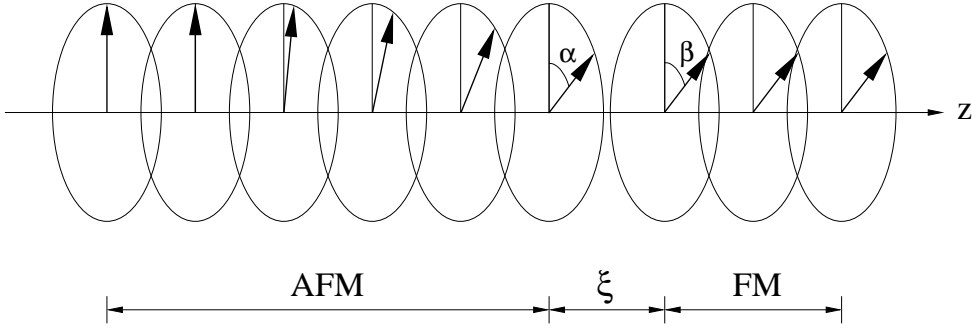


**Figure 2.3:** In the antiferromagnet only the magnetization of one sublattice is shown.  $\alpha$  and  $\beta$  are the angles between the interfacial spins and the easy axes of the antiferromagnet and ferromagnet, respectively.  $\xi$  denotes the distance between the two layers.

magnet, respectively, whereas  $K_F$  is the anisotropy constant of the ferromagnet.  $A_{AF-F}$  is the interfacial coupling constant,  $\xi$  the distance between the two layers,  $H$  the external field and  $\theta$  the angle of  $H$  with respect to the easy axis of the ferromagnet. The first term in Eq. (2.7) is the domain wall energy in the antiferromagnet and the second the interface energy. The third and the last terms denote the anisotropy energy and the Zeeman energy of the ferromagnet, respectively.

Minimizing Eq. (2.7) with respect to  $\alpha$  and  $\beta$  for a given external field yields the following two limiting cases:

- The interface energy is much larger than the domain wall energy

$$H_{eb} = -2 \frac{\sqrt{A_{AF}K_{AF}}}{\mu_0 M_F t_F} \quad (2.8)$$

- The interface energy is much smaller than the domain wall energy

$$H_{eb} = -\frac{A_{AF-F}}{\xi \mu_0 M_F t_F} \quad (2.9)$$

With  $J_{INT} = A_{AF-F}/\xi$  we find the expression of Meiklejohn and Bean Eq. (2.5).

Mauri's domain wall in the antiferromagnet may become unstable when  $\alpha$  reaches a certain critical angle  $\alpha_{crit}$ . For large interface coupling the antiferromagnet then switches to another state with reversed ordering far away from the interface. Néel first looked into this phenomenon and found that for antiferromagnets thicker than  $\delta/4$  ( $\delta$  is the domain wall width) the irreversible transitions occur at a critical angle  $\alpha_{crit} \in [90^\circ, 180^\circ]$ . For  $t_{AF} \rightarrow \infty$  the critical angle approaches  $180^\circ$ . It is worth noting that these irreversible transitions lead to rotational hysteresis loss and a field shift in the isotropic ferromagnetic resonance [31].

When the interface energy is small compared with the domain wall energy, the system behaves differently. Beyond  $\alpha_{\text{crit}} > 90^\circ$  the interface coupling cannot compensate the large domain wall energy. Therefore, antiferromagnetic spins turn back and form a new twist with opposite direction of rotation.

## 2.4 Malozemoff's Random Field Model

Malozemoff gave up the assumption of a perfectly uncompensated and smooth interface [19]. Instead he proposed an imbalance of the interfacial antiferromagnetic moments as a result of roughness and structural defects.

Assuming a single domain ferromagnetic layer, the antiferromagnet breaks up into domains to minimize the free energy. The domain walls in this model are perpendicular to the interface, in contrast to Mauri's model. A large number of antiferromagnetic domains would lower the interface energy but enhance the domain wall energy. Malozemoff obtained an optimal size of the domains

$$L \approx \pi \sqrt{\frac{A}{K}} \quad , \quad (2.10)$$

where  $A$  denotes the exchange constant in the antiferromagnet and  $K$  the uniaxial anisotropy.

The random field model then argues that in a region of  $N$  antiferromagnetic spins on a perfectly rough interface on average  $z\sqrt{N}$  spins are uncompensated, where  $z$  is a number in the order of unity. The number of spins in the area  $L^2$  is  $N = L^2/a^2$ , where  $a$  denotes the lattice constant. Accordingly, one finds for the exchange bias field

$$H_{\text{eb}} = -\frac{2z\sqrt{AK}}{\pi^2 M_{\text{F}} t_{\text{F}}} \quad . \quad (2.11)$$

This equation is very similar to the one of Mauri's for large interfacial energy (Eq. (2.8)).

Malozemoff's model explains several properties of exchange biased systems (for instance the training effect due to annihilation of domains during a hysteresis cycle). However, the statistical argument is quite unsatisfactory.



## 2.5 Koon's Spin Flop Coupling at Compensated Interfaces

Measurements of several bilayer systems indicate perpendicular coupling between the ferromagnet and the antiferromagnet [11]. Nogués et al. [25] investigated  $\text{FeF}_2/\text{Fe}$  bilayers and found the largest bias field for the *compensated* (110) interface orientation. Furthermore they discovered that the exchange bias field decreases with increasing interface roughness. Surprisingly, the same group found a *positive* unidirectional exchange anisotropy for large cooling fields [26].

Due to these experimental results, Koon proposed his spin flop model at fully compensated interfaces [16], i.e. the number of interfacial spins of sublattice A equals those of sublattice B. For absolutely antiparallel spins the antiferromagnet would provide no net moment. Obviously, all orientations of the ferromagnetic magnetization would therefore result in the same interface energy. Yet, Koon considered the case that the interfacial antiferromagnetic spins are not fully antiparallel but canted by a small angle  $\theta$  because of the coupling to the ferromagnet. That is, the ferromagnet produces a small net moment in the antiferromagnet parallel to the direction of the magnetization in the ferromagnetic layer and perpendicular to the easy axis in the antiferromagnet (see Fig. 2.4). The antiferromagnetic spins at the interface thus align perpendicular to the ferromagnetic moment.

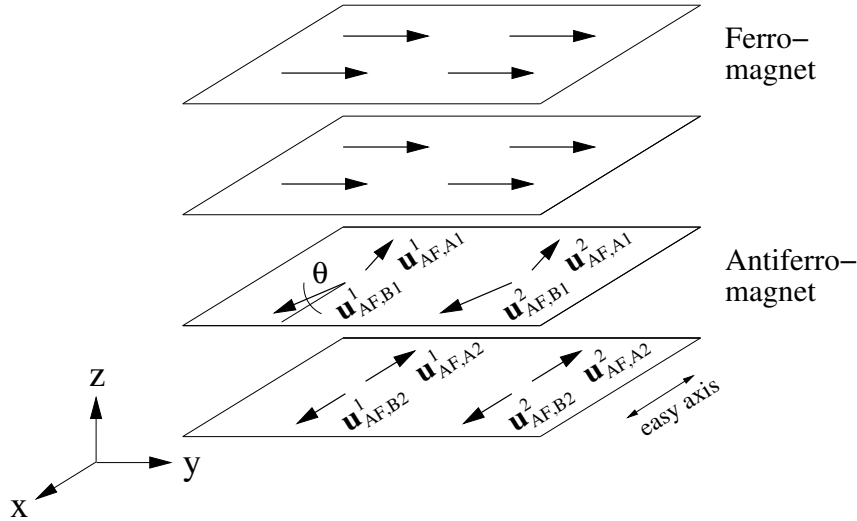


**Figure 2.4:** Spin flop coupling of a ferromagnet/antiferromagnet bilayer system.  $\mathbf{u}_{AF,A1}^2$  for example denotes the unit vector of the spin direction of sublattice A and monolayer 1 in the antiferromagnetic grain 2.

In addition, he assumed strong interface coupling and that the antiferromagnetic spins are restricted to planes parallel to the interface.

Suess et al. [36] investigated the dependence of  $\theta$  on the distance from the interface. They found out that  $\theta$  decreases from one antiferromagnetic monolayer to the next by approximately a factor 10. The canted spin structure at the interface thus relaxes within a few monolayers to the totally antiparallel alignment. In other words, the spin flop coupling is strongly localized at the interface.

Koon's model is able to explain exchange bias, even a positive shift of the hysteresis loop. However, Schulthess and Butler [29] pointed out that partial domain walls which are essential for Koon's model are not stable due to out of plane rotation.

## 2.6 Polycrystalline Antiferromagnets of Stiles and McMichael

In the model of Stiles and McMichael the ferromagnetic layer interacts with independent antiferromagnetic grains [31]. The external field is assumed to be high enough so that the ferromagnetic magnetization can be considered to be uniform. Since the antiferromagnetic grains are presumed to be small enough they do not break up into domains. However, partial domain walls parallel to the interface as a result of the coupling to the ferromagnet are allowed to occur.

The energy for each grain with the interfacial area  $N/a^2$  can be written as

$$\frac{E}{Na^2} = \underbrace{-\frac{J_{\text{net}}}{a^2} (\widehat{\mathbf{M}}_{\text{FM}} \cdot \widehat{\mathbf{m}}(0))}_{\text{direct coupling}} + \underbrace{\frac{J_{\text{sf}}}{a^2} (\widehat{\mathbf{M}}_{\text{FM}} \cdot \widehat{\mathbf{m}}(0))^2}_{\text{spin flop coupling}} + \underbrace{\frac{\sigma}{2} (1 - \widehat{\mathbf{m}}(0) \cdot (\pm \widehat{\mathbf{u}}))}_{\text{domain wall energy}} \quad . \quad (2.12)$$

$N$  denotes the number of spins at the interface of the grains,  $a$  is the lattice constant. The directions are  $\widehat{\mathbf{M}}_{\text{FM}}$ , the ferromagnetic magnetization,  $\widehat{\mathbf{m}}(0)$  the direction of the net sublattice magnetization at the interface, and  $\pm \widehat{\mathbf{u}}$  the two easy directions of the uniaxial anisotropy in the antiferromagnet.  $J_{\text{net}}$  is the average direct coupling to the net moment of the antiferromagnetic grain,  $J_{\text{sf}}$  designates the spin flop coupling, and  $\sigma$  is the energy of a  $180^\circ$  domain wall in the antiferromagnet.

Experimentally, the biased state is prepared by field cooling the system. In the model of Stiles and McMichael this process is simulated by choosing the antiferromagnetic state for each grain with the lowest energy with respect to the fixed ferromagnetic magnetization. With it the exchange bias field is given by [24]

$$H_{\text{eb}} = \frac{J_{\text{net}}}{2a^2 \mu_0 M_{\text{FM}} t_{\text{FM}}} \quad \text{for} \quad \frac{2J_{\text{net}}}{\sigma a^2} < 1 \quad , \quad (2.13)$$

$$H_{\text{eb}} = \frac{\sigma}{4\mu_0 M_{\text{FM}} t_{\text{FM}}} \quad \text{for} \quad \frac{2J_{\text{net}}}{\sigma a^2} > 1 \quad . \quad (2.14)$$

Owing to the results of high field rotational hysteresis measurements and isotropic ferromagnetic resonance some of the antiferromagnetic grains must switch irreversibly. Stiles and McMichael postulated that some grains have a critical angle  $\alpha_{\text{crit}}$ . A partial domain wall wound up above this angle becomes unstable and the grain makes an irreversible transition to a new state with reversed order far from the interface (see Fig. 2.5).

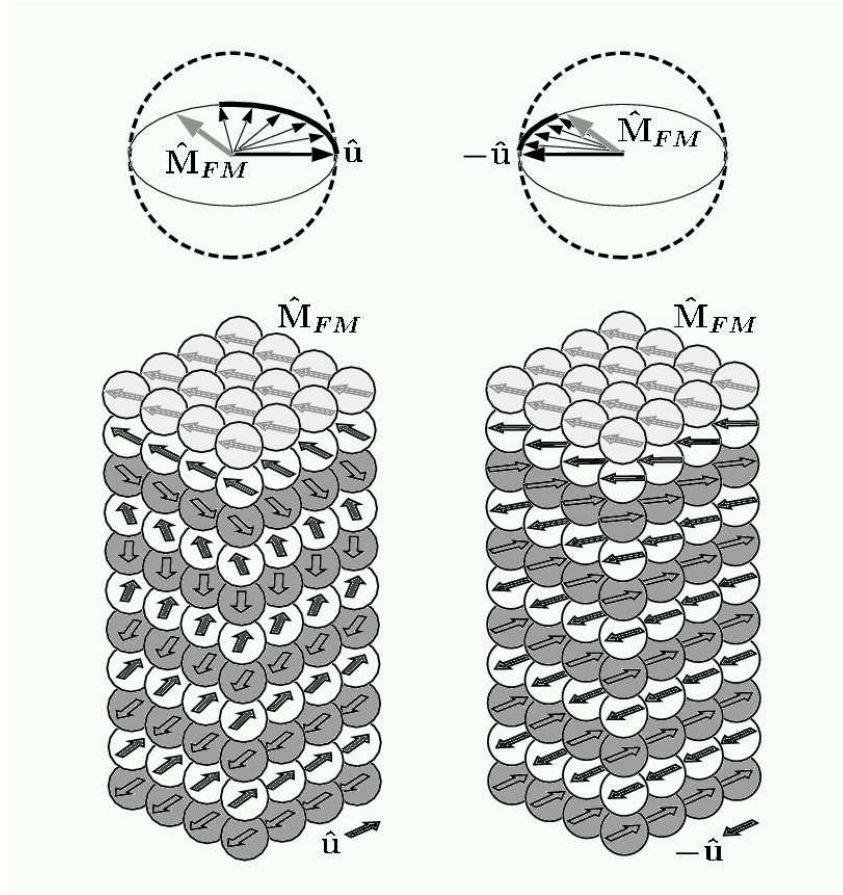


**Figure 2.5:** The white spheres are the antiferromagnetic atoms of the sublattice that predominates at the interface and the dark gray are the ones of the other sublattice. The light gray spheres represent the ferromagnetic atoms. On the left the antiferromagnet has ordered in the  $+\hat{\mathbf{u}}$  direction far from the interface, whereas the right structure pictures the switched antiferromagnetic grain. In both a partial domain wall is wound up due to the coupling of the two layers. From Ref. [31].

Stiles and McMichael found that grains with easy axes close enough to the interface normal maintain their antiferromagnetic order far from the interface when the ferromagnet switches in-plane.

In addition, they conceived the important result that the spin flop coupling for typical grain sizes and for comparable values of the interfacial constant and the antiferromagnetic exchange constant is much stronger than the direct coupling.

## Spin Flop Coupling

It is not obvious why Stiles and McMichael [31] or Stamps [30] suggested a biquadratic spin flop term. Since this expression plays an important role in our model, we have a closer look at its origin.

Consider a ferromagnetic spin perpendicular to fully antiparallel antiferromagnetic moments. When the two antiferromagnetic spins are canted by an angle  $\theta$  (see Fig. 2.4) the direct coupling energy of the ferromagnet/antiferromagnet bilayer system decreases (first term in Eq. (2.12)). This contribution to the total free energy is proportional to  $-\cos(\pi/2 - \theta)$ .

As we leave the anisotropy energy of the antiferromagnet out of consideration (third term in expression (2.12)), the exchange energy in the antiferromagnetic grain between the two sublattices can be written as

$$E_{\text{sf}} \propto \cos(\pi - 2\theta) = \cos^2\left(\frac{\pi}{2} - \theta\right) - \sin^2\left(\frac{\pi}{2} - \theta\right) = 2\cos^2\left(\frac{\pi}{2} - \theta\right) - 1 \quad . \quad (2.15)$$

That is,  $E_{\text{sf}}$  increases with increasing  $\theta$ . Additive constants in energy expressions have no physical meaning. Hence, we obtain

$$E_{\text{sf}} \propto \cos^2\left(\frac{\pi}{2} - \theta\right) \propto \left(\widehat{\mathbf{M}}_{\text{FM}} \cdot \widehat{\mathbf{m}}(0)\right)^2 \quad . \quad (2.16)$$

So, the spin flop term of Stiles and McMichael can be understood as the energy needed to remove the totally antiparallel alignment of the antiferromagnetic spins. The harder it is to cant the spins the weaker the spin flop coupling because the ferromagnet then only induces a very small magnetic moment in the antiferromagnet to interact with.

# Chapter 3

## Interacting Grain Model

### 3.1 Introduction

Suess [33] presented an approach for solving the LLG equation for antiferromagnets with the finite element method. He assumed spin flop coupling between the polycrystalline ferro- and antiferromagnet at a fully compensated interface. Contrary to other theories introducing some sort of defects within the antiferromagnet or at the interface in order to find exchange bias at mainly compensated interfaces, he showed that a system free of imperfections can still exhibit exchange bias.

Stiles and McMichael [31] pointed out that spin flop coupling increases the coercivity but does not contribute to the unidirectional anisotropy. However, they considered a polycrystalline antiferromagnet with independent grains whereas our model takes into account exchange coupled grains.

The finite element approach showed that the magnetization configurations in the antiferromagnetic grains remain almost uniform during the reversal of the ferromagnet. Therefore, a granular model where the magnetization is actually uniform within the antiferromagnetic grains should yield very similar results but allows to simulate larger systems with the great advantage of avoiding possible finite size effects.

### 3.2 The Model

Let us consider a thin ferromagnetic film spin flop coupled to a polycrystalline antiferromagnet with randomly oriented easy axes. The magnetization configuration within the antiferromagnetic grains are assumed to be uniform. This is a good approximation for small grain sizes and low intergrain exchange coupling within the antiferromagnet. Due to the spin flop coupling the antiferromagnetic spins are not fully antiparallel. Since the deviation is small and relaxes very rapidly to the spin structure of the bulk we neglect

the tilting of the spins. Thus, for the simplest case of two sublattices the magnetic state of each antiferromagnetic grain can be described by a single vector of one sublattice. The magnetization vector of the other sublattice points exactly antiparallel.

In a rough picture, the exchange bias effect can be understood by a change of the Gibbs free energy owing to irreversible transitions in the antiferromagnet. After field cooling the system possesses the lowest possible energy, i.e. the antiferromagnetic spins arrange in a way to minimize the total free energy. When the external field reverses the ferromagnet, some antiferromagnetic grains switch irreversibly. The random orientation of the magnetocrystalline anisotropy axes in the antiferromagnetic grains makes sure that not all grains switch irreversibly. Due to the intergrain coupling between the grains the Gibbs free energy increases.

For a better understanding of the mechanism leading to exchange bias in this model let us consider two antiferromagnetic grains spin flop coupled to a uniformly magnetized ferromagnet (Fig. 3.1). Grain 1 has an easy axis close to the interface normal whereas that of Grain 2 is mostly parallel to the interface (both easy axes lie in the image plane).

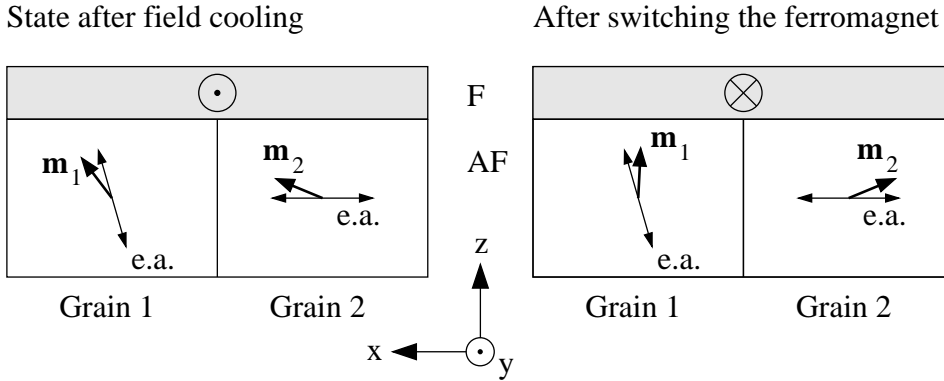


**Figure 3.1:** Magnetization configuration in the antiferromagnet (AF) after field cooling (left) and after the reversal of the ferromagnet (F, right). Only the spin direction of one sublattice is shown.

After field cooling the system is in its energy minimum. Due to the coupling of the antiferromagnetic grains the configuration with  $\mathbf{m}_1$  and  $\mathbf{m}_2$  parallel to their easy axes would result in a higher energy. When the ferromagnet reverses, Grain 2 switches *irreversibly*, whereas the main direction of the magnetization  $\mathbf{m}_1$  remains more or less unaffected. That is, Grain 1 is affected *reversibly* by the ferromagnet.

It is difficult to say if a certain grain switches or not because different mechanisms contribute to the partial switching. But a rough criterion for an irreversible transition of an antiferromagnetic grain is that the easy axis is “almost parallel” to the interface. However,

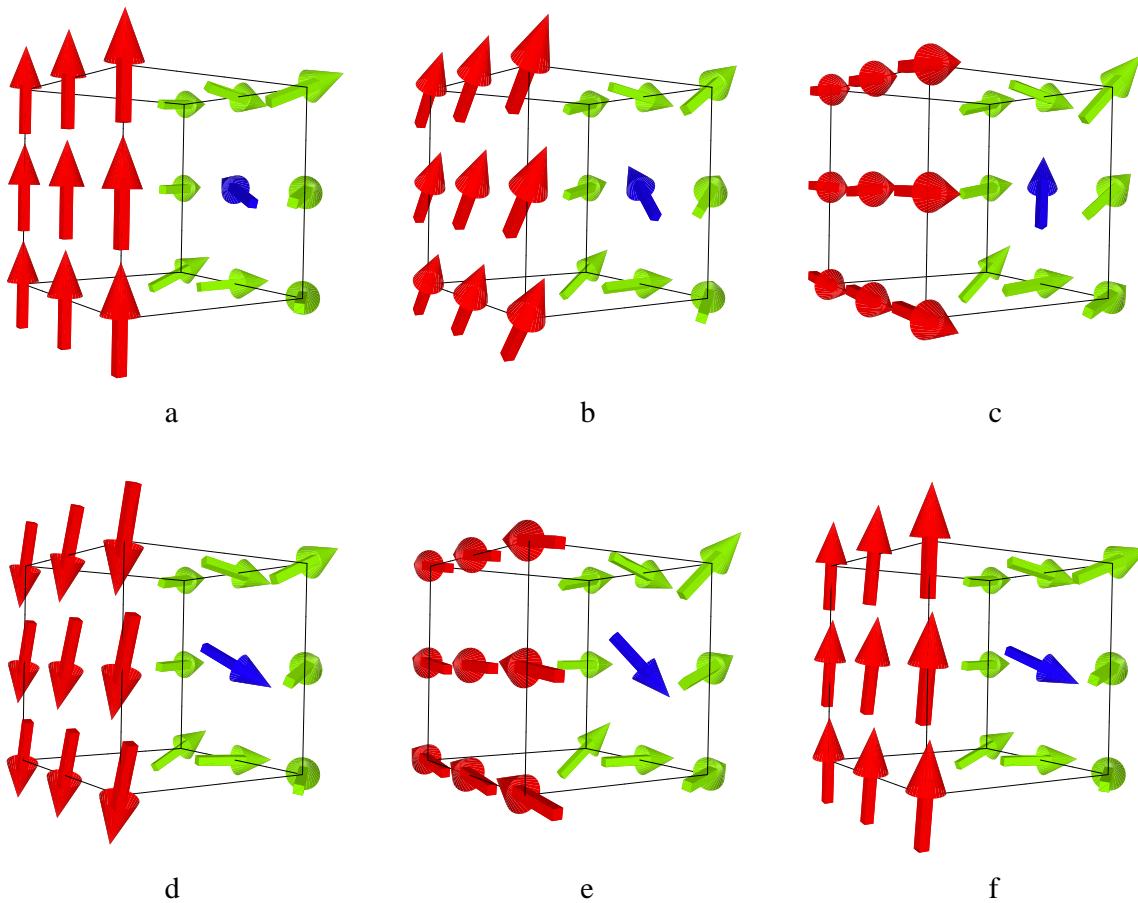
for the most part regions of several grains switch irreversibly rather than single grains. This is due to the coupling of the antiferromagnetic grains leading to a common behavior.

In any case, the spins make a transition from one local minimum of the anisotropy energy to the equivalent with opposite direction of the sublattice magnetization. The spin flop energy after reversing the ferromagnet has not changed, either. However, the enlargement of the angle between  $\mathbf{m}_1$  and  $\mathbf{m}_2$  yields a higher exchange energy in the antiferromagnet. That is, the states after field cooling and after switching the ferromagnet are not symmetric. The field required to switch the ferromagnet from the field cooled state into the reversed state is larger than that to rotate the ferromagnet back to its original direction.

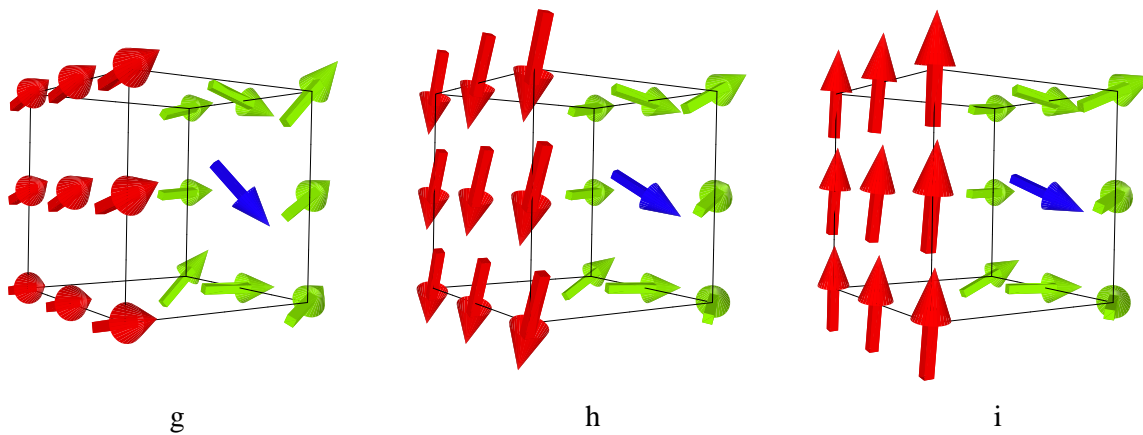
This asymmetry is usually thought to be the origin of exchange bias, which is evident for the simple picture considered above. But for more complex systems it is quite more difficult. For some parameters we have found *positive* exchange bias although the energy of the negative remanent state was higher than for the positive remanence. That is, at least for some bilayer systems it is not sufficient to explain the difference of the total energies in the positive and negative remanent state. However, most of the simulated systems showed a negative bias field for a negative energy difference.

Fig. 3.2 shows a sequence of more realistic images calculated with our model to illustrate the processes leading to exchange bias. The red spins in the front represent the ferromagnetic layer. For the antiferromagnet only the spins of one sublattice are shown. Fig. 3.2.a depicts the magnetization configuration after field cooling. The easy axes of the antiferromagnetic grains are more or less perpendicular to the film plane, except that of the middle grain with the blue spin. Reversing the ferromagnet thus mainly affects the blue spin which undergoes an irreversible transition (a→d). This causes the antiferromagnetic exchange energy to rise considerably. When the ferromagnet rotates back (d→f) the middle spin maintains its new direction due to intergranular exchange coupling, leading to asymmetric remanent states and therefore to exchange bias. The following rotation of the ferromagnet (g→i) leaves even the blue spin unaffected. Consequently no bias effect occurs, i.e. this simulation also explains the training effect.

### Cycle 1



### Cycle 2



**Figure 3.2:** A small simulation of  $3 \times 3$  grains to illustrate the processes responsible for exchange bias. The ferromagnetic layer is indicated by the red arrows on the left of each cube. An explanation can be found in the text.



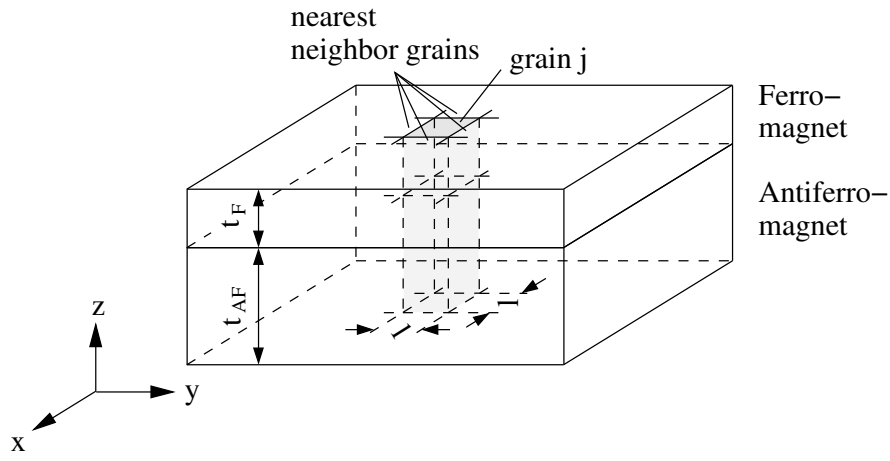


**Figure 3.3:** Grain  $j$  and its nearest neighbor grains. The basal planes of the grains are squares, equal in size. The grain structure in the ferromagnet and antiferromagnet are the same.

Our interacting grain (IG) model considers anisotropy, Zeeman and intergrain exchange energy terms and assumes a completely compensated interface. The total energy of the ferromagnet(F)/antiferromagnet(AF) bilayer system per grain  $j$  is

$$\begin{aligned}
 E^j = & \sum_{i=1}^{n.n.} \left( \underbrace{-J_F S^2 n_F t_F l}_{\text{exchange energy F}} \mathbf{u}_F^i \cdot \mathbf{u}_F^j \quad \underbrace{-J_{AF} S^2 n_{AF} t_{AF} l}_{\text{exchange energy AF}} \mathbf{u}_{AF}^i \cdot \mathbf{u}_{AF}^j \right) \\
 & \underbrace{-J_{AF-F} S^2 n_I l^2 (\mathbf{u}_F^j \cdot \mathbf{u}_{AF}^j)^2}_{\text{spin flop coupling}} \quad \underbrace{-K_1 t_{AF} l^2 (\mathbf{k}_{AF}^j \cdot \mathbf{u}_{AF}^j)^2}_{\text{anisotropy energy AF}} \\
 & \underbrace{+ \frac{J_S^2}{\mu_0} t_F l^2 (\mathbf{k}_F^j \cdot \mathbf{u}_F^j)^2}_{\text{in-plane anisotropy F}} \quad \underbrace{-J_S t_F l^2 \mathbf{H} \cdot \mathbf{u}_F^j}_{\text{Zeeman term}} .
 \end{aligned} \tag{3.1}$$

The sum over  $i$  is taken only over the nearest neighbor grains (n.n.) in the antiferromagnet and ferromagnet, respectively (see Fig. 3.3).

The quantities are

|                     |     |   |
|---------------------|-----|---|
| $J_F$               | ... | exchange integral across ferromagnetic grains, in J/m   |
| $J_{AF}$            | ... | exchange integral across antiferromagnetic grains, in J/m                                       |
| $J_{AF-F}$          | ... | exchange interaction at the compensated interface, in J/m                                       |
| $S$                 | ... | average total spin quantum number, dimensionless  |
| $K_1$               | ... | anisotropy constant of the antiferromagnetic grains, in J/m <sup>3</sup>                        |
| $\mathbf{u}_F^j$    | ... | unit vector of the spin direction in the ferromagnetic grain $j$ , dimensionless                |
| $\mathbf{u}_{AF}^j$ | ... | unit vector of the sublattice spin direction of the antiferromagnetic grain $j$ , dimensionless |
| $\mathbf{k}_F^j$    | ... | unit vector pointing perpendicular to the film plane, dimensionless                             |
| $\mathbf{k}_{AF}^j$ | ... | unit vector of the easy axis direction of the antiferromagnetic grain $j$ , dimensionless       |
| $\mathbf{H}$        | ... | external field, in A/m  |
| $l$                 | ... | grain diameter, in m  |
| $t_F$               | ... | thickness of the ferromagnetic film, in m   |
| $t_{AF}$            | ... | thickness of the antiferromagnetic film, in m   |
| $J_S$               | ... | magnitude of the spontaneous polarization, in T   |
| $n_F$               | ... | number of spins per unit area in the ferromagnetic grains, in m <sup>-2</sup>                   |
| $n_{AF}$            | ... | number of spins per unit area in the antiferromagnetic grains, in m <sup>-2</sup>               |
| $n_I$               | ... | number of spins per unit area at the interface, in m <sup>-2</sup>                              |

For simple cubic lattices with lattice constant  $a$  we find

$$n_F = n_{AF} = n_I = \frac{1}{a^2} \quad (3.2)$$

and for the spontaneous polarization (Eq. (1.22))

$$J_S = \frac{\mu_0 g \mu_B S}{a^3} \quad (3.3)$$

**Exchange energy of the ferromagnet:** Each ferromagnetic grain is exchange coupled to its four nearest neighbor grains. The coupling strength between two grains depends on the number of spins  $t_F l / a^3$  at the contact surface  $t_F l$ . For high ferromagnetic exchange interaction distinct domains occur, whereas ripple structure dominates for low coupling constants.

**Exchange energy of the antiferromagnet:** Each antiferromagnetic grain is coupled to its neighboring grains. Analogous to the ferromagnetic interaction above,  $t_{AF} l$  designates the value of the contact surface between two interacting grains. Weak antiferromagnetic exchange interaction is necessary to find exchange bias because the coupling of the grains reduces the out-of-plane rotation [33]. So, it is possible that a considerable

number of grains make an irreversible transition. For  $J_{\text{AF}} = 0$  only a few antiferromagnetic grains with an easy axis almost parallel to the film plane switch irreversibly. Since this model explains exchange bias as a consequence of domain walls formed in the antiferromagnet, no exchange bias occurs for zero exchange coupling. On the other hand, the exchange bias field decreases rapidly for too strong exchange interaction. The reason is that large regions switch irreversibly and therefore the domain wall energy in the antiferromagnet does not change significantly.

**Spin flop coupling:** The spin flop term in Eq. (3.1) is similar to that of Stiles and McMichael [31] in Eq. (2.12). It implicitly takes into account the canted state of the antiferromagnetic spins even if they are assumed to be perfectly antiparallel. This is a good approximation because the canted state is strongly localized at the interface, as mentioned above. The interface coupling depends on the number of interacting spins,  $l^2/a^2$ , where  $l^2$  is the value of the contact surface of the ferromagnetic and antiferromagnetic grains. Note that the ferromagnetic grain  $j$  is spin flop coupled only to the antiferromagnetic grain  $j$ .

**Anisotropy energy of the antiferromagnet:** The directions of the uniaxial anisotropy in the antiferromagnet are distributed randomly in space. The magnitude of  $K_1$  strongly affects the switching of the grains.

**In-plane anisotropy of the ferromagnet:** The strayfield energy of a uniformly magnetized thin ferromagnetic film attains its minimum when the magnetization is parallel to the film. Since the calculation of this energy contribution is time expensive we approximate it with an in-plane anisotropy. This term assures that the system favors in-plane alignment of the magnetization vectors. Within the film plane the ferromagnet is isotropic in space (Permalloy).

**Zeeman energy:** The external static magnetic field  $\mathbf{H}$  only acts on the ferromagnet and is expected to be weak enough to leave the antiferromagnet unaffected. That is, magnetic surface and volume charges are negligible in the antiferromagnet. This assumption is valid for most experiments.

### 3.3 Implementation

Calculations are performed by first choosing the easy axes of the antiferromagnetic grains randomly in space and then initializing the system by simulating field cooling. Afterwards, the evolution of the magnetization configuration with changing external field  $\mathbf{H}$  is investigated.

A Metropolis Monte Carlo algorithm is used to simulate field cooling. Usually, we start at an initial temperature  $T_i = 800$  K and decrease the temperature in steps of  $\Delta T = 25$  K towards zero. The direction of the ferromagnetic magnetization is fixed parallel to the y-axis, whereas the magnetization of the antiferromagnet is variable. Each Monte Carlo step starts by randomly picking out an antiferromagnetic grain and making three different trial steps to efficiently sample the phase space [10, 33]: A new magnetization direction of this antiferromagnetic grain is chosen

1. randomly within a cone of  $3^\circ$  opening angle (the symmetry axis of the cone is parallel to the old magnetization direction),
2. within any orientation on a sphere (this step is independent of the initial direction of the spin and thus guarantees ergodicity) and
3. as a simple reversal.

The change of the total energy  $E_{\text{tot}}$  of the system is computed according to Eq. (3.1) and summing up all grains. Finally, the trial step is accepted with the probability from the heat-bath algorithm. Without steps one and three the simulations would cost much more time since directions of lowest energy nearby the initial magnetization or the reversed spin direction would be found probably long after. At each temperature step  $2000 \cdot N_x \cdot N_y$  Monte Carlo steps are executed, where  $N_x$  and  $N_y$  denote the number of grains in x- and y-direction, respectively.

After field cooling ( $T \rightarrow 0$ ) an equilibrium configuration is obtained by the numerical integration of the LLG equation (Eq. (1.33)) at each magnetic field step. The direction of the external field  $\mathbf{H}$  is fixed parallel to the y-axis, whereas its absolute value varies with  $\Delta(\mu_0 H) = 2$  mT. However, to avoid unrealistic symmetry effects  $\mathbf{H}$  has a small x-component.

The effective field acting on the ferromagnetic grain  $j$  is given by (see Eq. (1.34))

$$\mathbf{H}_{\text{eff},F}^j = -\frac{1}{J_S t_F l^2} \left( \frac{\partial E_{\text{tot}}}{\partial \mathbf{u}_F^j} \right)_T . \quad (3.4)$$

$J_S t_F l^2$  represents the total ferromagnetic magnetization of grain  $j$ . Similar expressions

are used to compute the effective fields acting on the sublattice moments of the antiferromagnet (we use  $J_{S,AF} \approx J_{S,F} \equiv J_S$ ). The equilibrium state is approximately reached for  $\max\{|\mathbf{du}/dt|\} < 10^{-4}$ , where  $\max\{|\mathbf{du}/dt|\}$  gives the largest time derivative of all ferro- and antiferromagnetic unit vectors  $\mathbf{u}$ .

Since the system is supposed to be stiff (if one perturbs a state variable slightly, the system responds rapidly to return to equilibrium), a backward differentiation formula (BDF) is used for the numerical integration of the LLG equation [9]. This is the most effective multistep method, which makes use of several past values of  $\mathbf{y}$  (see Eq. (1.32)) and/or  $f(t, \mathbf{y})$  to attain a higher accuracy for the ODE.

We use the CVODE code for solving the LLG equation [4, 5]. Since the BDF method is implicit, a nonlinear algebraic system must be solved at each time step. The nonlinear system of equations is solved using a Newton method. For this purpose only a few Newton steps are required, leading to a very large system of linear equations. Within the CVODE code the system for each Newton step is solved with a Krylov subspace method [34, 37], which generates the solution iteratively by combining basis vectors of the Krylov subspace in a linear manner. At each iteration step a new orthonormal basis vector is added, increasing the dimension of the Krylov subspace by one. The exact solution is found if the number of unknowns equals the Krylov subspace dimension. However, only a few Krylov subspace iterations are necessary to obtain the required accuracy.

Instead of the exchange integrals  $J_F$ ,  $J_{AF}$  and  $J_{AF-F}$ , the program uses the exchange stiffness constants  $A_F$ ,  $A_{AF}$  and  $A_{AF-F}$ , satisfying the relations

$$A_F = \frac{J_F S^2}{a} \quad (3.5)$$

$$A_{AF} = \frac{J_{AF} S^2}{a} \quad (3.6)$$

$$A_{AF-F} = \frac{J_{AF-F} S^2}{a} \quad . \quad (3.7)$$

Additionally, we introduce the in-plane anisotropy constant

$$K_F = -\frac{J_S^2}{\mu_0} \quad (3.8)$$

of the ferromagnet and set

$$N_x = N_y \equiv N \quad . \quad (3.9)$$

The following table summarizes the material parameters chosen to approximate bilayer systems used in GMR read-heads, such as Permalloy/IrMn:

|            |     |                                  |          |     |                                 |
|------------|-----|----------------------------------|----------|-----|---------------------------------|
| $A_F$      | $=$ | $1 \cdot 10^{-12} \text{ J/m}$   | $t_F$    | $=$ | $10 \cdot 10^{-9} \text{ m}$    |
| $A_{AF}$   | $=$ | $0.5 \cdot 10^{-13} \text{ J/m}$ | $t_{AF}$ | $=$ | $20 \cdot 10^{-9} \text{ m}$    |
| $A_{AF-F}$ | $=$ | $-1 \cdot 10^{-12} \text{ J/m}$  | $l$      | $=$ | $10 \cdot 10^{-9} \text{ m}$    |
| $K_1$      | $=$ | $1 \cdot 10^5 \text{ J/m}^3$     | $a$      | $=$ | $3.76 \cdot 10^{-10} \text{ m}$ |
| $K_F$      | $=$ | $-1 \cdot 10^6 \text{ J/m}^3$    | $T_i$    | $=$ | $800 \text{ K}$                 |
| $\alpha$   | $=$ | $1$                              | $N$      | $=$ | $50 \text{ or } 60$             |
| $J_S$      | $=$ | $1 \text{ T}$                    |          |     |                                 |

These are the *standard parameters* of the computer simulations. In the following chapters some of the parameters are varied systematically. Only those with differing values are quoted, whereas the unchanged quantities can be looked up in this table.

## Technical Parameters

**Damping constant:** The results are almost independent of  $\alpha$  within a relatively wide range. However, the limits are more or less unclear. For too small damping constants the simulations become very time expensive, whereas numerical problems occur for too high values of  $\alpha$ .  $\alpha = 1$  seems to be a good compromise.

**Initial temperature:**  $T_i$  affects the magnetization configuration of the antiferromagnet after field cooling. The initial temperature has to be high enough to enable the antiferromagnet to minimize the total Gibbs free energy. We have found that  $T_i \approx 800 \text{ K}$  satisfies this condition. Beyond  $800 \text{ K}$  the magnetization configuration and the associated energy do not change essentially. For example, we found for the standard parameters and  $T_i = 1200 \text{ K}$  an energy difference in the remanent state after field cooling of less than 1% and hardly any differences in the hysteresis cycles.

**Stepsize of the external field:** The evolution of the calculated magnetization configuration is almost independent of the stepsize  $\Delta(\mu_0 H)$ . However, for a satisfying resolution (primarily of the hysteresis cycle) we choose  $\Delta(\mu_0 H) = 2 \text{ mT}$ .

# Chapter 4

## Results of the Interacting Grain Model

### 4.1 Conventions and Methods

#### 4.1.1 Magnetization States

In order to simplify the discussion of the results, we introduce the following notation for the most important points of the hysteresis cycle (see Fig. 4.1):

- S ... positive saturated state,  $\mathbf{J}$  (approximately) parallel to the y-axis
- $\bar{S}$  ... negative saturated state,  $\mathbf{J}$  (approximately) antiparallel to the y-axis
- R ... positive remanent state
- $\bar{R}$  ... negative remanent state
- C ... right intersection point with the magnetic field axis
- $\bar{C}$  ... left intersection point with the magnetic field axis

Additionally, an index number indicates the number of the hysteresis cycle ( $R_2$  for example means the positive remanent state of the second hysteresis cycle).

#### 4.1.2 Irreversible Switching

We have to distinguish between reversibly and irreversibly switched antiferromagnetic grains (or, in a shorter manner, not switched or switched grains) and have a look at the dependence of the bias field on the arrangement of the switched grains.

An antiferromagnetic grain  $j$  has made an *irreversible transition* when the relation

$$\frac{\mathbf{k}_{AF}^j \cdot \mathbf{u}_{AF,\bar{R}}^j}{|\mathbf{k}_{AF}^j \cdot \mathbf{u}_{AF,\bar{R}}^j|} = - \frac{\mathbf{k}_{AF}^j \cdot \mathbf{u}_{AF,R}^j}{|\mathbf{k}_{AF}^j \cdot \mathbf{u}_{AF,R}^j|} \quad (4.1)$$

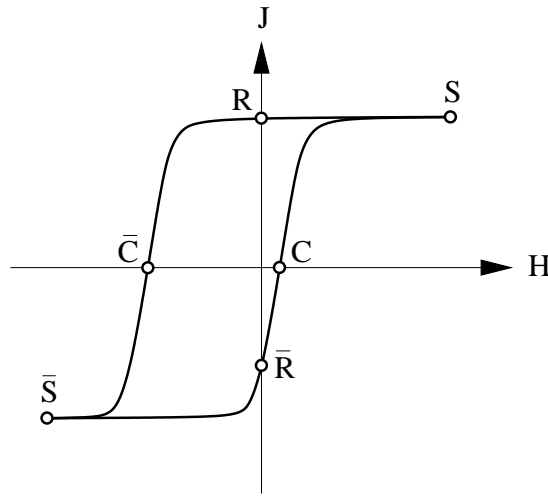


**Figure 4.1:** Important points of the hysteresis cycle.

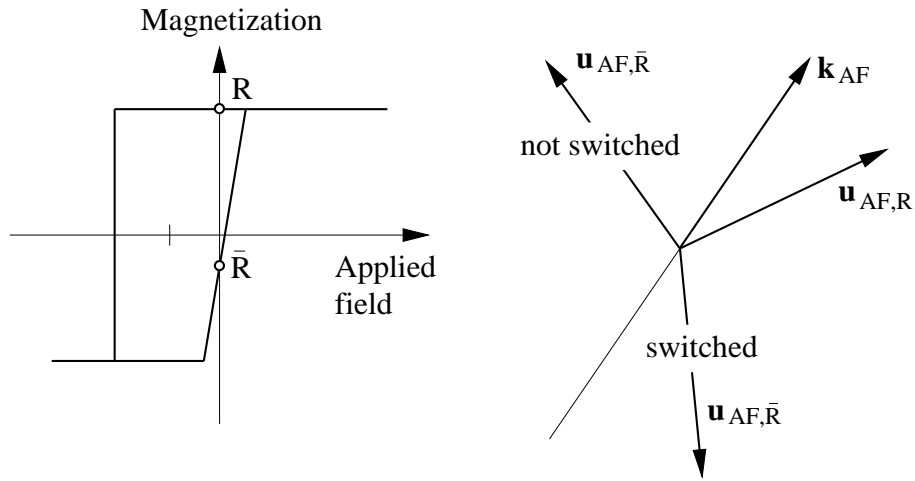


**Figure 4.2:** Difference between reversible and irreversible switching. For an irreversible transition the inner product  $\mathbf{k}_{AF} \cdot \mathbf{u}_{AF}$  changes its sign.

is fulfilled (see Fig. 4.2).  $\mathbf{u}_{AF,R}^j$  and  $\mathbf{u}_{AF,\bar{R}}^j$  denote the directions of the antiferromagnetic sublattice magnetization in the positive and negative remanent state, respectively. Fig. 4.2 makes clear that an angle of greater than  $90^\circ$  between  $\mathbf{u}_{AF,R}$  and  $\mathbf{u}_{AF,\bar{R}}$  is not a sufficient condition for irreversible transitions. On the other hand, irreversible transitions may occur for angles less than  $90^\circ$ .

At first sight one could presume to find the largest unidirectional anisotropy for  $s = 50\%$ , where  $s$  designates the percentage of switched grains. A closer look reveals that the arrangement of the switched grains strongly affects the exchange bias field since the interacting grain (IG) model explains exchange bias as a consequence of domain walls in the antiferromagnet. Fig. 4.3 shows different arrays of  $8 \times 8$  antiferromagnetic grains.



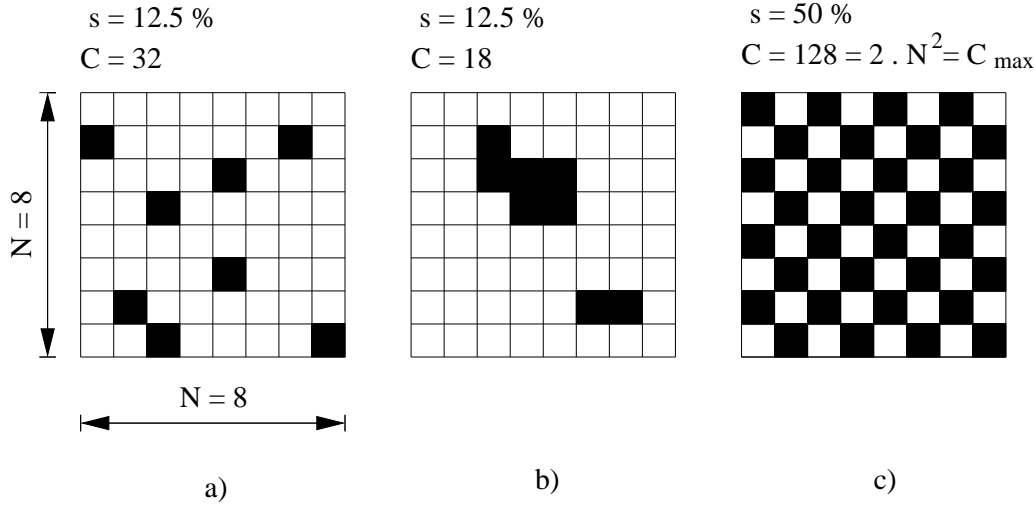


**Figure 4.3:** Irreversible and reversible transitions in an antiferromagnetic layer. Black squares represent irreversibly switched grains, whereas reversibly switched grains are white. The configurations a) and b) only differ in the circumference of the black areas. Fig. c) shows the arrangement with  $C_{\max}$  (periodic boundary conditions).

Irreversibly switched grains are indicated black, whereas the others made reversible transitions. Both Fig. 4.3.a and Fig. 4.3.b lead to  $s = 12.5 \%$ , whereas the circumferences  $C$  (in arbitrary units) between switched and not switched grains are not the same. Since  $C$  of Fig. 4.3.b is much smaller than for the left array, configuration 4.3.a would exhibit a larger domain wall energy and hence a greater exchange bias field.

The highest possible value of  $C$  is found for the arrangement of Fig. 4.3.c.  $s = 50 \%$  and a maximal splitted configuration yield the theoretical limit (for periodic boundary conditions)

$$C_{\max} \approx 2 \cdot N^2 \quad . \quad (4.2)$$

### 4.1.3 Centerline of the Hysteresis Cycle

As mentioned above, Stiles and McMichael [31] noticed that formula (2.1) for the calculation of the exchange bias field is possibly not the correct way to find  $H_{\text{eb}}$ . Hence, we introduce a new method to calculate an exchange bias field  $\tilde{H}_{\text{eb}}$  for given hysteresis curves.

The total work done on a ferromagnetic material to change the polarization  $J$  from  $J_1$  to  $J_2$  is

$$A_{1 \rightarrow 2} = \int_{J_1}^{J_2} H(J) \, dJ \quad . \quad (4.3)$$

$A_{1 \rightarrow 2}$  is the area between the hysteresis cycle and the polarization axis as depicted in

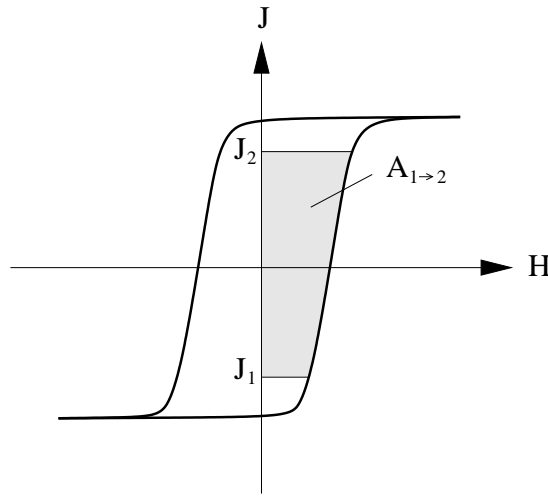


**Figure 4.4:** Total work  $A_{1 \rightarrow 2}$  to change the polarization from  $J_1$  to  $J_2$ .

Fig. 4.4 and consists of heat losses (the most part) and the stored energy difference between state 1 and 2 [15].

Now suppose an unbiased ferromagnetic layer in an external field. Fig. 4.5.a shows the hysteresis curve.  $A_{R \rightarrow \bar{R}}$  denotes the total work for reversing the magnetization vector from the positive remanent state (R) to the negative remanent state ( $\bar{R}$ ) (see Fig. 4.5.a). Analogously,  $A_{\bar{R} \rightarrow R}$  is the total work to rotate the magnetization vector back to R. Since only *uniaxial* anisotropies are considered in the unbiased film, the two energies satisfy the relation  $A_{R \rightarrow \bar{R}} = A_{\bar{R} \rightarrow R}$ . That is to say, the reversal mechanisms for increasing and decreasing external field are the same.

For very small ferromagnetic samples it is possible to find deviations in the reversal mechanisms although the film is unbiased. But in the following we leave this origin of asymmetric hysteresis cycles out of consideration.

For biased ferromagnetic films the antiferromagnet induces a *unidirectional* anisotropy in the ferromagnet, i.e. the energies  $A_{R \rightarrow \bar{R}}$  and  $A_{\bar{R} \rightarrow R}$  are not equal anymore (see Fig. 4.5.b). The exchange bias field usually opposes the external field during field cooling. Accordingly, we obtain  $A_{R \rightarrow \bar{R}} > A_{\bar{R} \rightarrow R}$ . That is, an additional amount of work is required to reverse the ferromagnet to the negative remanent state. The centerline, drawn in Fig. 4.5.b, subdivides the area within the hysteresis cycle into two areas, equal in size. The hatched area between the centerline and the y-axis is the unidirectional anisotropy energy  $A_{\text{ani}}$  due to the coupling to the antiferromagnet. Hence, the distance between the centerline and the polarization axis,  $\tilde{H}_{\text{eb}}$ , is probably a better measure for the exchange bias field.

From this point of view it is not surprising when we find positive exchange bias fields

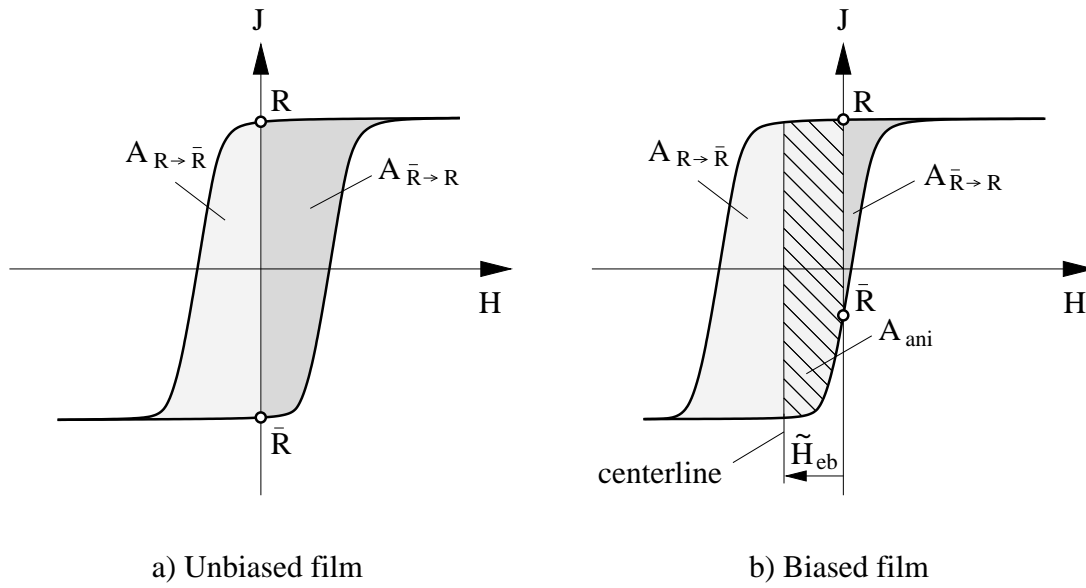


**Figure 4.5:** Hysteresis cycles of an unbiased a) and a biased b) ferromagnetic layer. The gray areas indicate the total work required to rotate the ferromagnetic magnetization from the positive (R) to the negative ( $\bar{R}$ ) remanent state and vice versa, respectively. Locating the centerline of the shifted hysteresis cycle leads to  $\tilde{H}_{eb}$ .

although the total energy of the positive remanent state is lower than for the reversed state. This is possible if more irreversible work is done for the backward rotation.

It is worth noting that a large energy difference  $\Delta E_{\text{tot}}$  between the states R and  $\bar{R}$  only decreases the probability to find positive exchange bias, because  $\Delta E_{\text{tot}}$  tries to fix the ferromagnetic magnetization parallel to the positive y-axis. Stable configurations enhancing the irreversible work are much more probable to occur for the transition  $R \rightarrow \bar{R}$  than for  $\bar{R} \rightarrow R$ . Moreover, it is possible to approximate the energy difference  $\Delta E_{\text{tot}}$  analytically (see chapter 2). But owing to the fact that stable configurations in the ferromagnet like  $360^\circ$  domain walls seem to appear unpredictably, it remains unclear how one could give an expression for the exchange bias field based on a given set of parameters.

To obtain the exchange bias field  $\tilde{H}_{eb}$  we use the procedure depicted in Fig. 4.6. We split the magnetization curve into two graphs and calculate their difference. Afterwards, we integrate the new curve yielding the total area within the hysteresis cycle. The centerline is located at the half maximum of the integrated curve. For most cases the relation  $H_{eb} \approx \tilde{H}_{eb}$  is fulfilled. However, relatively large deviations of about 20 % or more also occur, namely for the appearance of remarkably stable magnetization configurations in the ferromagnet (such as  $360^\circ$  domain walls), leading to stepped hysteresis cycles.

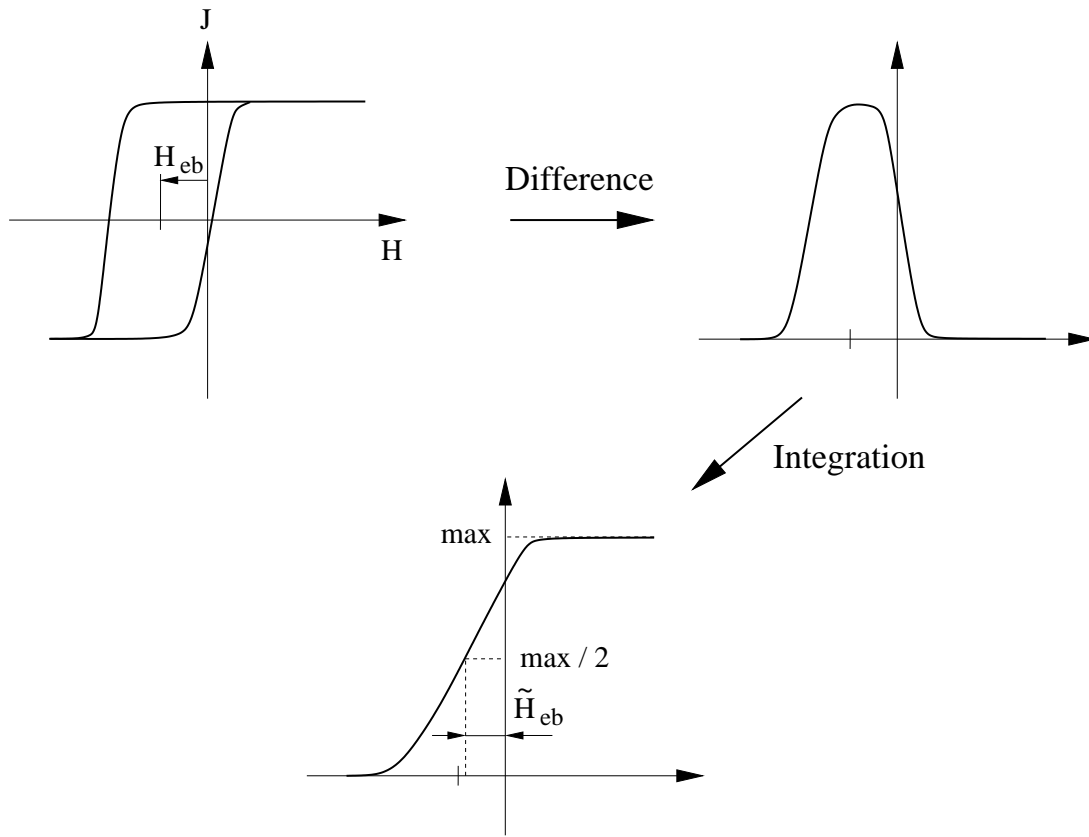


**Figure 4.6:** Schematic illustration of the calculation of  $\tilde{H}_{\text{eb}}$ .

#### 4.1.4 Designation of the Bias Fields

In the following simulations we always calculate both  $H_{\text{eb}}$  (according to Eq. (2.1)) and  $\tilde{H}_{\text{eb}}$  for the **first hysteresis loop**. Negative (or normal) bias fields are represented in **absolute values**, whereas a positive shift of the hysteresis curve is indicated by bars (e.g.  $\bar{2}$  mT).

## 4.2 Results for the Standard Parameters

### 4.2.1 Hysteresis

Fig. 4.7 shows the hysteresis curves for the first, third and fifth cycle. The training effect leads to a decrease of the exchange bias field and coercivity with increasing cycle number  $n$ . Cycle 3 exhibits a distinct knee between the states  $\bar{C}$  and  $\bar{S}$ , emphasizing the fact that different mechanisms are responsible for the transitions  $R \rightarrow \bar{R}$  and  $\bar{R} \rightarrow R$ . The equilibrium state is achieved after the fifth cycle, i.e. deviations of following curves are negligible.

In experiments usually more cycles are required to reach the equilibrium state. According

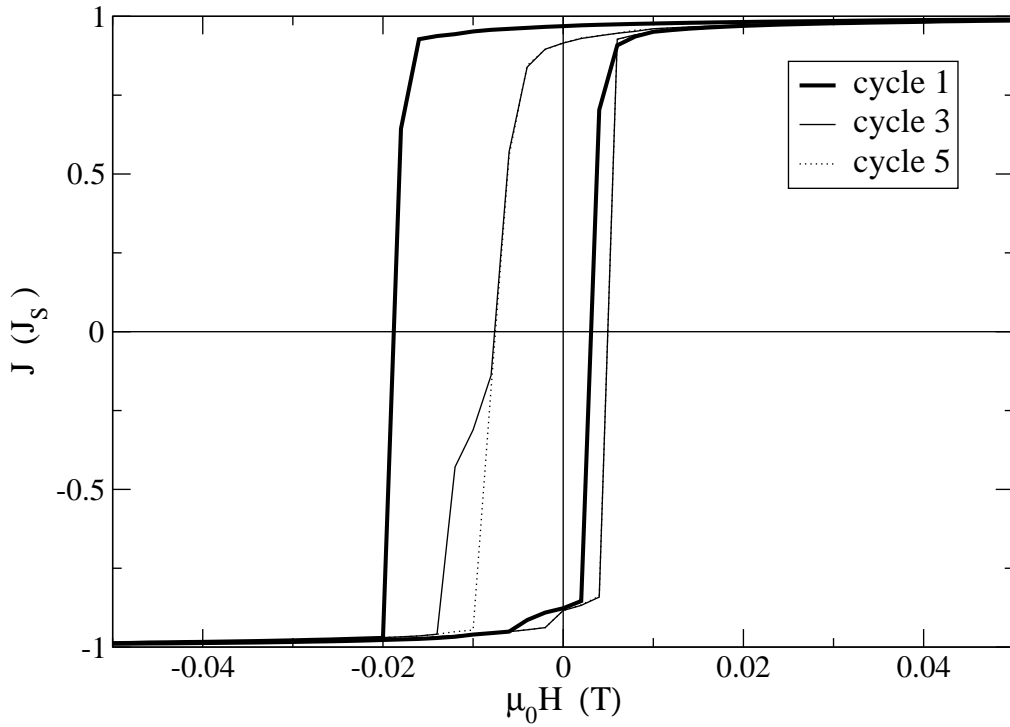


**Figure 4.7:** Hysteresis curves for the standard parameters. The equilibrium state is reached after the fifth cycle.

to Eq. (2.3) the exchange bias field decreases with  $n^{-1/2}$ . However, our simulations resulted in a more rapid decrease of the bias field, as depicted in Fig. 4.8.

After field cooling the system is in its absolute energy minimum or in a very low energy state, respectively. The switching of the ferromagnet from  $R \rightarrow \bar{R}$  causes several antiferromagnetic grains to make irreversible transitions (see Fig. 4.9, left column). When the ferromagnet rotates back ( $\bar{R} \rightarrow R$ ), not all antiferromagnetic grains switch back again. After the first cycle a considerable number of grains maintain their new direction (Fig. 4.9, right column). Due to the intergrain coupling not switched grains are affected as well. Instead of the original configuration the pinning layer occupies a *local* energy minimum. To reach the *global* minimum again, an additional amount of energy would be required because of energy barriers between different minima. In contrast to the ferromagnet, where a stronger external field leads to a polarization vector more parallel to the y-axis, the alignment of the antiferromagnet by the ferromagnet is limited to the interfacial coupling strength. Only a further heat treatment could rearrange the antiferromagnet in order to minimize the total energy again because thermal activation may help to overcome energy barriers. Actually, finite temperatures could be the reason for a much slower decrease of the experimentally found bias fields. However, the temperature dependence of the exchange bias field in the IG model remains to be investigated.

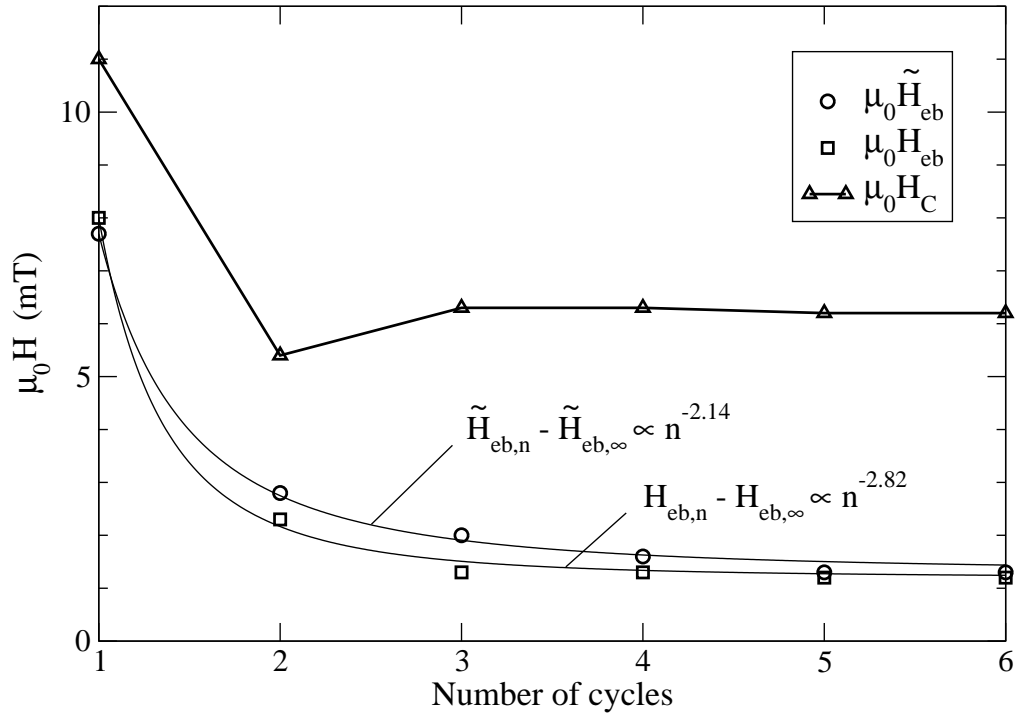


**Figure 4.8:** The training effect causes the decrease of the exchange bias field and the coercive field with increasing cycle number  $n$ . A non-linear curve fitting (thin lines) reveals a more rapid decrease of the bias field than experimentally found.

After the first cycles still a lot of antiferromagnetic grains switch irreversibly from  $R \rightarrow \bar{R}$ . But since almost all grains rotate back again, there is no remarkable training effect anymore. In a simplified picture the system rapidly chooses a certain closed path through the possible magnetization configurations. That is to say, the system reaches a kind of dynamic equilibrium.

### 4.2.2 Energy terms

In the following we discuss the contributions to the total energy Eq. (3.1) except for the in-plane anisotropy energy of the ferromagnet and the Zeeman energy, because they do not lead to a deeper insight of the phenomenon of exchange bias. The energy terms strongly depend on the history of the sample and thus originate the training effect.

**Exchange energy of the ferromagnet:** Fig. 4.10 shows the exchange energy of the ferromagnet. Starting at  $S_1$  the energy  $E_{ex,F}$  increases with decreasing external field due to domain formation within the ferromagnet, caused by the coupling to the antiferromagnet with randomly distributed easy axes. At the distinct peak ( $\mu_0 H \approx -18$  mT) the external field is high enough to rotate the ferromagnet, i.e. the exchange energy of the ferromagnet has become too high. A further decrease of the magnetic field annihilates ferromagnetic

domains and thus decreases  $E_{\text{ex,F}}$ . For the transition  $\bar{S}_1 \rightarrow S_2$  the ferromagnetic exchange energy behaves analogously.

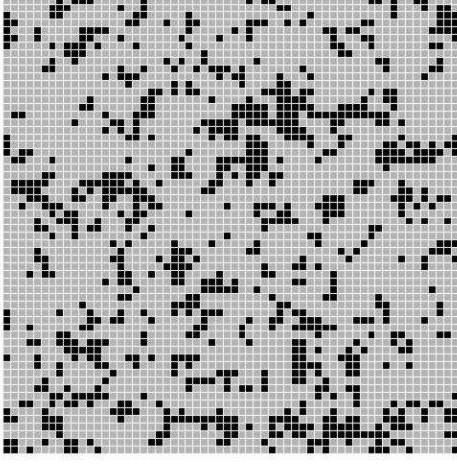
**Exchange energy of the antiferromagnet:** This energy is depicted in Fig. 4.11. When the ferromagnet rotates, about 24% of the antiferromagnetic grains switch irreversibly, giving rise to a dramatic change of  $E_{\text{ex,AF}}$ . If one compares the energy differences  $\Delta E_{\text{ex,AF},\bar{R}_1-R_1} \approx 3.4 \cdot 10^{-17}$  J and  $\Delta E_{\text{tot},\bar{R}_1-R_1} \approx 3.7 \cdot 10^{-17}$  J, one finds that  $E_{\text{ex,AF}}$  is almost completely responsible for the asymmetry of the states  $R_1$  and  $\bar{R}_1$ . This result is in agreement with our explanation of the origin of exchange bias, given in Sec. 3.2: The energy involved in forming domain walls between antiferromagnetic grains generates the shift of the hysteresis loop. When the ferromagnet rotates back, approximately half of the antiferromagnetic grains do not switch back. As one expects, the energy difference between the states  $S_2$  and  $S_1$  is  $1.7 \cdot 10^{-17}$  J, i.e. half of the energy difference between  $\bar{R}_1$  and  $R_1$ .

**Interface energy:** Fig. 4.12 shows the interface or spin flop energy.  $E_{\text{inter}}$  decreases slightly with decreasing  $H$ , down to the external field where the ferromagnet switches.  $E_{\text{inter}}$  then increases due to rearrangements of ferro- and antiferromagnetic spins.

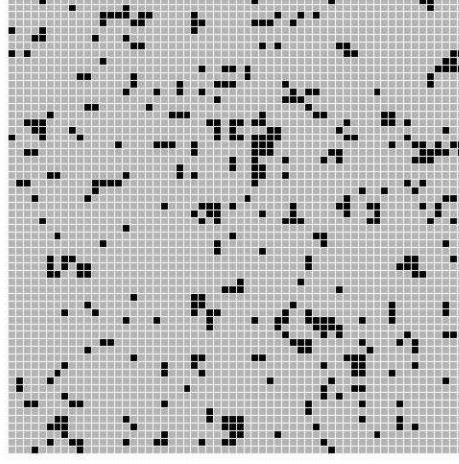
**Anisotropy energy of the antiferromagnet:**  $E_{\text{ani,AF}}$  is shown in Fig. 4.13. Owing to the coupling of the antiferromagnet to the ferromagnet and the exchange coupling among antiferromagnetic grains the antiferromagnetic spins are not parallel to the easy axes. When the external field decreases, starting at  $S_1$ , ferromagnetic domains are formed because the antiferromagnet tries to reduce its anisotropy energy. Hence,  $E_{\text{ani,AF}}$  drops with decreasing external field. Below  $H = 0$  the magnetization distribution in the ferromagnet becomes more and more perturbed. This permits a further relaxation of the antiferromagnetic spins, since the external field does not affect the antiferromagnet. After reversal, the ferromagnet shows a relatively uniform magnetization configuration again, yielding larger angles between the antiferromagnetic polarization vectors and their easy directions. Thus,  $E_{\text{ani,AF}}$  increases continuously until  $\bar{S}_1$  is reached. For  $\bar{S}_1 \rightarrow S_2$  the energy  $E_{\text{ani,AF}}$  behaves very similar.

**Total energy:**  $E_{\text{tot}}$  is presented in Fig. 4.14. For a symmetric range of the external field the system always has the lowest total energy at  $S_1$ , that is after field cooling. Even though hysteresis loops are calculated at zero temperature, the original configuration after field cooling will never appear again as the field is cycled further. The Zeeman term in Eq. (3.1) is the reason for the linear decrease of  $E_{\text{tot}}$  as  $H$  increases, although the ferromagnet is almost saturated. The ratio  $\Delta E_{\text{ex,AF},S_2-S_1} / \Delta E_{\text{tot},S_2-S_1} \approx 0.85$  reveals that the training effect has its roots mainly in the exchange energy of the antiferromagnet. The largest training effect occurs for the first cycle.

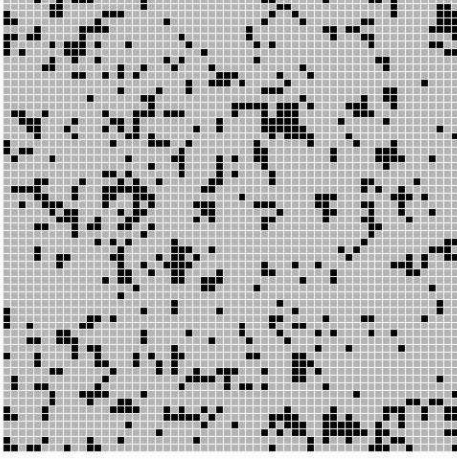
$R_1/\bar{R}_1$   $s = 24.1\%$  ,  $C/C_{\max} = 26.9\%$



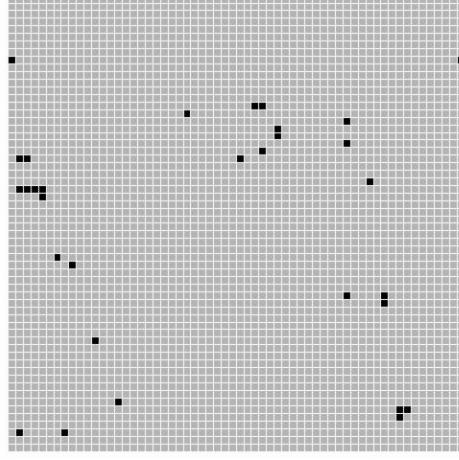
$R_1/R_2$   $s = 11.1\%$  ,  $C/C_{\max} = 16.1\%$



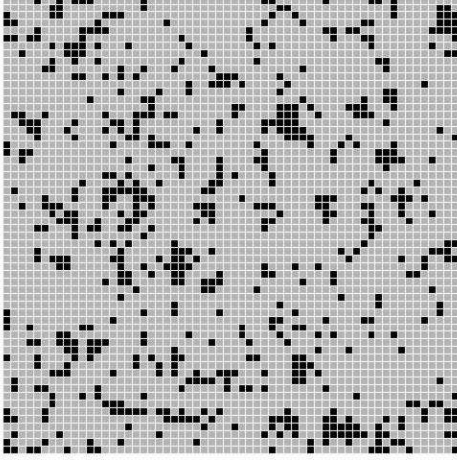
$R_2/\bar{R}_2$   $s = 18.1\%$  ,  $C/C_{\max} = 23.2\%$



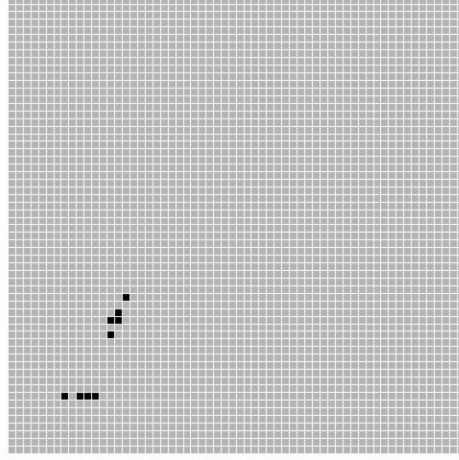
$R_2/R_3$   $s = 0.9\%$  ,  $C/C_{\max} = 1.4\%$



$R_4/\bar{R}_4$   $s = 17.5\%$  ,  $C/C_{\max} = 22.9\%$



$R_4/R_5$   $s = 0.3\%$  ,  $C/C_{\max} = 0.4\%$



120 nm

**Figure 4.9:** Images of the pinning layer. Black squares indicate switched antiferromagnetic grains. The left column shows switched grains for the transition  $R \rightarrow \bar{R}$ , whereas the right column shows the situation for a whole cycle. Due to the weak antiferromagnetic intergrain coupling the antiferromagnetic grains switch individually rather than in clusters. After the first cycles the pattern of switched grains remains nearly the same.



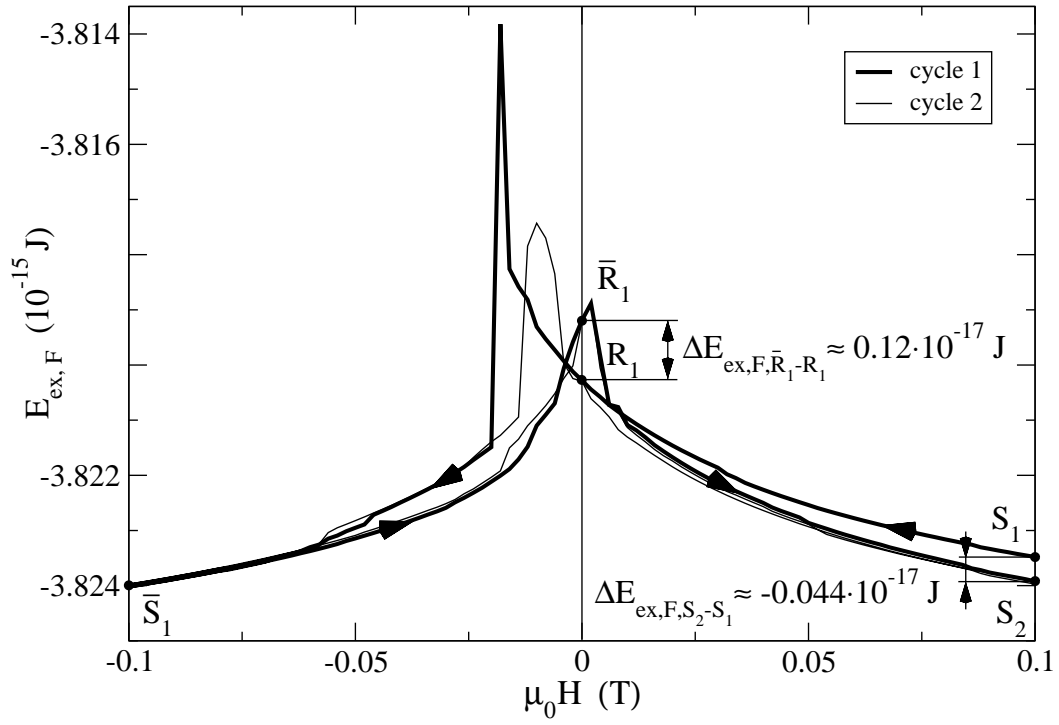


**Figure 4.10:** Exchange energy of the ferromagnet for the cycles 1 and 2. The peaks indicate the external fields where the ferromagnet switches.

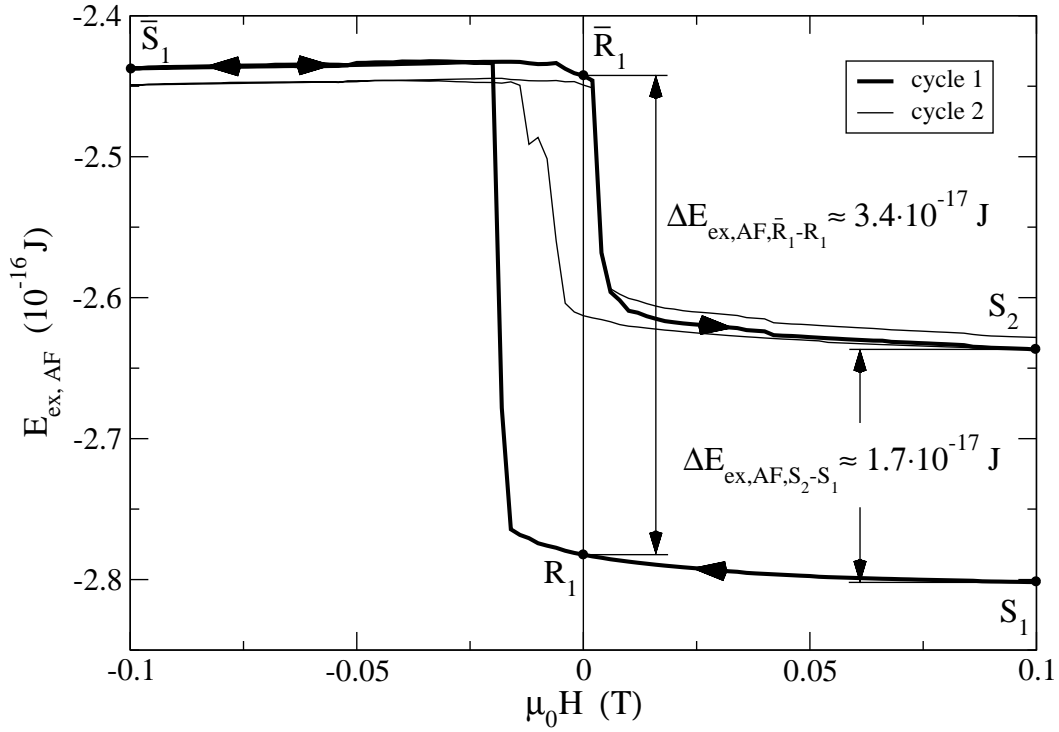


**Figure 4.11:** The exchange energy of the antiferromagnet is mainly responsible for the asymmetry of the remanent states  $R_1$  and  $\bar{R}_1$  and for the training effect.

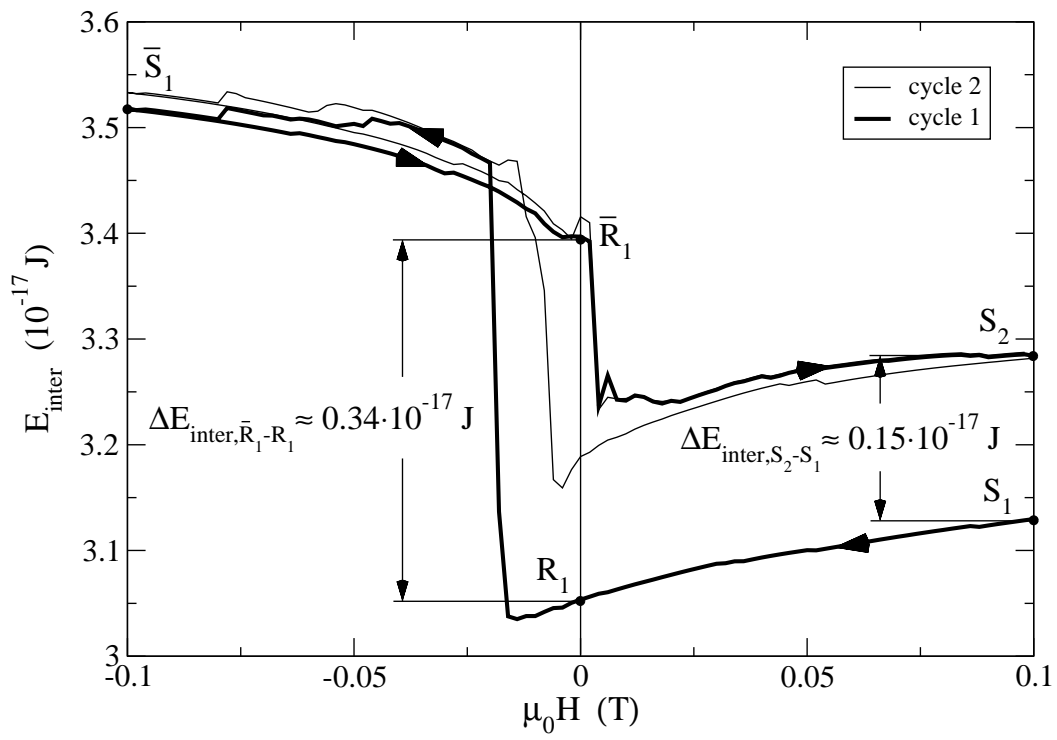


**Figure 4.12:** Interface or spin flop energy. The jump in  $E_{\text{inter}}$  indicates the switching of the ferromagnet and is due to rearrangements of ferro- and antiferromagnetic spins.

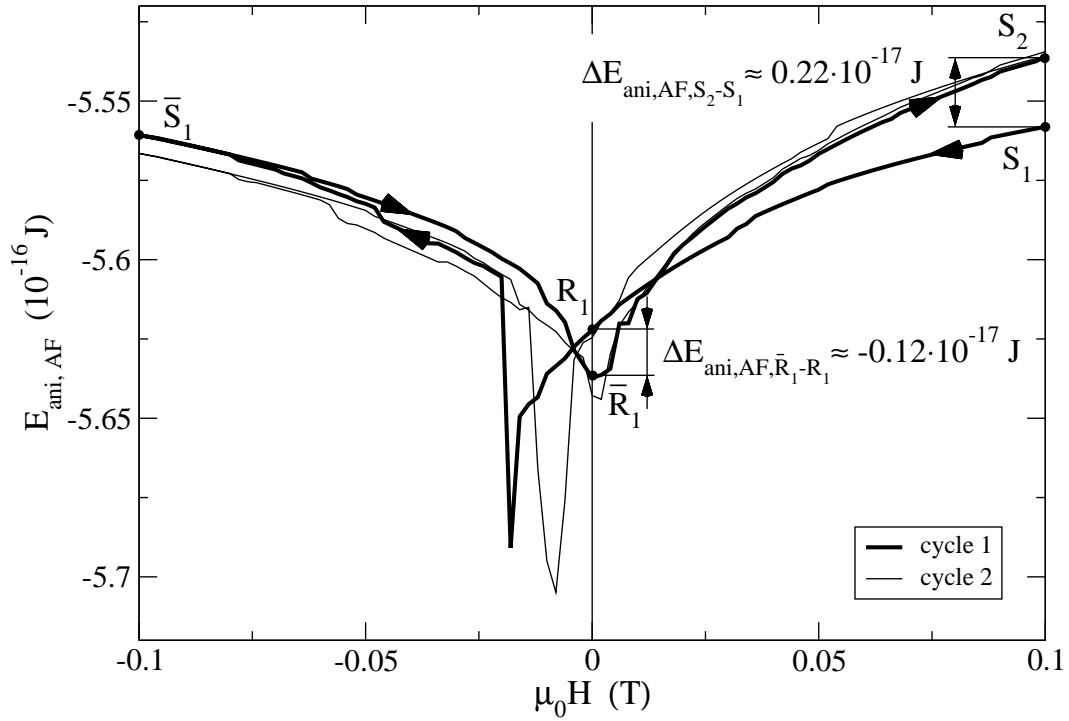


**Figure 4.13:** Starting at  $S_1$ , the anisotropy energy of the antiferromagnet decreases down to where the ferromagnet reverses. The misalignment of the ferromagnet enables the antiferromagnetic spins to relax towards the easy axes.

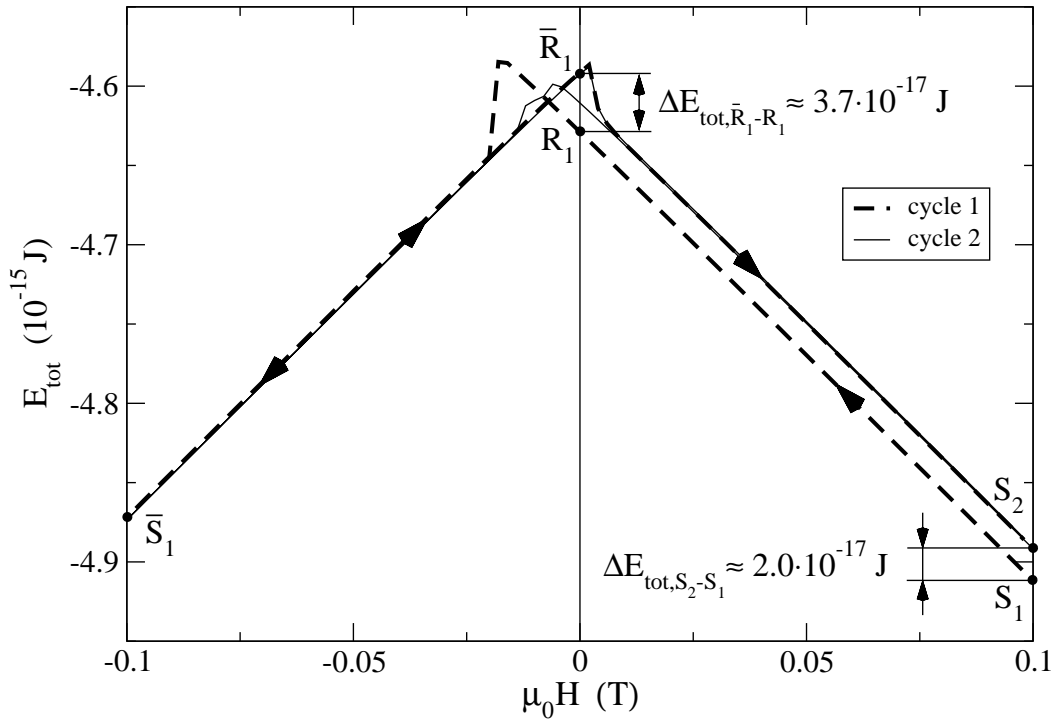


**Figure 4.14:** Total energy given by Eq. (3.1). The energy after field cooling ( $S_1$ ) is never reached again, although the process takes place at zero temperature. Cycle 1 shows by far the largest training effect.

### 4.2.3 Magnetization Configuration

Ferromagnetic and antiferromagnetic domains have an important effect on the exchange bias field. Thus, ferromagnetic domain formation has been studied using several techniques, such as Bitter method, Kerr effect, Lorentz microscopy, Faraday effect or magnetic force microscopy. These techniques only allow studies of the ferromagnetic surface domain formation perpendicular to the interface. Domains parallel to the interface cannot be observed. The detailed behavior of the domain structure depends on the system parameters. Usually the domain structure in exchange biased systems is more complex (that is more sizes, shapes and types of domains) than for single ferromagnetic layers. In the following we discuss the magnetization configuration of both layers and the observed correlation for the standard parameters.

The magnetization configuration of the ferromagnet at  $R_1$  is shown in Fig. 4.15. The domain structure is mainly affected by the exchange constant  $A_F$ . For  $A_F = 1 \cdot 10^{-12}$  J pronounced uniformly magnetized regions dominate. The domain size is approximately 15 grains or, with a grain diameter  $l = 10$  nm, 150 nm. If one applies a negative external field, some regions of the ferromagnet start to rotate clockwise, whereas other regions rotate counterclockwise. One is able to distinguish these regions already in the remanent

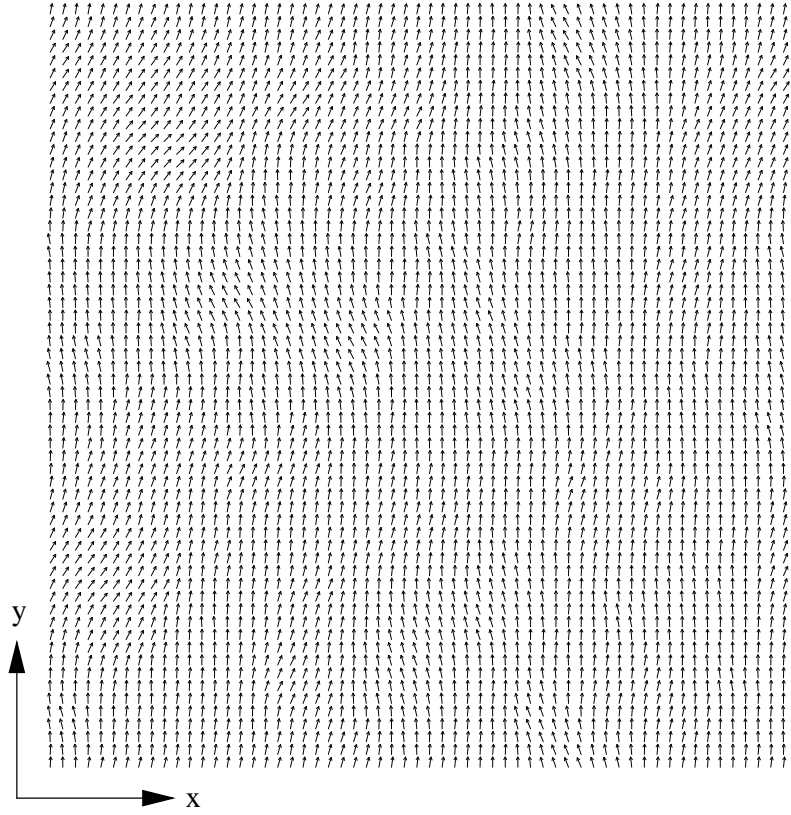


**Figure 4.15:** Ferromagnetic spin configuration in the positive remanent state  $R_1$ . Pronounced domains with a diameter of about 15 grains ( $= 150$  nm) dominate. When a negative external field is applied, some regions rotate clockwise and others counterclockwise. These regions can already be distinguished in the remanent state.

state. The direction of rotation is predefined by the antiferromagnet. For decreasing and increasing fields rotation takes place in opposite directions. This means that parts of the system rotate irreversibly in high rotational field measurements but not in magnetization reversal [31].

Fig. 4.16 presents ferromagnetic (left column) and antiferromagnetic (right column) spin configurations parallel to the  $x$ -axis at  $R_1$ ,  $\bar{R}_1$  and  $R_2$ , indicated by a color scale. Note that only one sublattice of the antiferromagnet is shown. Relatively large domains of about 100 nm on average are formed in the antiferromagnet although the easy axes are randomly distributed in space. This is consistent with thermal annealing and cooling at high fields which favors formation of uniform domains with a minimum of domain boundary walls.

Reversing the ferromagnet from  $R_1$  to  $\bar{R}_1$  causes several antiferromagnetic grains to make irreversible transitions. The initially large domains of the antiferromagnet parallel to the  $x$ -axis therefore break up into a number of smaller domains, increasing the domain wall

energy (see also Fig. 4.11). This means that the number of antiferromagnetic domains increases when the external field opposes the field cooling direction. The domain size stabilizes as the domain wall energy balances the energy gained by aligning with the ferromagnet, i.e. the spin flop energy. Rotating the ferromagnet back to the positive remanent state  $R_2$ , both spin configurations differ from those of  $R_1$ . The antiferromagnetic domains are smaller ( $\approx 60$  nm) as compared with the initial configuration due to the fact that several grains do not switch back again. This is the origin of the training effect as mentioned in the last section. The ferromagnetic domains increase just as the antiferromagnetic ones decrease. At  $R_2$  the domain size is approximately 25 grains or 250 nm on average.

For the ferromagnet the perturbation generated by an antiferromagnet with smaller domains varies faster in space than for larger domains. However, the ferromagnetic exchange coupling tries to even out disordering forces. The smaller the typical length of changes of the perturbation, the better is the compensation and thus larger ferromagnetic domains occur in the remanent state (compare  $R_1$  and  $\bar{R}_1$  in Fig. 4.16). This is valid for antiferromagnetic domains much larger than the ferromagnetic domain wall width ( $\delta \approx 10$  nm for the standard parameters, see Sec. 4.3.2). For antiferromagnetic domain sizes comparable to  $\delta$ , an additional reduction of the antiferromagnetic domains does not affect the domain size of the ferromagnet. Far away from the ferromagnetic domain wall width the relation

$$d_F \approx d_{F,R_1} \cdot \frac{d_{AF,R_1}}{d_{AF}} \quad (4.4)$$

seems to be fulfilled.  $d_{F,R_1}$  and  $d_{AF,R_1}$  denote the domain sizes of the ferromagnet and antiferromagnet at  $R_1$ , respectively, and  $d_F$  and  $d_{AF}$  are those of any remanent state (positive or negative).

Each cycle through the magnetization loop brings the system closer to its dynamic equilibrium in which the hysteresis curve remains constant. Apparently, the first hysteresis loop causes the largest change of the spin configuration, whereas additional cycles do not alter the domain structure for the standard parameters significantly.

It is interesting that the position of the domains does not change, apart from the fact that they become larger or smaller. The configuration after field cooling roughly determines the pending behavior of the system when an external field is applied. This is in agreement with experimental results. For example, King et al. [14] found that the way in which reversal took place was quite reproducible. Additionally, the same group found that local regions which had been the last to reverse under a decreasing field were the first to return to their original direction as the field was increased. We observed the same characteristic behavior.

Fig. 4.17 shows the antiferromagnetic spin configurations parallel to the y- and z-axis, respectively. Almost no domains are formed along the y-direction because the spin flop coupling pushes the antiferromagnetic spins towards the xz-plane. Therefore, the y-component is not free to form domains. Owing to the stray field energy the ferromagnetic spins rotate within the film plane, that is around the z-axis. The z-component of the antiferromagnetic spins shows distinct domains which are almost independent of the ferromagnetic spin configuration. Antiferromagnetic grains with spins almost perpendicular to the film plane do not switch and thus determine the direction of the domains. Even if adjacent grains switch, their z-component remain nearly unaffected because of exchange coupling to unswitched grains. Therefore, the domains along the z-axis are nearly static in size and position.

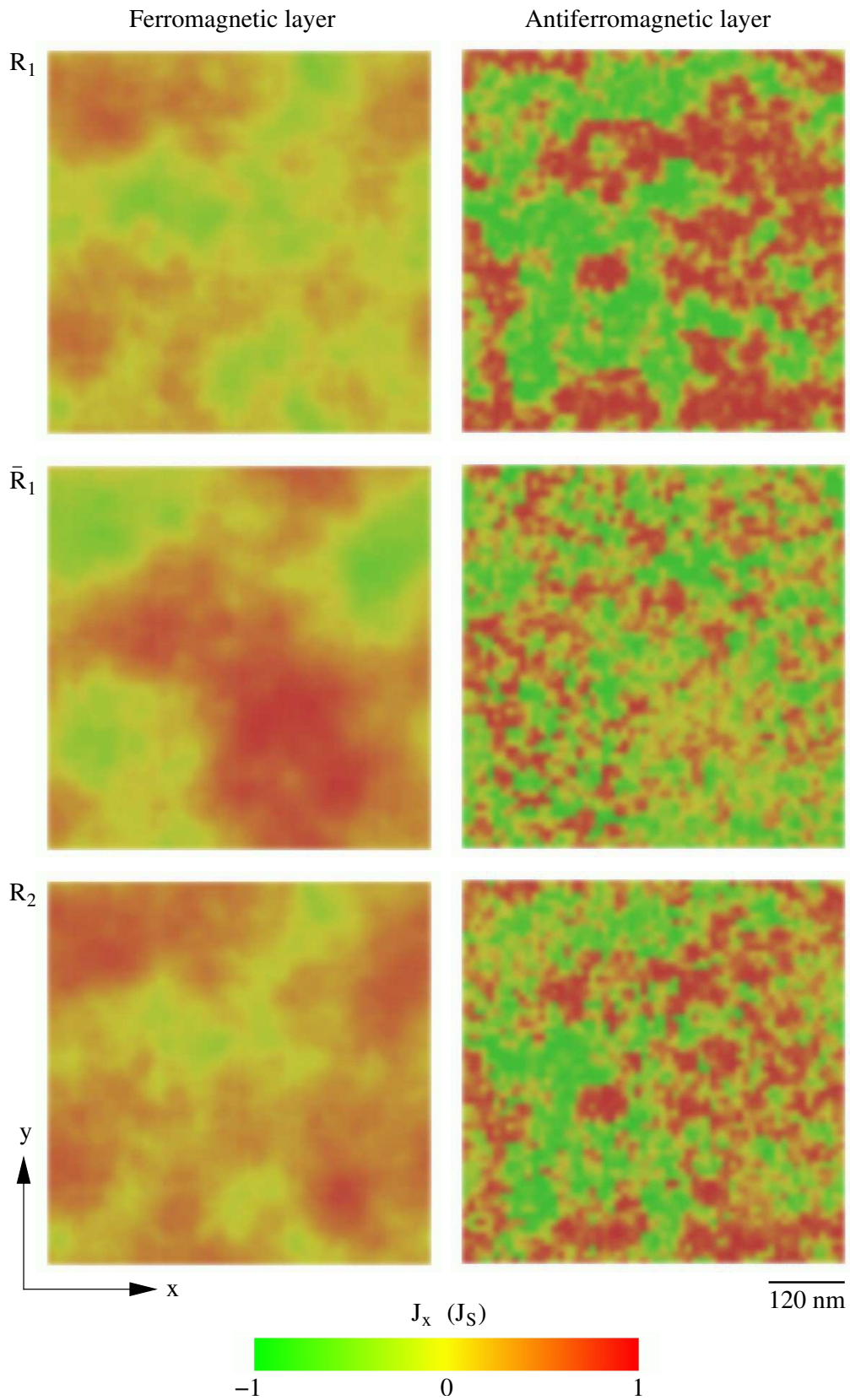


**Figure 4.16:** Domains in the ferromagnet (left column) and antiferromagnet (right column) along the x-axis at different points of the hysteresis curve. When the ferromagnet is reversed ( $\bar{R}_1$ ), the relatively large antiferromagnetic domains break up into a number of smaller domains. The antiferromagnet does not reach the initial spin configuration again when the ferromagnet is rotated back ( $R_2$ ).

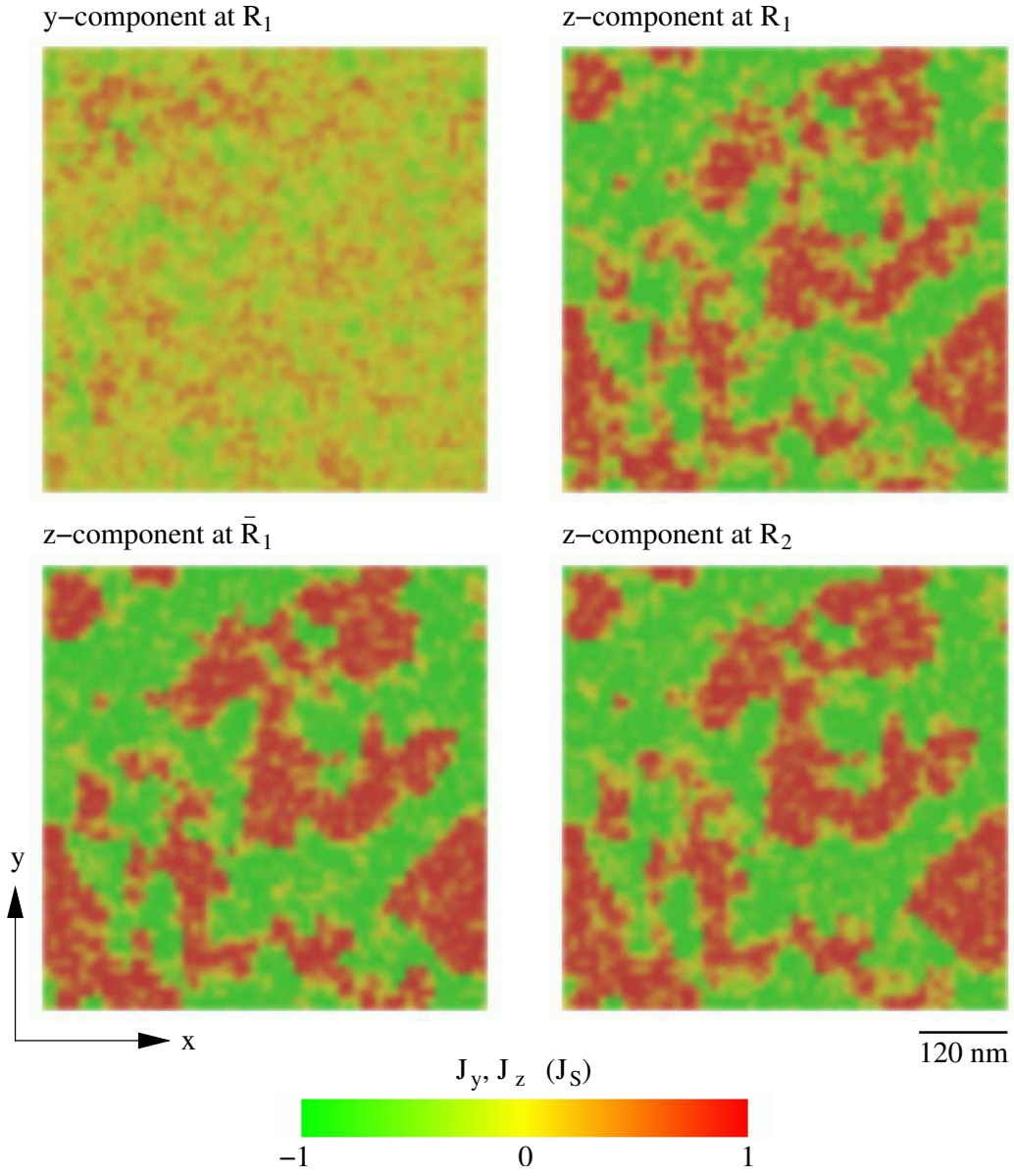


**Figure 4.17:** Antiferromagnetic spin configurations parallel to the y- and z-axis, respectively. Almost no domains are formed along the y-direction because of spin flop coupling to the ferromagnet. The domains parallel to the z-axis are almost unaffected by the rotation of the ferromagnet.



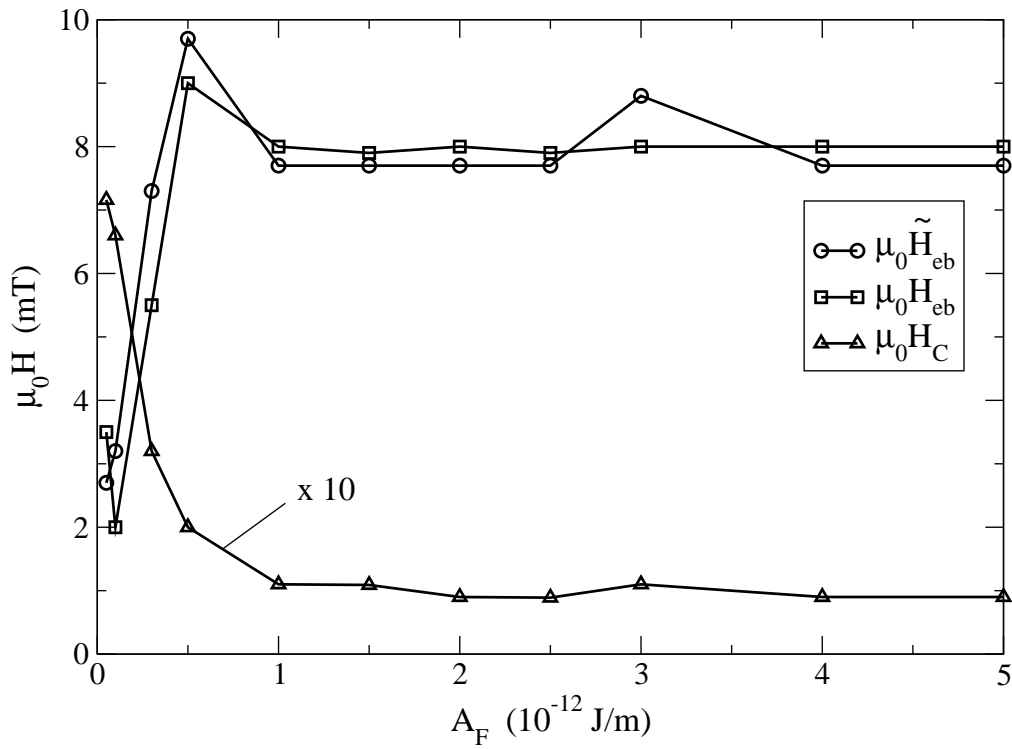


**Figure 4.18:**  $H_{eb}$ ,  $\tilde{H}_{eb}$  and  $H_C$  as a function of  $A_F$ . The exchange bias field quickly increases with increasing exchange coupling and remains nearly constant ( $\approx 8$  mT) for  $A_F \gtrsim 1 \cdot 10^{-12}$  J/m. To find the correct value of  $H_C$ , the given function has to be multiplied by 10.  $H_C$  shows the inverse behavior of  $H_{eb}$ . For  $A_F \gtrsim 1 \cdot 10^{-12}$  we found  $\mu_0 H_C \approx 10$  mT.

## 4.3 Variation of Parameters

### 4.3.1 Exchange Constant of the Ferromagnet

The dependence of the bias field and the coercivity on the exchange constant  $A_F$  of the ferromagnet is shown in Fig. 4.18. The shift of the hysteresis loop is small for  $A_F \lesssim 0.3 \cdot 10^{-12}$  J/m and almost independent of the coupling strength for  $A_F \gtrsim 1 \cdot 10^{-12}$  J/m within a wide range ( $\mu_0 H_{eb} \approx 8$  mT). That is to say, a considerably high exchange bias field requires an ferromagnetic exchange constant  $A_F$  greater than a certain threshold value.

The behavior of the exchange bias field has its roots in the percentage  $s$  and the pattern of switched grains (see Sec. 4.1.2) since a change of  $A_F$  leaves the antiferromagnetic energy terms unaffected. For  $A_F = 0.1 \cdot 10^{-12}$  J/m only 12.3 % of the antiferromagnetic grains made an irreversible transition, leading to the ratio  $C/C_{\max} = 16.8$  %, whereas the constant values of  $s \approx 21$  % and  $C/C_{\max} \approx 25$  % were obtained for  $A_F \geq 0.5 \cdot 10^{-12}$  J/m. For low intergrain coupling ripple structure dominates in the remanent state, as depicted in Fig. 4.19 (left hand side), i.e. the antiferromagnet determines the switching behavior

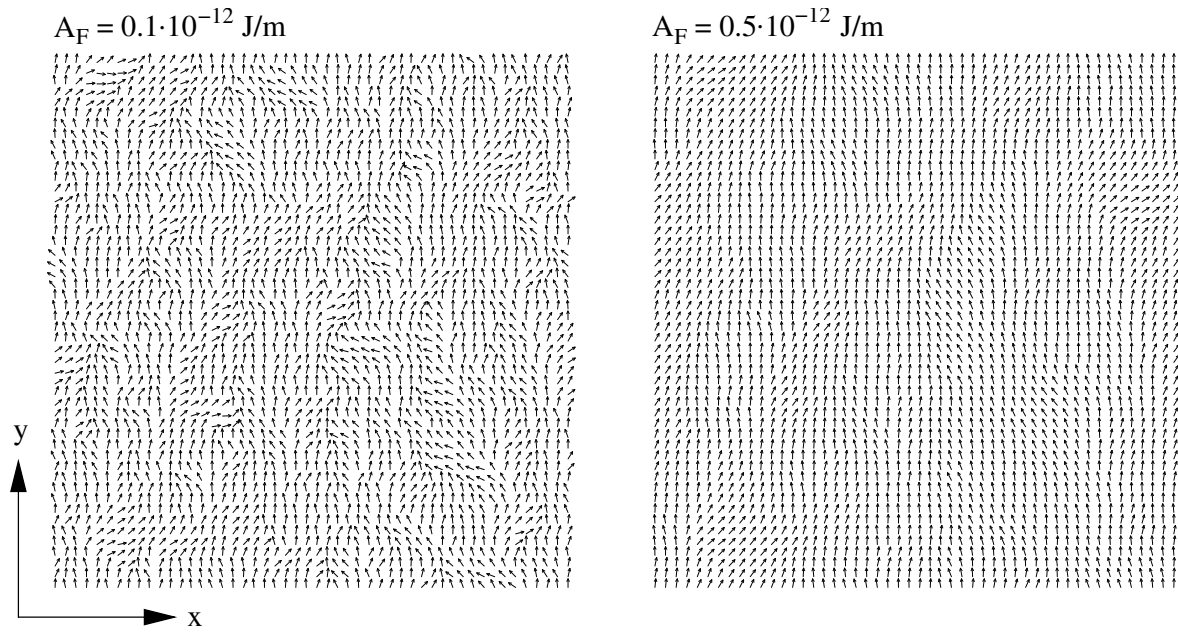


**Figure 4.19:** Domain structure of the ferromagnet in the remanent state  $R_1$  for  $A_F = 0.1 \cdot 10^{-12} \text{ J/m}$  (left hand side) and for  $A_F = 0.5 \cdot 10^{-12} \text{ J/m}$  (right hand side). For low intergrain coupling ripple structure dominates, whereas domains are formed when  $A_F$  increases. The spatial “wavelength” of the ripple structure mainly depends on the exchange coupling of the ferromagnet.

when the external field reverses the ferromagnet. Thus, the ferromagnet is able to switch only a few antiferromagnetic grains. In fact, for micropolycrystalline films of the kind of interest here, experiments showed that the magnetization in a domain is not completely uniform but exhibits a ripple structure [14]. This is the reason for a small quasi-periodic variation of the intensity perpendicular to the mean magnetization direction found in Fresnel images. With increasing  $A_F$  the ferromagnetic spins form domains (see Fig. 4.19 on the right hand side). Whether an antiferromagnetic grain switches or not depends on the chosen parameters, the adjacent grains and, first of all, on the direction of the easy axis. For  $A_F \gtrsim 0.5 \cdot 10^{-12} \text{ J/m}$  the ferromagnet switches all possible antiferromagnetic grains. An increase of  $A_F$  has no further effect on  $s$  or  $C/C_{\max}$ .

The coercive field falls off rapidly with increasing ferromagnetic exchange coupling and is also nearly constant for  $A_F \gtrsim 1 \cdot 10^{-12} \text{ J/m}$ . For  $A_F = 0.1 \cdot 10^{-12} \text{ J/m}$  we found  $\mu_0 H_C = 66 \text{ mT}$ , whereas for  $A_F = 1 \cdot 10^{-12} \text{ J/m}$  the coercivity is only  $\mu_0 H_C = 11 \text{ mT}$ . The increase of the coercive field with decreasing  $A_F$  was also reported by Stiles and McMichael [32].

To understand the dependence of  $H_C$  of the bilayer system on  $A_F$ , first consider a single polycrystalline ferromagnetic layer with randomly distributed easy axes [33]. If the mag-

netization is constrained to be uniform over the whole sample owing to a high rotating external field (rotational hysteresis measurement), the energy of the system is the same for any orientation of the magnetization vector. The coercivity vanishes since no irreversible processes occur in the ferromagnet (the rotational hysteresis loss is zero if the field is higher than the anisotropy field). The same result would be obtained for an infinitely large exchange constant. Apparently, irreversible processes appear more frequently when the exchange constant decreases.

For ferro-/antiferromagnetic bilayer systems the rotational hysteresis measurement does not vanish even for arbitrarily large fields. That is, in these systems irreversible work is being done during reversal of the ferromagnet even if the exchange constant of the ferromagnet is infinitely large. These irreversible processes occur in the antiferromagnet since the interfacial coupling strength is still finite. When the exchange constant of the ferromagnet decreases, the anisotropy, induced via the interfacial coupling, becomes more and more dominant. Therefore,  $H_C$  increases with decreasing  $A_F$  analogously to a single ferromagnetic layer.

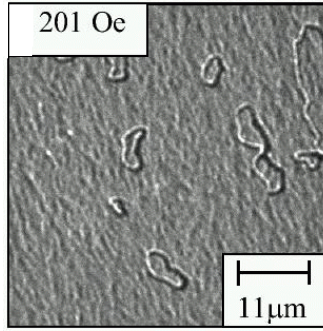


**Figure 4.20:** A Fresnel image of remarkably stable  $360^\circ$  wall loops. From Ref. [14].

Several groups, for instance King et al. [14] and Gogol et al. [8], obtained  **$360^\circ$  domain wall loops**. The Fresnel image Fig. 4.20 from Ref. [14] shows several loops. Such loops, once formed, were remarkably stable and stayed in place up to fields of about 30 mT. Beyond this, the ferromagnetic film appeared saturated. Repetition of the hysteresis cycle resulted a similar behavior, but the locations of these loops tended to vary. Furthermore, they also found less stable lines of  $360^\circ$  domain walls. Note that high stability  $360^\circ$  walls are not found in single ferromagnetic layers without imperfections or impurities.

In our simulations stable  $360^\circ$  wall loops or lines appeared primarily for  $A_F \approx 0.3 \cdot 10^{-12}$  J/m. Fig. 4.21 shows hysteresis curves and Fig. 4.22 an image sequence of the formation and annihilation of an extremely stable  $360^\circ$  loop for this coupling constant. At  $\mu_0 H \approx 30$  mT domain walls move together and, rather than annihilating, form a  $360^\circ$  wall loop. This configuration is stable due to the pinning effect of the antiferromagnetic

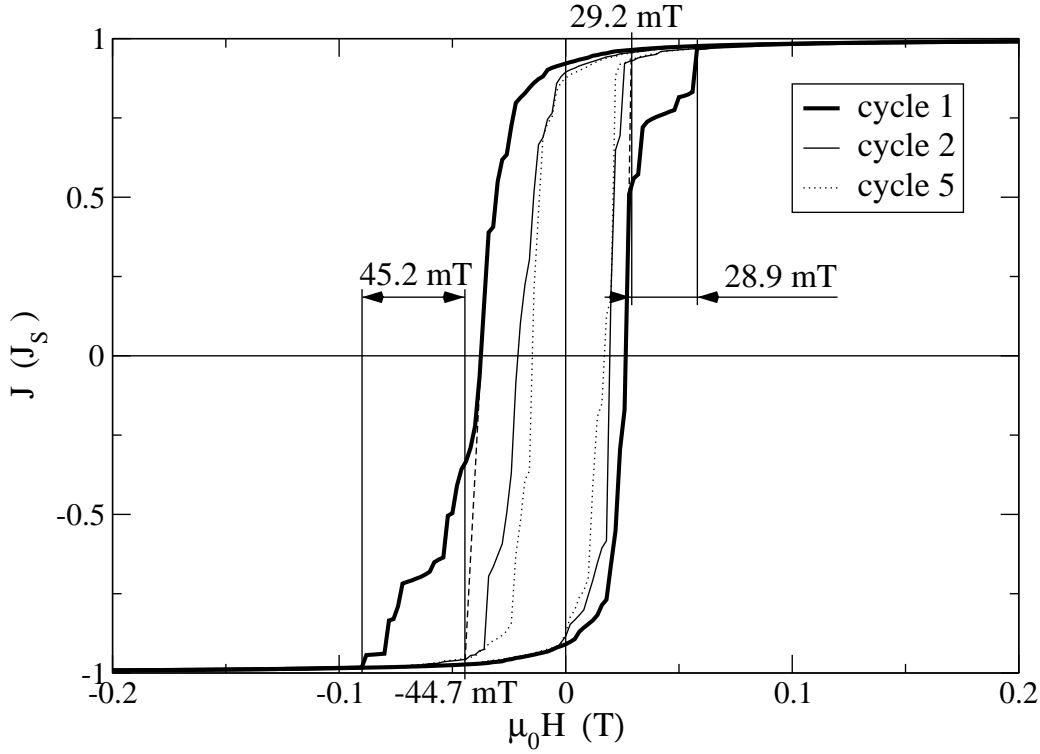


**Figure 4.21:** Hysteresis loops for  $A_F = 0.3 \cdot 10^{-12}$  J/m. Cycle 1 shows distinct knees for decreasing as well as for increasing external field due to the formation of  $360^\circ$  wall loops, leading to an enhancement of the required external field of about 100 % to saturate the pinned layer. The locations of the walls varied for increasing and decreasing fields. The dashed lines approximate the hysteresis curve without  $360^\circ$  walls. The most stable configurations usually appeared for the first hysteresis cycle.

layer, leading to a distinct knee in the hysteresis curve. A similar loop in the ferromagnet and an appropriate knee also occurred for increasing external field. The dashed lines in Fig. 4.21 represent the approximated hysteresis curve of cycle 1 without the appearance of exceedingly stable configurations. That is, the  $360^\circ$  loops enhance the external field required to saturate the ferromagnet by about 100 %. Moreover, this is the reason for the large difference between  $\mu_0 H_{\text{eb}} = 5.5$  mT and  $\mu_0 \tilde{H}_{\text{eb}} = 7.3$  mT in Fig. 4.18.

For exchange constants  $A_F > 0.3 \cdot 10^{-12}$  J/m the formation of such walls becomes more and more energy expensive, whereas for low coupling constants ripple structure hinders the creation of correlated regions. Additionally,  $360^\circ$  walls appear relatively independent of the antiferromagnetic exchange coupling, but need a minimum amount of antiferromagnetic anisotropy energy. For too low anisotropy constants the antiferromagnetic pinning effect is not sufficient to make  $360^\circ$  walls energetically favorable.

Most important, no impurities or structural defects are needed to originate  $360^\circ$  domain walls in ferro-/antiferromagnet bilayer systems, contrary to single ferromagnetic films.

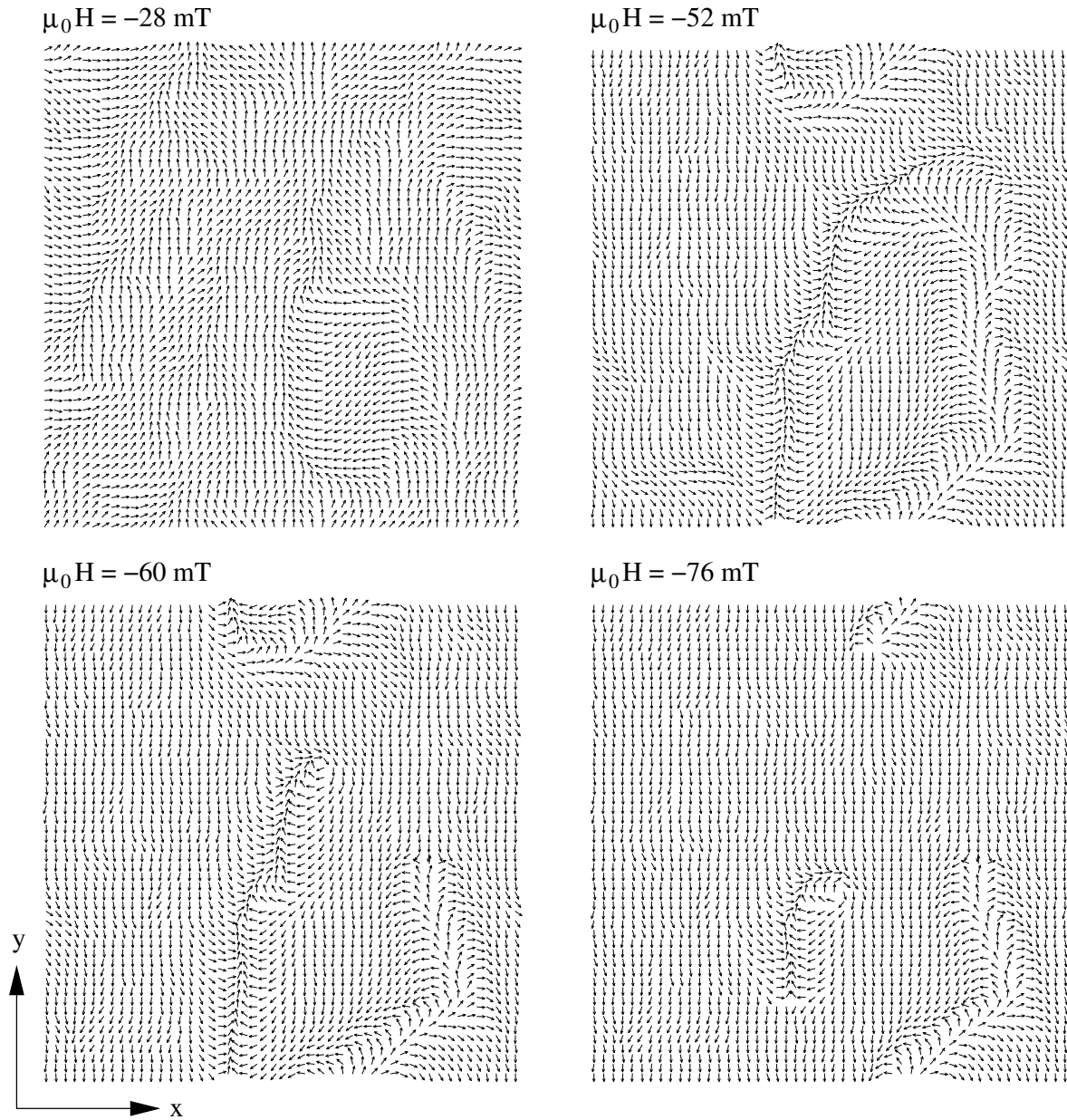


**Figure 4.22:** An image sequence of the creation and finally annihilation of an substantially stable 360° loop for a decreasing external field. At  $\mu_0 H \approx 30$  mT domain walls move together and, owing to the pinning effect of the antiferromagnet, form a stable 360° wall. Parts of the loop remain up to an external field of about 90 mT (see also Fig. 4.21).

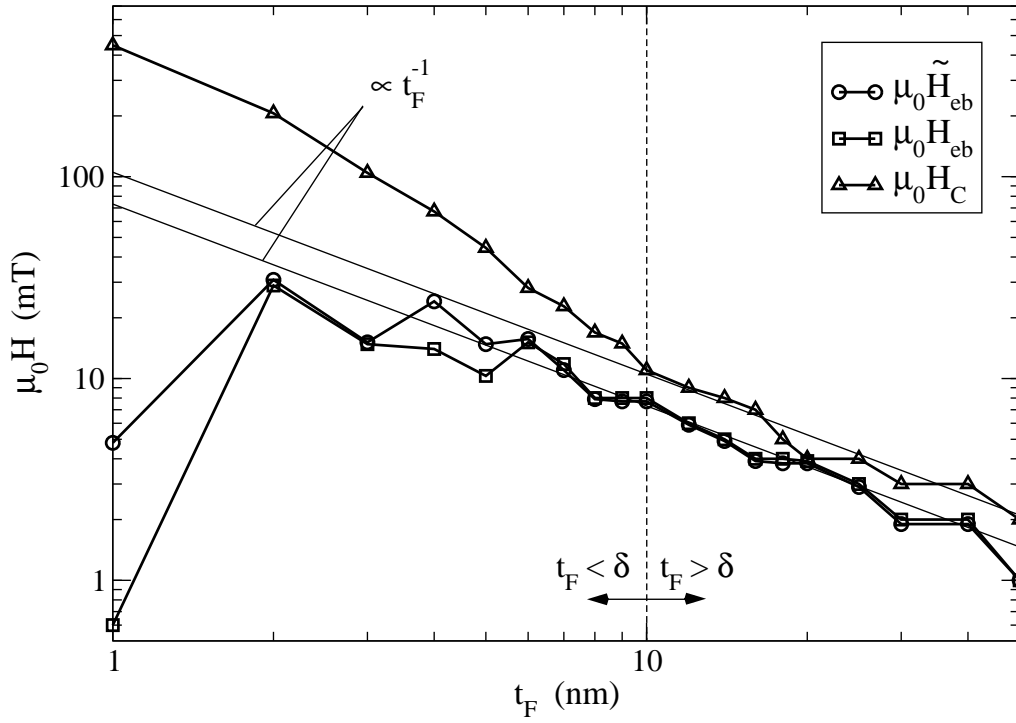


**Figure 4.23:** Dependence of  $H_{\text{eb}}$ ,  $\tilde{H}_{\text{eb}}$  and  $H_C$  on the ferromagnetic thickness, directly calculated by varying  $t_F$ . For  $t_F > \delta$  the characteristic fields behave like  $t_F^{-1}$ , whereas large deviations were found for thicknesses smaller than the ferromagnetic domain wall width. Only the results for  $t_F > 10$  nm were used for the nonlinear curve fits (thin lines).

### 4.3.2 Thickness of the Ferromagnet

The simplest way to vary the intergranular exchange coupling experimentally is to vary the thickness of the ferromagnetic layer, since the exchange energy of the ferromagnet is proportional to  $t_F$  and  $A_F$ . However, the Zeeman term in Eq. (3.1) also depends linearly on the ferromagnetic thickness. In the following we will show that the dependence of the bias field and the coercivity on  $A_F$  determines and explains the behavior of  $H_{\text{eb}}$  and  $H_C$  as a function of the ferromagnetic thickness  $t_F$ . Furthermore, we compare the results obtained by directly varying  $t_F$  with those derived from the results of the last section.

The ferromagnetic exchange energy and the Zeeman energy are dominated by the terms (see Eq. (3.1) and Eq. (3.5))

$$\varepsilon_{ex,F} = A_F t_F \frac{l}{a} = \left( A_F \frac{t_F}{t_{F,0}} \right) t_{F,0} \frac{l}{a} \quad , \quad (4.5)$$

$$\varepsilon_H = J_S l^2 t_F H = J_S l^2 t_{F,0} \underbrace{\left( \frac{t_F}{t_{F,0}} H \right)}_{\mathcal{H}} \quad (4.6)$$

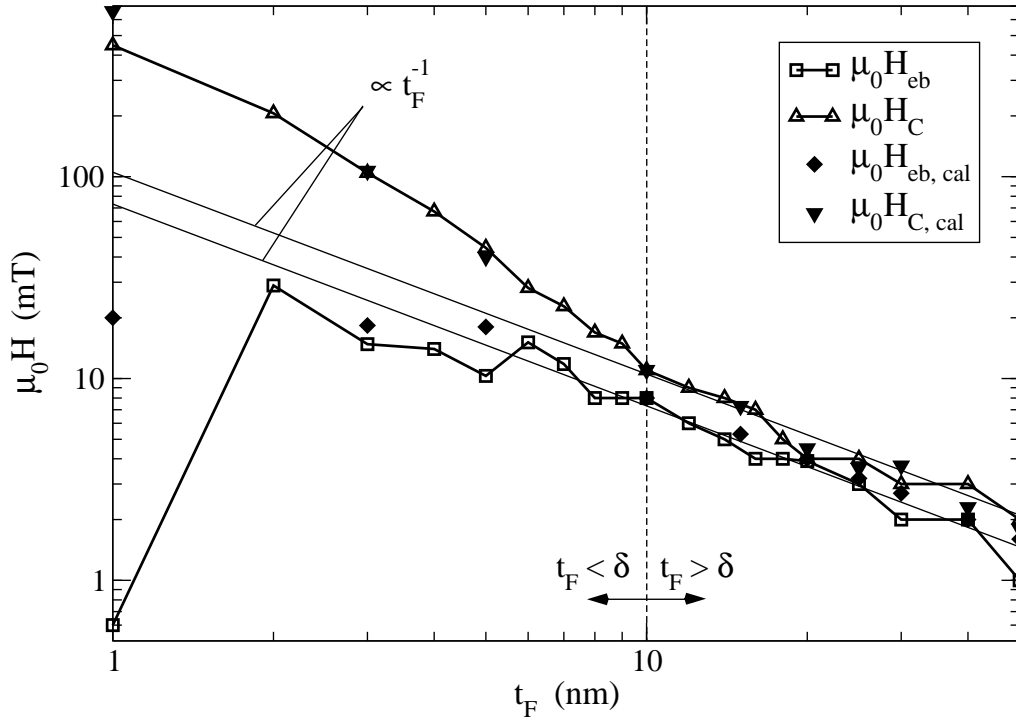


**Figure 4.24:** Comparison of  $H_{\text{eb}}$  and  $H_C$  from Fig. 4.23 with the calculated fields  $H_{\text{eb,cal}}$  and  $H_{C,\text{cal}}$ , obtained via Eq. (4.8) and Eq. (4.9), respectively. The deviations are small, except for  $t_F = 1$  nm.

with the standard parameter  $t_{F,0} = 10$  nm and the rescaled external field  $\mathcal{H}$ . Any other value of  $t_{F,0}$  works as well, of course. Thus, a variation of the ferromagnetic thickness is equivalent to the same variation of  $A_F$  plus a scaling of the external field according to

$$\mu_0 H = \frac{t_{F,0}}{t_F} \mu_0 \mathcal{H} \quad . \quad (4.7)$$

Using the standard parameter  $A_{F,0} = 1 \cdot 10^{-12}$  J/m one finds the relations

$$\mu_0 H_{\text{eb}}(A_{F,0}, t_F) = \frac{t_{F,0}}{t_F} \mu_0 \mathcal{H}_{\text{eb}} \left( A_F = \frac{t_F}{t_{F,0}} A_{F,0}, t_{F,0} \right) \quad (4.8)$$

$$\mu_0 H_C(A_{F,0}, t_F) = \frac{t_{F,0}}{t_F} \mu_0 \mathcal{H}_C \left( A_F = \frac{t_F}{t_{F,0}} A_{F,0}, t_{F,0} \right) \quad . \quad (4.9)$$

It has been observed experimentally that the hysteresis shift is roughly inversely proportional to the ferromagnetic thickness  $t_F$ , indicating that exchange bias is an interface effect [27]. This behavior holds for rather thick ferromagnetic layers (depending on the material parameters) and is no longer valid when  $t_F$  is smaller than the ferromagnetic domain wall size  $\delta$  (usually a few nm).

Since  $H_{\text{eb}}$  and  $H_{\text{C}}$  are almost independent of the ferromagnetic exchange coupling for  $A_{\text{F}} \gtrsim 1 \cdot 10^{-12}$  J/m (see Fig. 4.18), we obtain

$$\left. \begin{aligned} \mu_0 H_{\text{eb}} &\propto t_{\text{F}}^{-1} \\ \mu_0 H_{\text{C}} &\propto t_{\text{F}}^{-1} \end{aligned} \right\} \quad \text{for } t_{\text{F}} \gtrsim 10 \text{ nm} \quad . \quad (4.10)$$

That is, the asymptotic domain wall width

$$\delta = \pi \sqrt{\frac{A_{\text{F}}}{K_{\text{ind}}}} \quad (4.11)$$

of the ferromagnet is approximately 10 nm (for the standard parameters).  $K_{\text{ind}}$  estimates the anisotropy constant, induced by the antiferromagnet. Using  $A_{\text{F}} = 1 \cdot 10^{-12}$  J/m, we find  $K_{\text{ind}} \approx 10^5$  J/m<sup>3</sup>. That is to say, the coupling to the antiferromagnet causes a ferromagnetic anisotropy constant of the same order of magnitude as the anisotropy constant of the antiferromagnet.

Fig. 4.23 shows the results for  $H_{\text{eb}}$  and  $H_{\text{C}}$ , found by directly varying the ferromagnetic thickness  $t_{\text{F}}$ . For  $t_{\text{F}} > \delta$  the exchange bias field and coercivity are, except for small deviations due to finite size effects, strongly proportional to  $t_{\text{F}}^{-1}$  as predicted above. Below the ferromagnetic domain wall width,  $H_{\text{C}}$  increases more rapidly with decreasing  $t_{\text{F}}$ , whereas  $H_{\text{eb}}$  increases more slowly. These deviations are in agreement with experimental results and have their origin in the behavior of the characteristic fields with varying  $A_{\text{F}}$  (see Fig. 4.18).

It is worth noting that we found a considerably high *positive shift* of the hysteresis curve of  $\mu_0 H_{\text{eb}} = \overline{13.5}$  mT for  $t_{\text{F}} = 1$  nm and  $50 \times 50$  grains. However, a new simulation with  $80 \times 80$  grains resulted in the (negative) bias field of Fig. 4.23.

The exchange bias field  $H_{\text{eb,cal}}$  and coercivity  $H_{\text{C,cal}}$  calculated with Eq. (4.8) and Eq. (4.9) are shown in Fig. 4.24. The results are in good agreement with those obtained by varying  $t_{\text{F}}$  except for  $t_{\text{F}} = 1$  nm, where a considerably high deviation occurred.

For the standard parameters stable 360° walls appeared for  $A_{\text{F}} \approx 0.3 \cdot 10^{-12}$  J/m. The correlation between a variation of  $t_{\text{F}}$  and  $A_{\text{F}}$  suggests that 360° loops should also appear for  $t_{\text{F}} \approx 3$  nm, accompanied with marked knees in the hysteresis curves. In fact, simulations for  $t_{\text{F}} = 3$  nm and  $t_{\text{F}} = 4$  nm resulted in extremely stable loops. The sequence of images in Fig. 4.25 presents the results for  $t_{\text{F}} = 4$  nm at different external fields. A relatively high external field of  $\mu_0 H \approx -200$  mT had to be applied to remove the last part of the stable configuration.



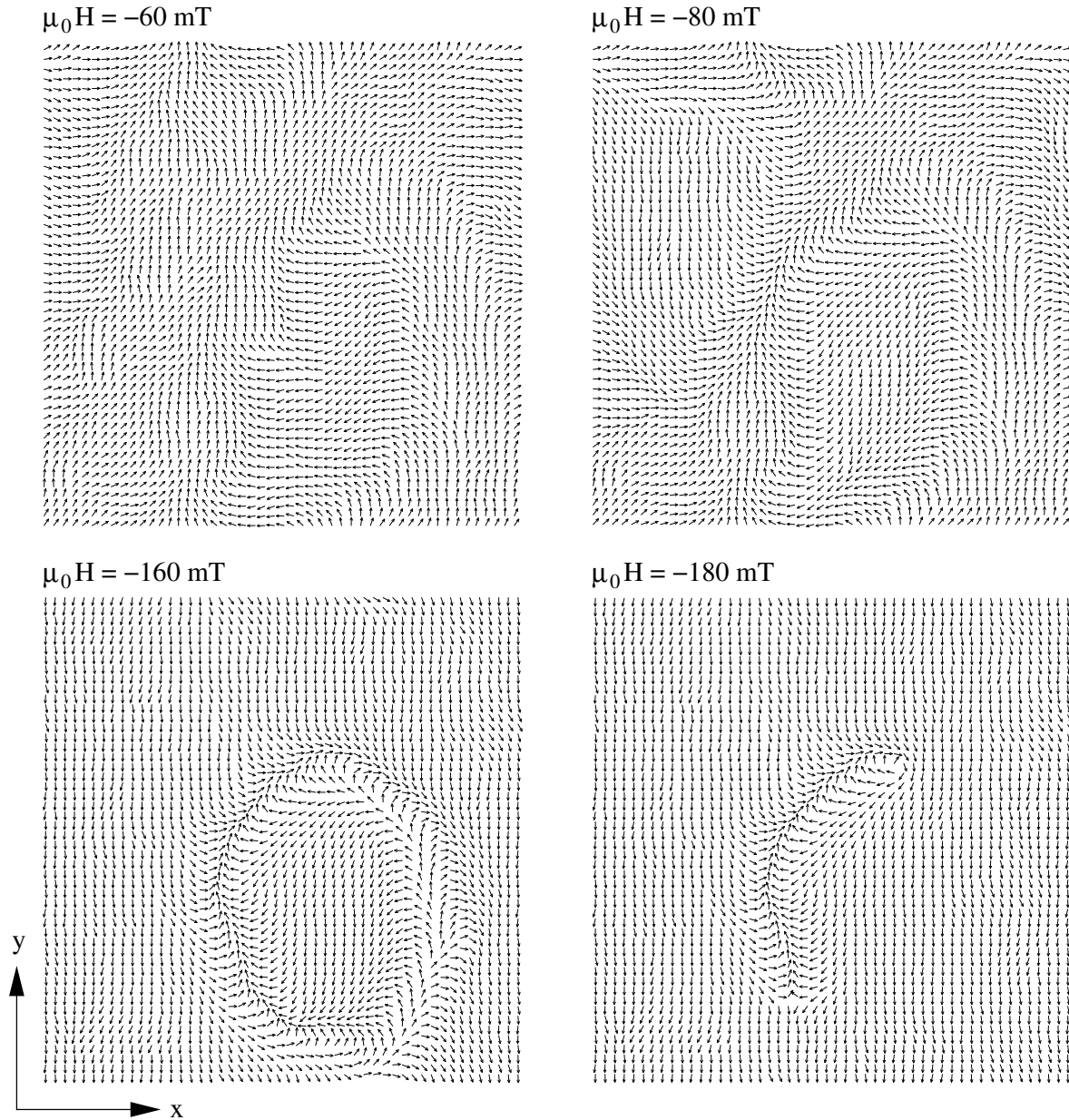


**Figure 4.25:** An extremely stable  $360^\circ$  loop appearing for  $t_F = 4 \text{ nm}$ . It starts to form at about  $-60 \text{ mT}$  and remains up to  $-170 \text{ mT}$ . A high external field of about  $-200 \text{ mT}$  was required to annihilate the last part of the loop.

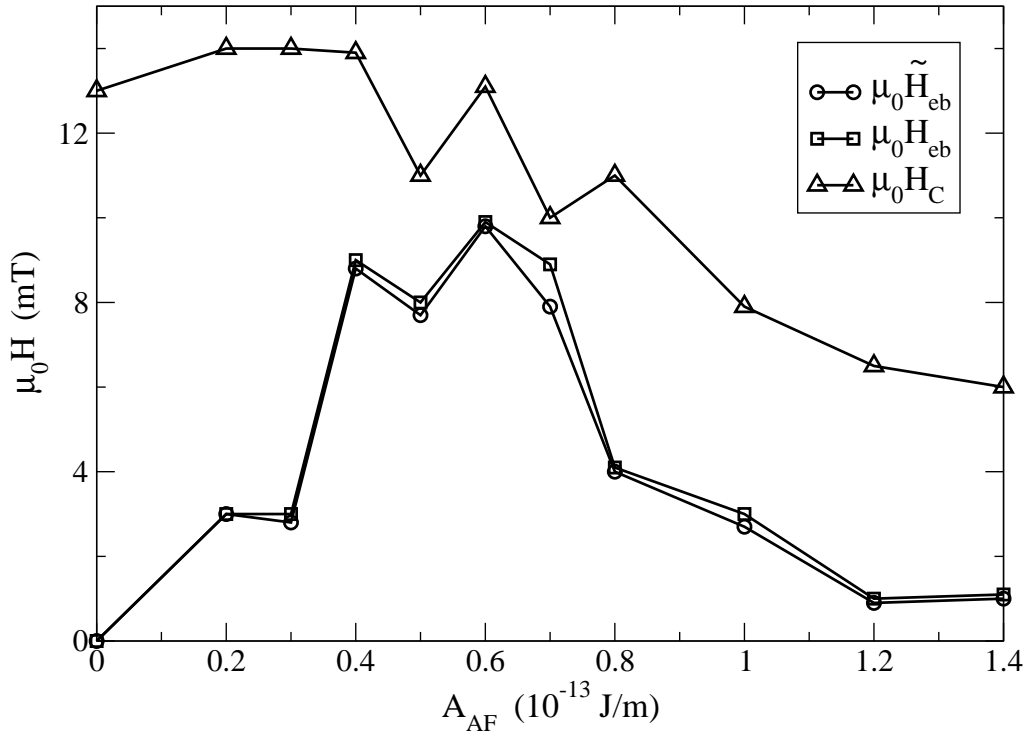


**Figure 4.26:** Bias field and coercivity as a function of the antiferromagnetic exchange coupling  $A_{AF}$ . The bias field exhibits a relatively narrow maximum between  $0.4 \cdot 10^{-13}$  and  $0.7 \cdot 10^{-13}$  J/m.  $H_C$  decreases continuously with increasing exchange constant, reflecting that coherent rotation of the strongly coupled grains becomes more and more favorable.

### 4.3.3 Exchange Constant of the Antiferromagnet

The results of our simulations for varying  $A_{AF}$  are depicted in Fig. 4.26. The bias field shows a pronounced maximum between  $A_{AF} = 0.4 \cdot 10^{-13}$  and  $A_{AF} = 0.7 \cdot 10^{-13}$  J/m and quickly falls off for larger antiferromagnetic exchange constants. Fig. 4.27 makes clear that the increase of  $H_{eb}$  is a result of the rising ratio  $C/C_{\max}$ .

For low intergrain coupling the antiferromagnetic grains switch individually rather than in clusters. For decoupled antiferromagnetic spins only grains with an easy axis nearly parallel to the interface may be dragged by the ferromagnet. Of course no hysteresis shift or training effect occurs for independent grains. As  $A_{AF}$  increases the switching behavior becomes more and more a collective phenomenon. Finally for  $A_{AF} \gtrsim 0.7 \cdot 10^{-13}$  J/m  $C/C_{\max}$  shows no further increase although  $s$  increases as well. In this region a larger intergrain coupling leads to smaller angles between switched and not switched grains and therefore to a lower energy difference stored in the antiferromagnetic domain walls, that is a lower bias field.

In our calculations  $H_{eb}$  changed its sign for  $A_{AF} \gtrsim 1.6 \cdot 10^{-13}$  J/m. We found out that

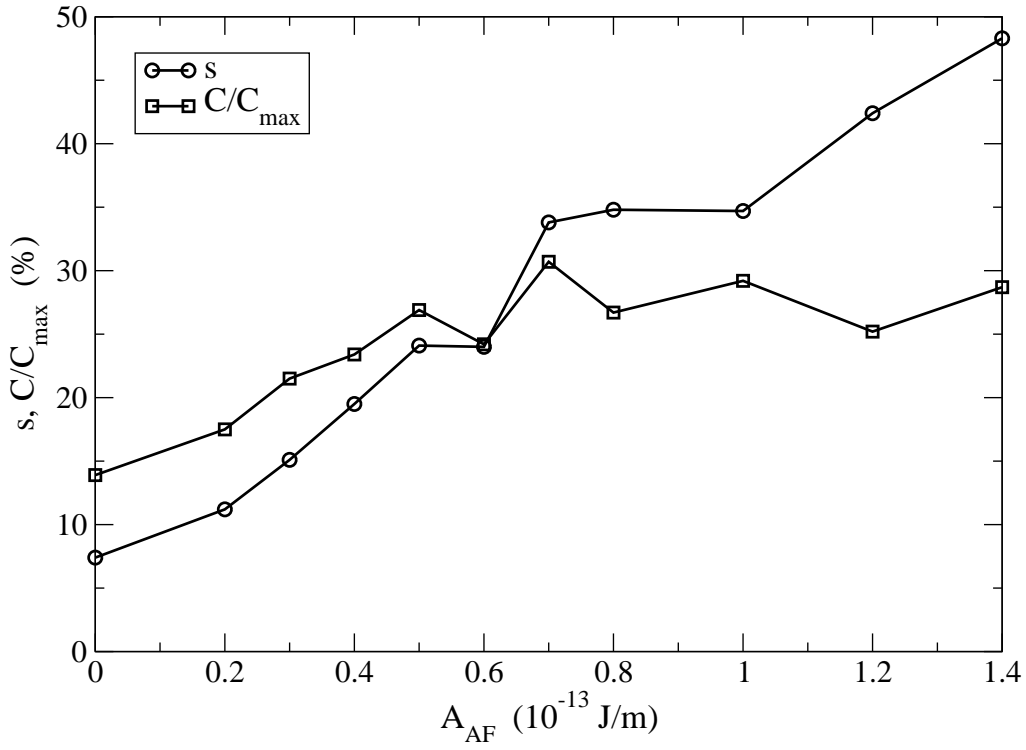


**Figure 4.27:**  $s$  and  $C/C_{\max}$  as a function of  $A_{AF}$ . The higher the intergrain coupling the more grains make an irreversible transition. For  $A_{AF} \gtrsim 0.7 \cdot 10^{-13} \text{ J/m}$  the ratio  $C/C_{\max}$  is almost independent of  $A_{AF}$  in order to minimize the energy stored in antiferromagnetic domain walls.

the initial temperature  $T_i = 800 \text{ K}$  of the field cooling process was too small to enable the bilayer system to reach the energy minimum, resulting in a positive energy difference between the remanent states  $R_1$  and  $\bar{R}_1$ .

The coercive field  $H_C$  as a function of the antiferromagnetic exchange constant drops continuously. Coherent rotation of considerably large regions takes place for high exchange energies, leading to diminishing irreversible work being done in the antiferromagnet.

Fig. 4.28 shows the domain structure of the pinning film in the remanent state  $R_1$  for  $A_{AF} = 0.3 \cdot 10^{-13} \text{ J/m}$  and  $A_{AF} = 1.4 \cdot 10^{-13} \text{ J/m}$ , respectively. As one expects, the antiferromagnet forms larger domains for higher intergrain exchange energies in order to minimize the domain wall energy.

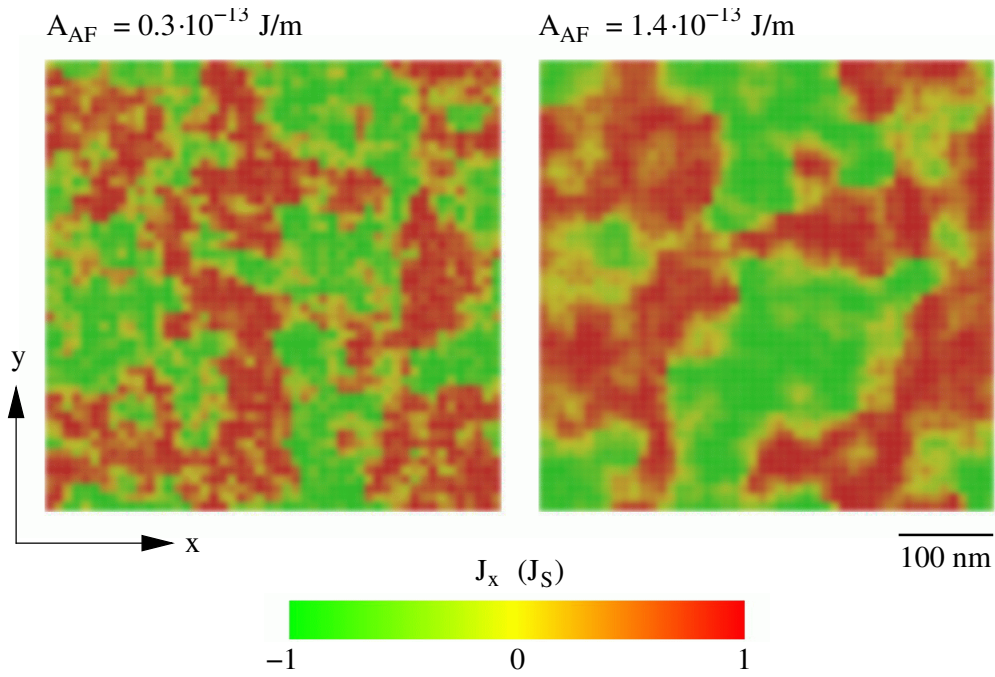


**Figure 4.28:** Magnetization configuration in the antiferromagnet for  $A_{\text{AF}} = 0.3 \cdot 10^{-13} \text{ J/m}$  and  $A_{\text{AF}} = 1.4 \cdot 10^{-13} \text{ J/m}$ , respectively. Obviously, the antiferromagnetic domain size increases for increasing  $A_{\text{AF}}$  in order to minimize the domain wall energy.

#### 4.3.4 Thickness of the Antiferromagnet

The thickness of the antiferromagnetic film has to exceed a certain critical thickness to find exchange bias (*finite size effect* [24]). Beyond it experiments show two different behaviors. First, the exchange bias field increases with increasing  $t_{\text{AF}}$  and decreases after a maximum. Second, for thick pinning layers (e.g.  $t_{\text{AF}} > 20 \text{ nm}$ )  $H_{\text{eb}}$  is independent of  $t_{\text{AF}}$ .

We found that the exchange bias field reaches a maximum of about 9 mT between 20 and 30 nm and decreases with increasing  $t_{\text{AF}}$  for thicker antiferromagnets (see Fig. 4.29). The coercive field increases continuously with increasing thickness and thus reflects the enhancement of the antiferromagnetic pinning effect. For too thin antiferromagnetic films both the exchange bias field and coercivity vanish. The antiferromagnetic layer is no longer magnetic and therefore stops hindering the ferromagnetic rotation.

Larger domains are formed in the antiferromagnet for increasing  $A_{\text{AF}}$  or decreasing  $K_1$ , respectively. One may expect that the antiferromagnetic domains remain almost unaffected if one alters  $t_{\text{AF}}$  because both the exchange energy and the anisotropy energy of the antiferromagnet depend linearly on  $t_{\text{AF}}$ . Therefore, it should be possible to estimate

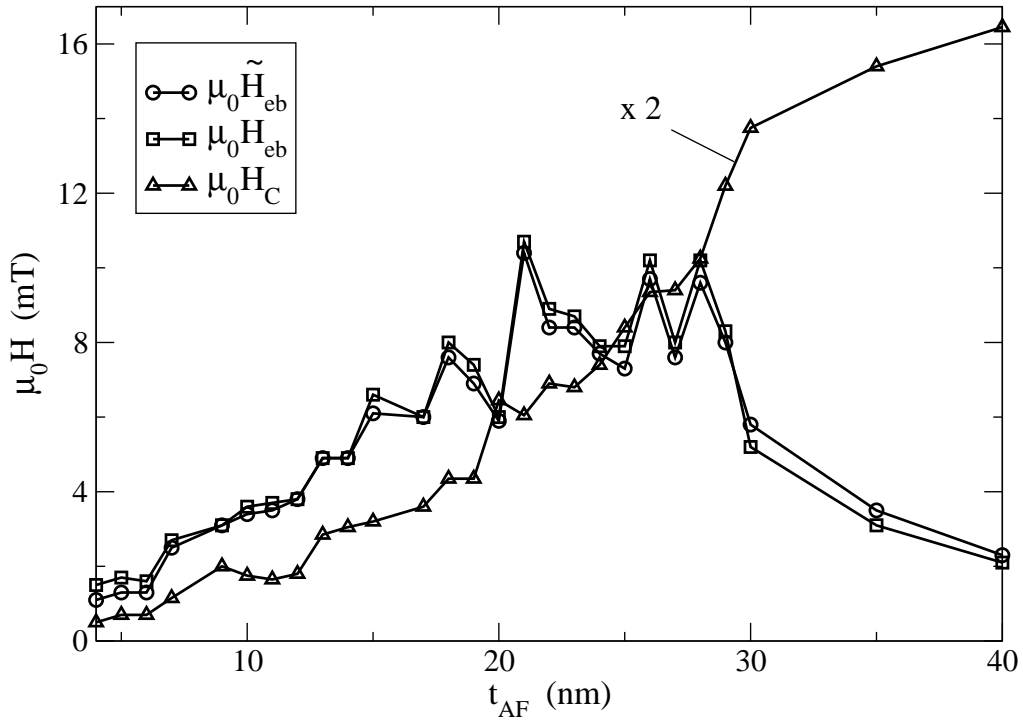


**Figure 4.29:** Dependence of the hysteresis shift and the coercive field on the antiferromagnetic thickness  $t_{AF}$ . The bias field reaches a maximum of about 9 mT between 20 and 30 nm.  $H_C$  increases continuously with increasing thickness, indicating the increasing pinning effect of the antiferromagnet. In order to get the values of  $H_C$ , the depicted function has to be multiplied by 2.

the exchange bias field with the help of the following simple picture.

Suppose two antiferromagnetic grains with parallel easy axes as depicted in Fig. 4.30. On the left hand side the configuration with the lowest energy ( $E_{\downarrow\downarrow}$ ) is shown. The right hand side shows an arbitrary situation resulting in a higher energy ( $E_{\downarrow\uparrow}$ ). To simplify the following calculations we assume that the left spin is fixed to the easy axis.

The IG model explains the phenomenon of exchange bias by domain walls formed in the antiferromagnet. For a rough estimation of the energy difference  $\Delta E = E_{\downarrow\uparrow} - E_{\downarrow\downarrow}$  it is thus sufficient to consider only the exchange and anisotropy energies of the antiferromagnet:

$$E = E_{ex, AF} + E_{ani, AF} = -A_{AF} t_{AF} \frac{l}{a} \cos \alpha - K_1 t_{AF} l^2 \cos^2 \alpha \quad . \quad (4.12)$$

In order to find the angles  $\alpha_0$  where  $E$  becomes an extremum we need the first and second derivatives of (4.12)

$$\left. \frac{\partial E}{\partial \alpha} \right|_{\alpha_0} = A_{AF} t_{AF} \frac{l}{a} \sin \alpha_0 + 2K_1 t_{AF} l^2 \sin \alpha \cos \alpha_0 = 0 \quad (4.13)$$

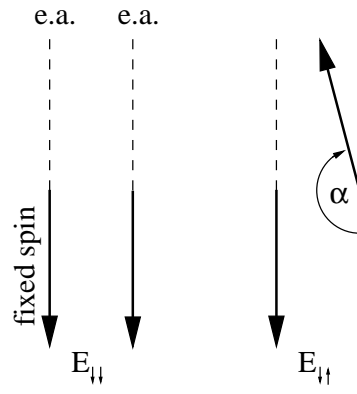


**Figure 4.30:** Two antiferromagnetic grains with parallel easy axes. The configuration with the lowest energy  $E_{\downarrow\downarrow}$  is shown on the left hand side. The right hand side shows a situation with a higher energy  $E_{\downarrow\uparrow}$ . One spin is assumed to be fixed to the easy axis.

$$\left. \frac{\partial^2 E}{\partial \alpha^2} \right|_{\alpha_0} = A_{\text{AF}} t_{\text{AF}} \frac{l}{a} \cos \alpha_0 + 2K_1 t_{\text{AF}} l^2 \cos^2 \alpha_0 - 2K_1 t_{\text{AF}} l^2 \sin^2 \alpha_0 \quad , \quad (4.14)$$

with two possible solutions of Eq. (4.13).

**Case 1:**  $\sin \alpha_0 = 0 \leftrightarrow \alpha_0 = 0, \pi$

Using Eq. (4.14) we get

$$\alpha_0 = 0 \quad \dots \quad \text{minimum} \quad , \quad (4.15)$$

$$\alpha_0 = \pi \quad \dots \quad \begin{cases} \text{maximum for} & A_{\text{AF}}/2K_1 al > 1 \\ \text{saddle point for} & A_{\text{AF}}/2K_1 al = 1 \\ \text{minimum for} & A_{\text{AF}}/2K_1 al < 1 \end{cases} \quad . \quad (4.16)$$

**Case 2:**  $\sin \alpha_0 \neq 0$

One obtains

$$\cos \alpha_0 = -\frac{A_{\text{AF}}}{2K_1 al} \quad \dots \quad \begin{cases} \text{maximum for} & A_{\text{AF}}/2K_1 al < 1 \\ \text{saddle point for} & A_{\text{AF}}/2K_1 al = 1 \end{cases} \quad , \quad (4.17)$$

Since the condition

$$\frac{A_{\text{AF}}}{2K_1 al} \leq 1 \quad (4.18)$$

has to be fulfilled for case 2 there is no energy minimum between 0 and  $\pi$ .

For the standard parameters we find  $A_{\text{AF}}/2K_1 al \approx 1/15 \ll 1$ , that is the second spin makes a transition from the global energy minimum  $\alpha_0 = 0$  to the local minimum  $\alpha_0 = \pi$ .

The energy difference becomes

$$\Delta E = E_{\downarrow\uparrow} - E_{\downarrow\downarrow} = 2A_{\text{AF}}t_{\text{AF}} \frac{l}{a} \quad . \quad (4.19)$$

In most cases the bias field should be proportional to the energy difference between the remanent states  $R_1$  and  $\bar{R}_1$  ( $H_{\text{eb}} \propto \Delta E$ ). In consideration of the circumference ratio  $C/C_{\text{max}}$  (see Fig. 4.31) we try

$$H_{\text{eb}} \propto \frac{C}{C_{\text{max}}} t_{\text{AF}} \quad (4.20)$$

for the exchange bias field. Of course adjacent spins are not fully parallel or antiparallel. But the situation should not depend on  $t_{\text{AF}}$ , that is a more realistic picture should not destroy the proportionality in Eq. (4.20).

Fig. 4.32 compares the exchange bias field  $\mu_0 H_{\text{eb}}$  of Fig. 4.29 with the field  $\mu_0 H_{\text{eb,cal}}$  according to Eq. (4.20). Both functions agree well, particularly the position of the maxima. Even local spikes of the bias field between 20 and 30 nm are reproduced by Eq. (4.20), although the heights do not agree.

The energy difference  $\Delta E$  in Eq. (4.19) also depends on  $A_{\text{AF}}$  and  $l$ . But contrary to  $t_{\text{AF}}$  a variation of  $A_{\text{AF}}$  or  $l$  entirely alters the properties of the bilayer system. An important assumption of Eq. (4.19) was that the antiferromagnetic domain structure remains almost unaffected by changing the thickness of the antiferromagnet. Therefore, Eq. (4.19) cannot be applied to a variation of  $l$  or  $A_{\text{AF}}$ , respectively.

The IG model assumes homogeneous magnetization configurations within the antiferromagnetic grains. Of course this assumption is not valid beyond some antiferromagnetic thickness, depending on the system parameters. We expect that the results of the IG model are reliable for antiferromagnetic thicknesses up to at least 50 nm.

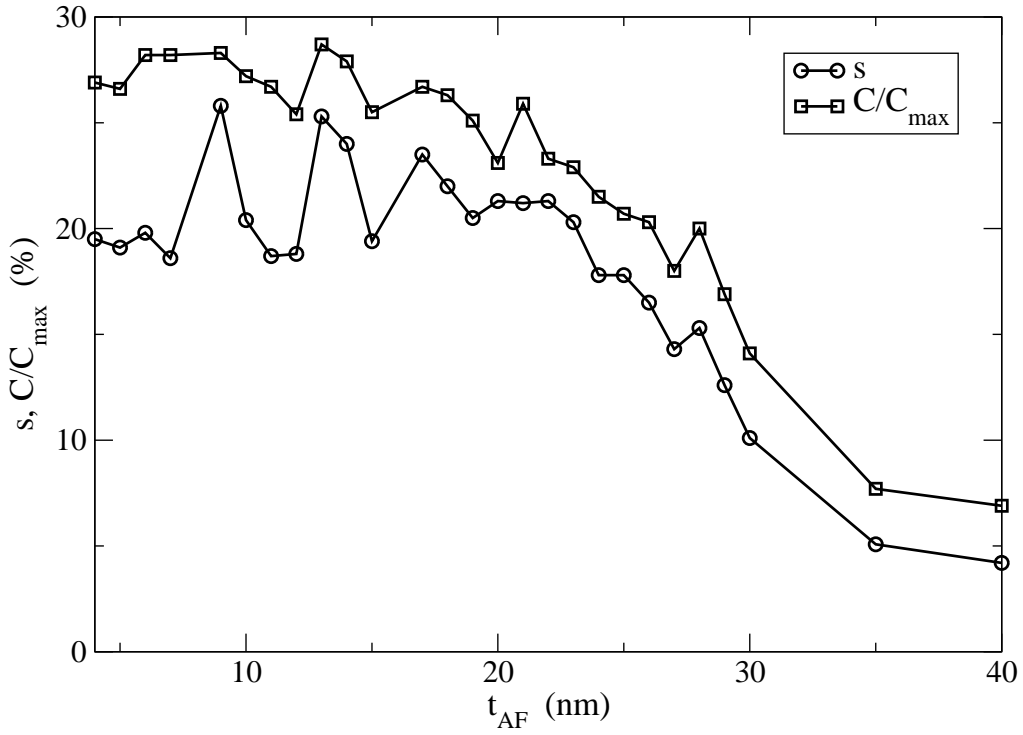


**Figure 4.31:**  $C/C_{max}$  and  $s$  versus the antiferromagnetic film thickness  $t_{AF}$ . Beyond  $t_{AF} \approx 20$  nm  $s$  and  $C/C_{max}$  quickly fall off, resulting in a diminishing bias field.

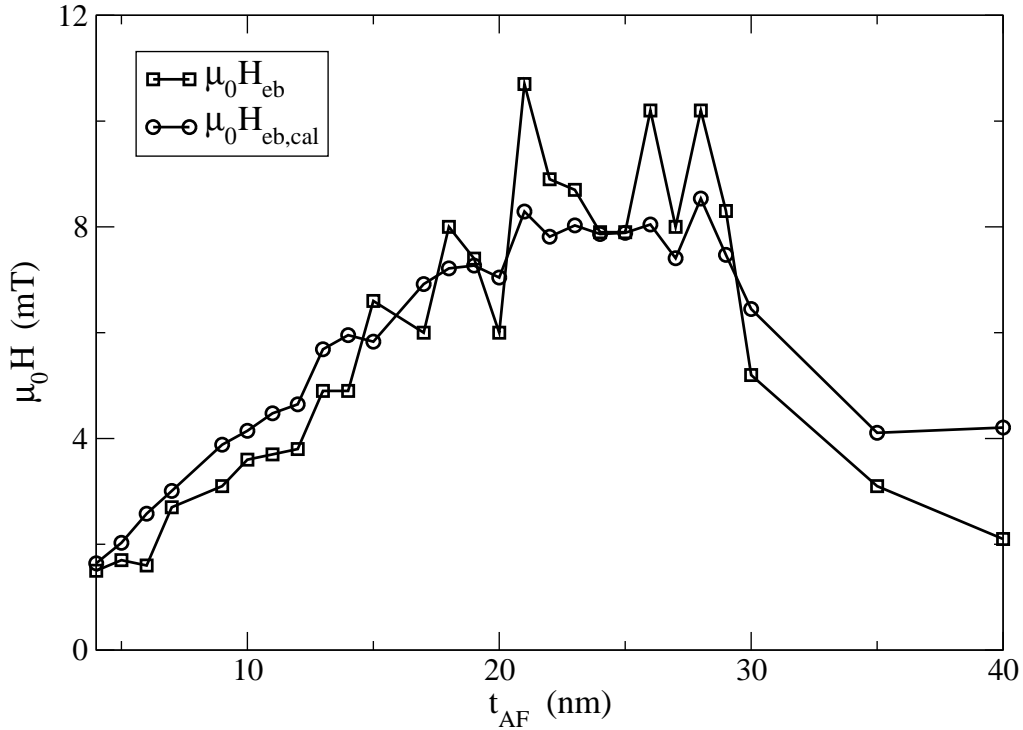


**Figure 4.32:** A comparison of  $\mu_0 H_{eb}$  found by directly varying  $t_{AF}$  with  $\mu_0 H_{eb,cal}$  according to Eq. (4.20). The results agree considerably well, in particular the position of the maxima.



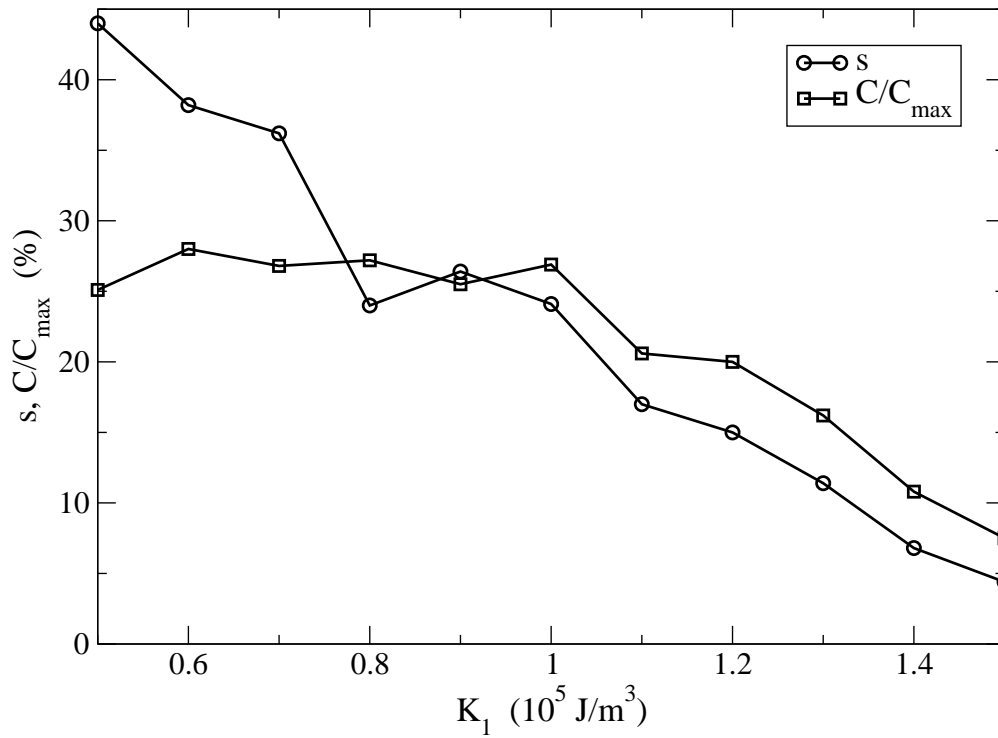


**Figure 4.33:**  $s$  and  $C/C_{\max}$  as a function of the anisotropy constant  $K_1$ . For  $K_1 \gtrsim 10^5$  J/m<sup>3</sup> both functions behave quite similar, whereas  $C/C_{\max}$  remains nearly constant for  $K_1 \lesssim 10^5$  J/m<sup>3</sup>. For decreasing  $K_1$  growing clusters of antiferromagnetic grains switch as the ferromagnet reverses since  $s$  increases with decreasing anisotropy constant.

### 4.3.5 Anisotropy Constant of the Antiferromagnet

The anisotropy constant  $K_1$  mainly affects the switching behavior of the antiferromagnetic grains. Fig. 4.33 shows the percentage  $s$  of switched grains and  $C/C_{\max}$  as function of  $K_1$ . Apparently,  $s$  quickly decreases with increasing  $K_1$  because it becomes more and more difficult to switch antiferromagnetic grains with easy axes not almost parallel to the interface. Beyond  $K_1 \approx 1 \cdot 10^5$  J/m<sup>3</sup> the ratio  $C/C_{\max}$  behaves in a similar way. However, below  $K_1 \approx 1 \cdot 10^5$  J/m<sup>3</sup> the circumference of switched areas is almost constant, indicating that switching of antiferromagnetic clusters becomes important. Additionally, the mean value of the angles between switched and not switched grains and thus the energy difference  $\Delta E$  between  $R_1$  and  $\bar{R}_1$  falls off, resulting in a lower bias field.

Fig. 4.34 summarizes the calculated hysteresis shift and coercive field versus  $K_1$ , verifying the considerations above. With increasing anisotropy constant the increasing energy barrier induced by the antiferromagnet causes the coercivity to rise although  $s$  falls off. Irreversible transitions of antiferromagnetic grains contribute to coercivity. But as  $K_1$  increases irreversible work being done in the pinned layer becomes important and finally dominates. That is, even though  $s$  is rather small coercivity can rise with  $K_1$ .

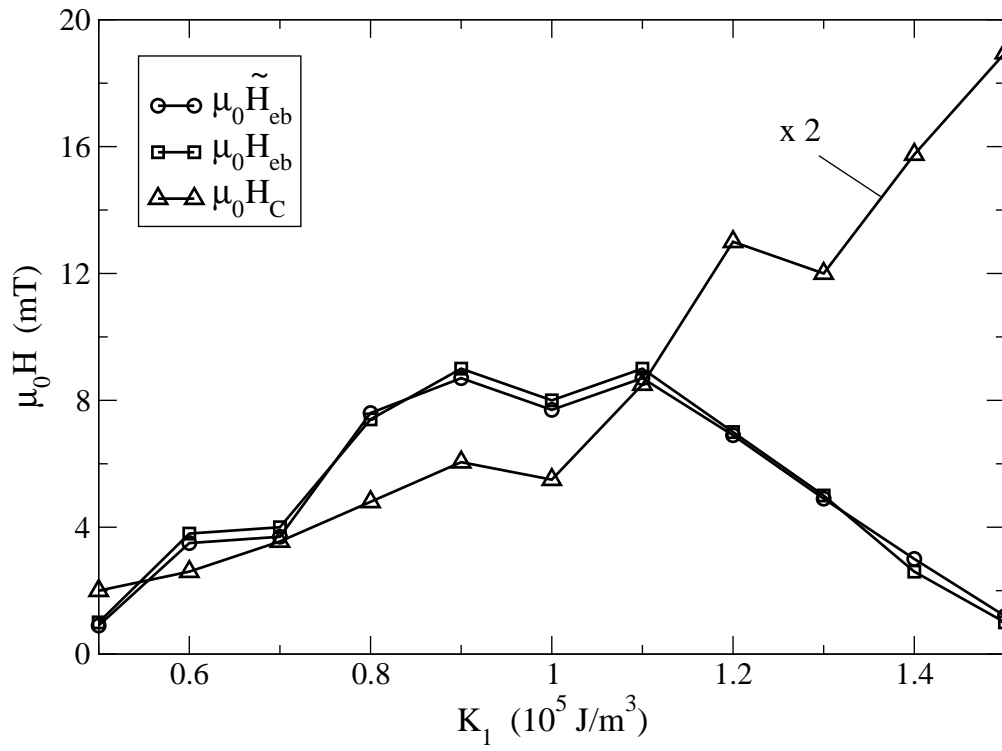


**Figure 4.34:** Bias field and coercivity versus  $K_1$ . The function  $H_C$  has to be multiplied by 2 to obtain the correct coercivity.  $H_C$  increases continuously with increasing  $K_1$  due to irreversible work within the ferromagnet. The bias field reaches a maximum of about 9 mT for  $K_1 \approx 0.9 - 1.1 \cdot 10^5$  J/m<sup>3</sup>.

In several experiments the ferromagnet decouples for large antiferromagnetic anisotropies because it cannot drag antiferromagnetic spins [27]. Consequently the coercive field falls off which is in contrast to our results. However, other systems show an increasing coercive field for increasing antiferromagnetic anisotropy [38]. We expect that  $H_C$  as a function of  $K_1$  behaves different for different exchange constants.

### 4.3.6 Interface Coupling

The dependence of the exchange bias field and coercivity on the interfacial coupling strength  $A_{AF-F}$  is shown in Fig. 4.35. Although the characteristic fields fluctuate for  $|A_{AF-F}| \gtrsim 1 \cdot 10^{-12}$  J/m, their mean values are almost independent of the interfacial coupling strength due to the constant ratio  $C/C_{\max} \approx 29$  %. Moreover,  $A_{AF-F}$  does not act on the relevant energy terms  $E_{ex,AF}$  and  $E_{ani}$ . For  $|A_{AF-F}| \lesssim 1 \cdot 10^{-12}$  the percentage  $C/C_{\max}$  decreases rapidly with decreasing interface coupling constant. For example  $C/C_{\max} = 6.1$  % for  $A_{AF-F} = -0.5 \cdot 10^{-12}$  J/m. Obviously,  $H_{eb}$  and  $H_C$  vanish for  $A_{AF-F} \rightarrow 0$  J/m (coherent rotation of the ferromagnet).

For given parameters of the bilayer system a minimum strength of the spin flop coupling

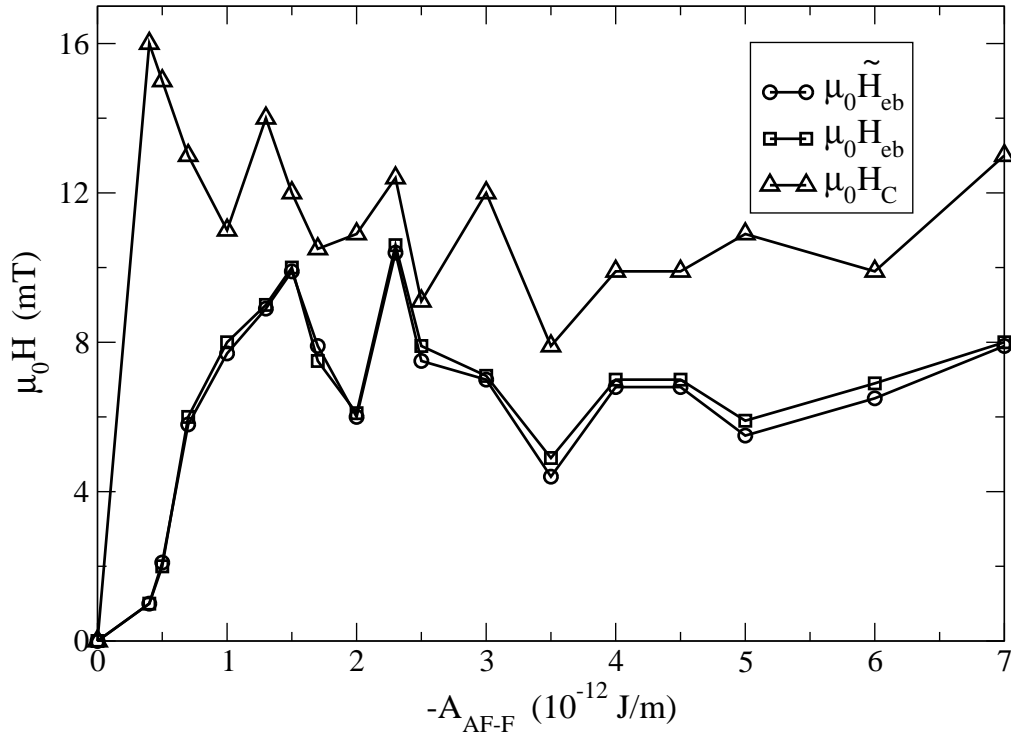


**Figure 4.35:**  $H_{eb}$ ,  $\tilde{H}_{eb}$  and  $H_C$  as function of the negative interfacial coupling constant  $-A_{AF-F}$ . For  $|A_{AF-F}| \gtrsim 1 \cdot 10^{-12} \text{ J/m}$  the characteristic fields fluctuate but the general behavior is almost independent of  $A_{AF}$ .

is required to switch all possible antiferromagnetic grains. A further increase of  $|A_{AF-F}|$  does not result in a higher percentage  $s$  of switched grains. Hence  $H_{eb}$  and  $H_C$  remain nearly constant.

The difference between  $H_{eb}$  and  $\tilde{H}_{eb}$  is negligible because stable configurations cannot be originated by changing the interfacial coupling strength.

### 4.3.7 Grain Size

Experimentally, the role of the grain size in exchange bias remains more or less unclear [27]. Some of the effects of the grain size are expected to be similar to the thickness effects. The results from different studies, however, seem to depend on the specific system and conditions. As the grain size changes, probably other parameters are affected substantially as well. Some systems show an increasing bias field for increasing grain size while other experiments resulted in an inverse behavior.

Fig. 4.36 shows the results of our simulations for  $A_F = 0.5 \cdot 10^{-12} \text{ J/m}$ .  $H_C$  increases continuously while  $H_{eb}$  exhibits a maximum ( $\mu_0 H_{eb} \approx 10 \text{ mT}$ ) between  $l \approx 8 \text{ nm}$  and  $l \approx 13 \text{ nm}$ . King et al. [14] calculated average grain sizes of 7–8 nm for NiFe/IrMn bilayers

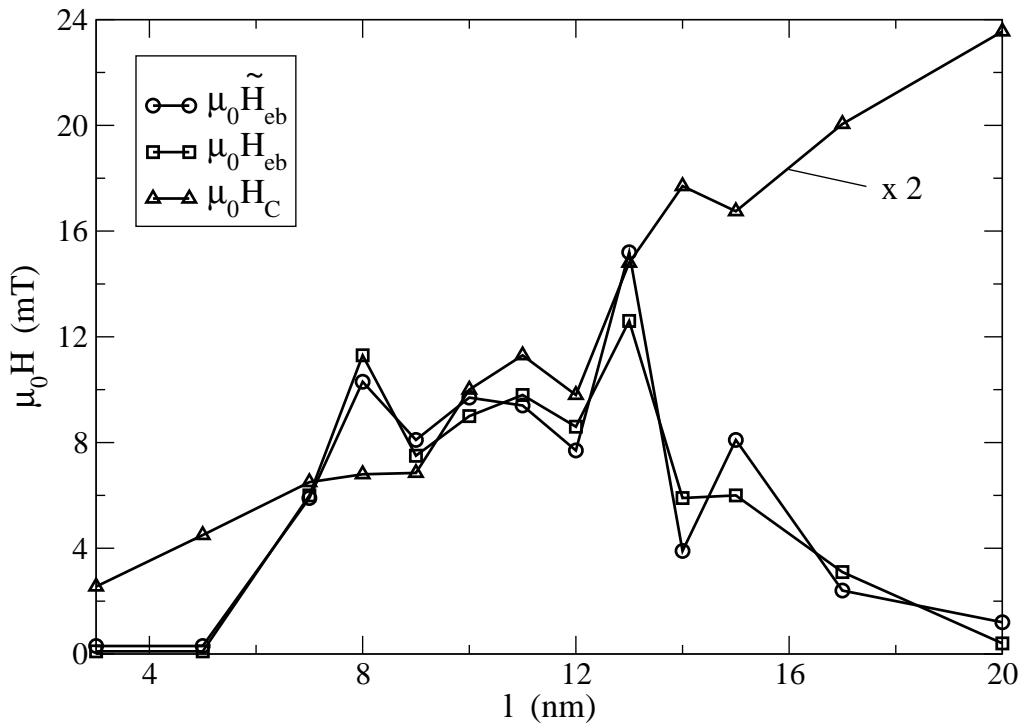


**Figure 4.36:** Dependence of  $H_{\text{eb}}$ ,  $\tilde{H}_{\text{eb}}$  and  $H_C$  on the grainsize  $l$ . The function of  $H_C$  times 2 gives the right coercive field. The behavior of  $H_C$  results from the anisotropy energy term. The bias field attains its broad maximum of about 9 mT on average between  $l \approx 7 - 13$  nm.

by randomly measuring a large number of crystallites ( $> 40$ ) from dark field Fresnel images. Since  $l$  plays an important role in all energy terms of Eq. (3.1) a rigorous explanation of the characteristics in Fig. 4.36 is not possible.

If one increases the grain size  $l$  one increases the antiferromagnetic anisotropy energy, the spin flop term and the Zeeman energy relatively to the exchange energy terms. Thus the increase of the coercive field can be explained analogously to Sec. 4.3.5. For  $l \gtrsim 15$  nm the percentage  $s$  of switched grains decreases rapidly ( $s = 20.7\%$  for  $l = 10$  nm,  $s = 10.4\%$  for  $l = 17$  nm), yielding a decreasing hysteresis shift. Although  $s$  increases with decreasing  $l$ , the ratio  $C/C_{\text{max}}$  remains almost constant ( $C/C_{\text{max}} \approx 22\%$ ). The energy difference  $\Delta E$  between the remanent states (stored in antiferromagnetic domain walls) decreases. Since  $\Delta E$  mainly influences the bias field, the hysteresis shift also falls off.

$360^\circ$  domain walls may occur for  $l \gtrsim 13$  nm, indicating that the ferromagnetic exchange energy is then weak enough relative to the antiferromagnetic anisotropy energy. Such stable configurations are the reason for the differences between  $H_{\text{eb}}$  and  $\tilde{H}_{\text{eb}}$  for  $l = 13, 14$  and  $15$  nm.

### 4.3.8 Remarks on the Antiferromagnetic Anisotropy

A comparison of Fig. 4.29, Fig. 4.34 and Fig. 4.36 clearly reveals a strong correlation between a variation of  $t_{\text{AF}}$ ,  $K_1$  and  $l$ . The energy term responsible for the observed similarity is the antiferromagnetic anisotropy term which mainly determines the behavior of the pinning layer and thus of the whole system.

The antiferromagnetic thickness also affects the antiferromagnetic exchange term. But the fact that  $H_C$  decreases with increasing  $A_{\text{AF}}$  is apparently eliminated or overlapped by the anisotropy term.

The grainsize  $l$  plays a role in all energy terms. The exchange energies depend linearly on  $l$  whereas the other terms in Eq. (3.1) vary with  $l^2$ . Since  $H_{\text{eb}}$  and  $H_C$  are not strongly affected by the interface coupling (see Fig. 4.35) and the Zeemann term only acts on the ferromagnet, a variation of  $l$  primarily influences the antiferromagnetic anisotropy.

## 4.4 Textured films

The results of the previous sections assumed a flat distribution of anisotropy axes over all possible orientations. This is not the best approximation of several experimental samples where the structure of granular materials may show on average a preferred orientation for antiferromagnetic crystalline axes. For example, King et al. [14] conclude from x-ray diffraction patterns taken on NiFe/IrMn bilayers that the granular IrMn layer is highly textured with the  $\langle 111 \rangle$  direction of the grains perpendicular to the interface. Fuke et al. [7] investigated IrMn single layer films deposited on thermally oxidized Si(100) substrates. The fcc IrMn film also showed a  $\langle 111 \rangle$  preferred orientation.

IrMn for exchange biased bilayer systems are used in the disordered fcc ( $\gamma$ ) phase [1] ( $T_N \approx 600 - 750$  K depending on at% Mn). The average spins on each (002) plane are aligned parallel along the c-axis with alternating signs on neighboring (002) planes. In terms of magnetic anisotropies, a  $\langle 111 \rangle$  texturing corresponds to an average angle  $\bar{\theta}$  between the easy axes and the interface normal of

$$\bar{\theta} = \arccos \frac{1}{\sqrt{3}} \approx 54.74^\circ \quad . \quad (4.21)$$

The problem at hand is to generate easy axes with the requested distribution on the surface of a sphere with the mean value of  $\bar{\theta}$ .

### 4.4.1 General Aspects of Arbitrarily Distributed Easy Axes

Easy directions are represented in spherical coordinates  $\theta \in [0, \pi]$  and  $\phi \in [0, 2\pi)$ . Fig. 4.37 depicts an unit sphere with surface elements  $\Delta A = \sin \theta \Delta \theta \Delta \phi$ . For randomly distributed easy axes in space surface elements that are equal in size have the same probability to contain easy axes. Since  $\Delta A$  varies with  $\sin \theta$  for constant  $\Delta \theta$  and  $\Delta \phi$  the distribution of the azimuth angle has to be uniform whereas the randomly chosen polar angle has to show a  $\sin \theta$  distribution in order to find easy axes actually random in space. For example Fig. 4.37 shows two surface elements  $\Delta A_1$  and  $\Delta A_2$  at  $\theta = \bar{\theta} \pm \xi$  with the same  $\Delta \theta$  and  $\Delta \phi$  but different sizes. In the  $(\theta, \phi)$ -diagram below they are represented by  $\Delta \tilde{A}_1$  and  $\Delta \tilde{A}_2$ , equal in size. That is, a uniform distribution of polar angles would not lead to a uniform distribution in space.

Now consider an arbitrary distribution function  $f(\theta)$  on the surface of the unit sphere with the symmetry condition  $f(\bar{\theta} + \xi) = f(\bar{\theta} - \xi)$ .  $f(\theta)\Delta A$  gives the number of easy axes within  $\Delta A$  at  $\theta$ . If  $\tilde{f}(\theta)$  denotes the distribution function in the two dimensional  $(\theta, \phi)$ -diagram, the relation

$$f(\theta)\Delta A = f(\theta) \sin \theta \Delta \theta \Delta \phi = \tilde{f}(\theta)\Delta \theta \Delta \phi = \tilde{f}(\theta)\Delta \tilde{A} \quad (4.22)$$

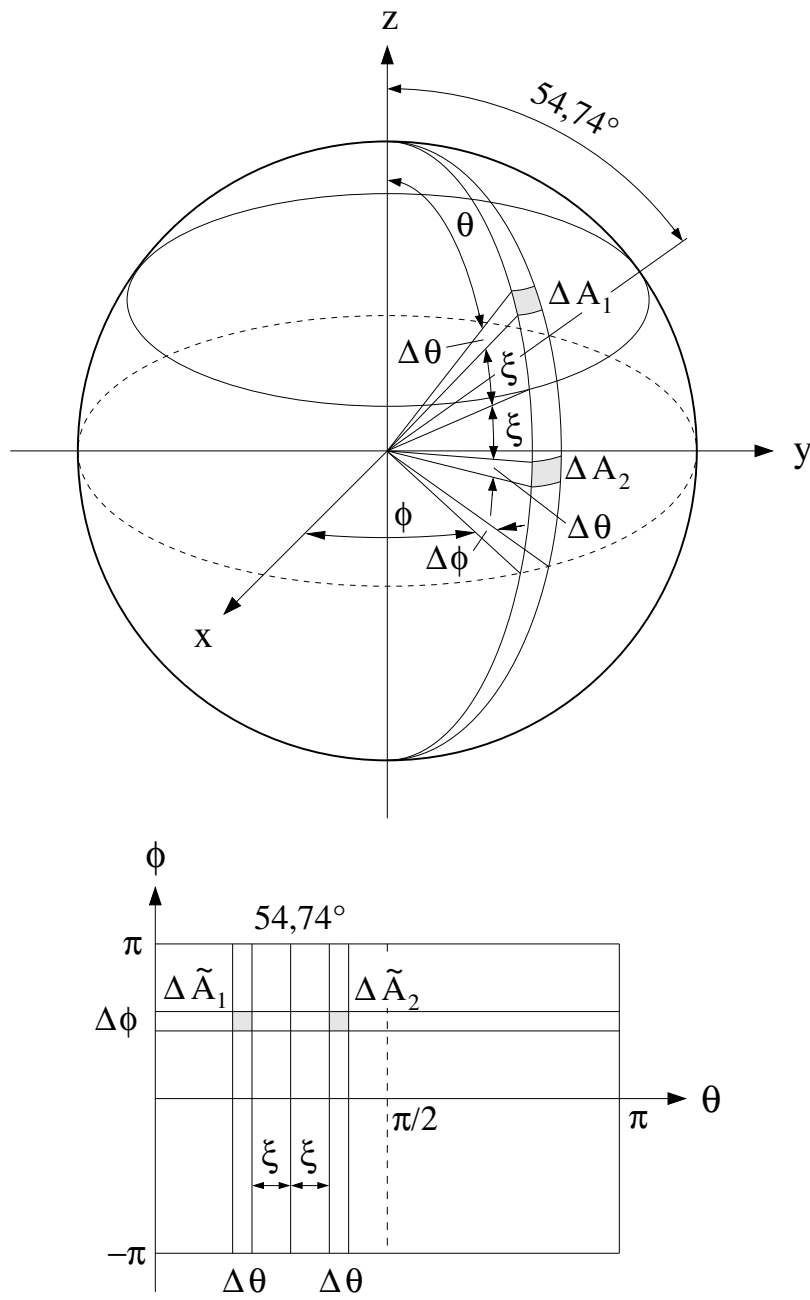


**Figure 4.37:** Unit sphere with surface elements  $\Delta A_1$  and  $\Delta A_2$  ( $\Delta A_2 > \Delta A_1$ ) symmetrically arranged at  $\bar{\theta} \approx 54.74^\circ$ . For given  $\Delta\theta$  and  $\Delta\phi$  the area of a surface element  $\Delta A$  varies with  $\sin\theta$ . In the  $(\theta, \phi)$ -diagram below the areas are represented by the equally sized elements  $\Delta \tilde{A}_1$  and  $\Delta \tilde{A}_2$ . Thus, for randomly oriented easy axes the probability for the polar angle  $\theta$  is  $\sin\theta$ .

must be fulfilled. Hence we get

$$\tilde{f}(\theta) = f(\theta) \sin\theta \quad , \quad (4.23)$$

i.e. to obtain the correct spatial distribution of the easy directions, the probability function

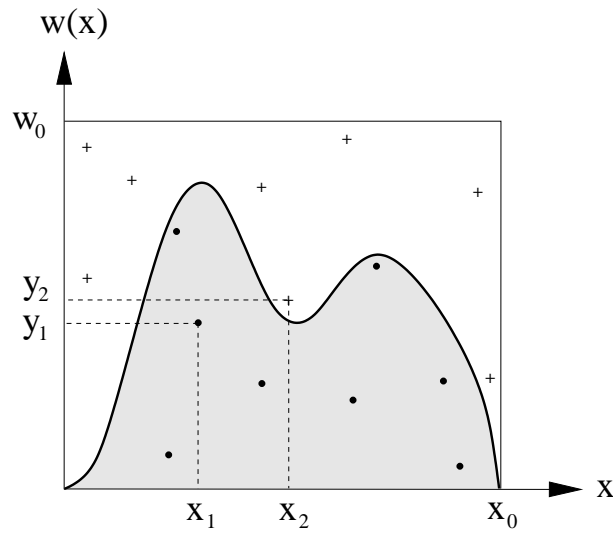


**Figure 4.38:** The von Neumann rejection method for generating random points  $x$  with the weight  $w(x)$ . According to the test (4.24) we accept  $x_1$  and reject  $x_2$ .

of the polar angle  $\theta$  must be  $\tilde{f}(\theta)$ . To originate  $\tilde{f}(\theta)$  we make use of the von Neumann rejection method.

### Rejection Method of von Neumann

Von Neumann introduced a simple method for generating random points with a probability distribution  $w(x)$  [18]. Suppose a graph of  $w(x)$  versus  $x$  within a box limited by a horizontal line at  $w_0$  and a vertical line at  $x_0$  as depicted in Fig. 4.38. The condition  $w_0 \geq w(x)$  for all values of  $x$  within the box must be fulfilled. Now we generate uniform distributions in  $x$  and  $y$  with the maximum  $y$  value equal to the height of the box  $w_0$  and make the following test for each pair  $(x_i, y_i)$ :

$$\begin{aligned} \text{if } y_i \leq w(x_i) & \dots \text{ accept } x_i, \\ \text{if } y_i > w(x_i) & \dots \text{ reject } x_i. \end{aligned} \tag{4.24}$$

The accepted  $x_i$  values will have the weighting  $w(x)$ .



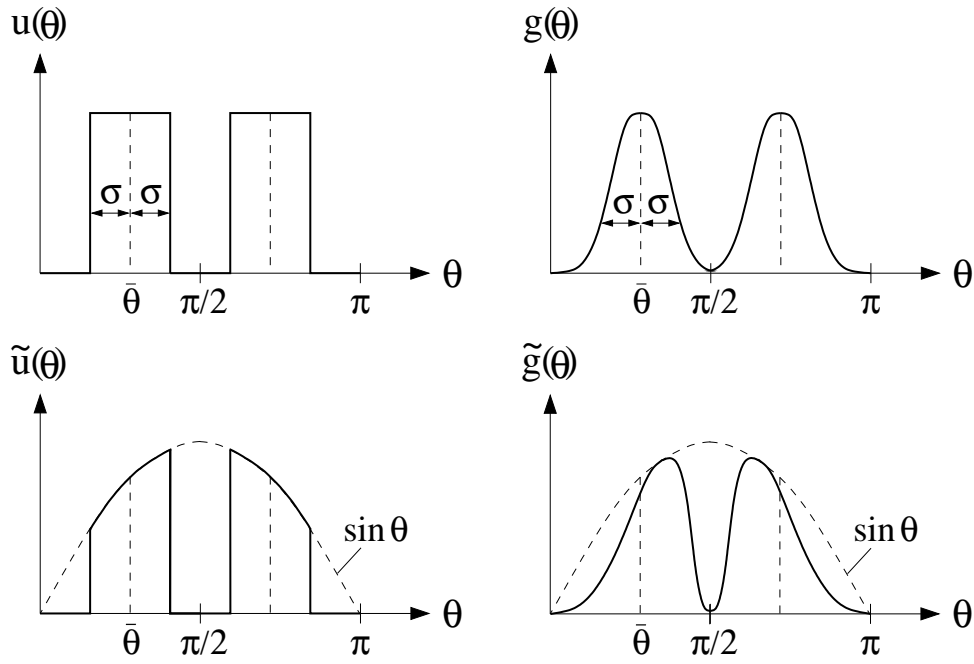


**Figure 4.39:** Above: Uniform ( $u(\theta)$ ) and Gaussian ( $g(\theta)$ ) distributions of the antiferromagnetic easy axes in space, symmetrically arranged about  $\pi/2$ . Below: Demanded distributions for the polar angle  $\theta$  according to Eq. (4.23).

#### 4.4.2 Uniform and Gaussian Distributions

Additionally to the totally random orientation of the easy axes we considered uniform ( $u(\theta)$ ) and Gaussian ( $g(\theta)$ ) distributions in space with the mean value  $\bar{\theta} \approx 54.74^\circ$  and standard deviation  $\sigma$  according to

$$u(\theta) = \frac{1}{2\sigma} \Theta_{-\sigma, \sigma}(\theta - \bar{\theta}) \quad , \quad (4.25)$$

$$g(\theta) = \frac{1}{\sqrt{2\pi}\sigma} \exp \left\{ -\frac{(\theta - \bar{\theta})^2}{2\sigma^2} \right\} \quad , \quad (4.26)$$

with the modified Heavyside function

$$\Theta_{a,b}(x) = \begin{cases} 1, & \text{for } a \leq x \leq b \\ 0, & \text{else.} \end{cases} \quad (4.27)$$

In order to improve the numerical behavior the directions  $\mathbf{k}_{\text{AF}}$  in Eq. (3.1) are chosen symmetrically around  $\theta = \pi/2$ . Fig. 4.39 illustrates the probability functions.  $\tilde{u}(\theta)$  and  $\tilde{g}(\theta)$  are calculated via Eq. (4.23). For  $\sigma \rightarrow \infty$  both functions converge to  $\sin \theta$ , i.e. to the fully random case.

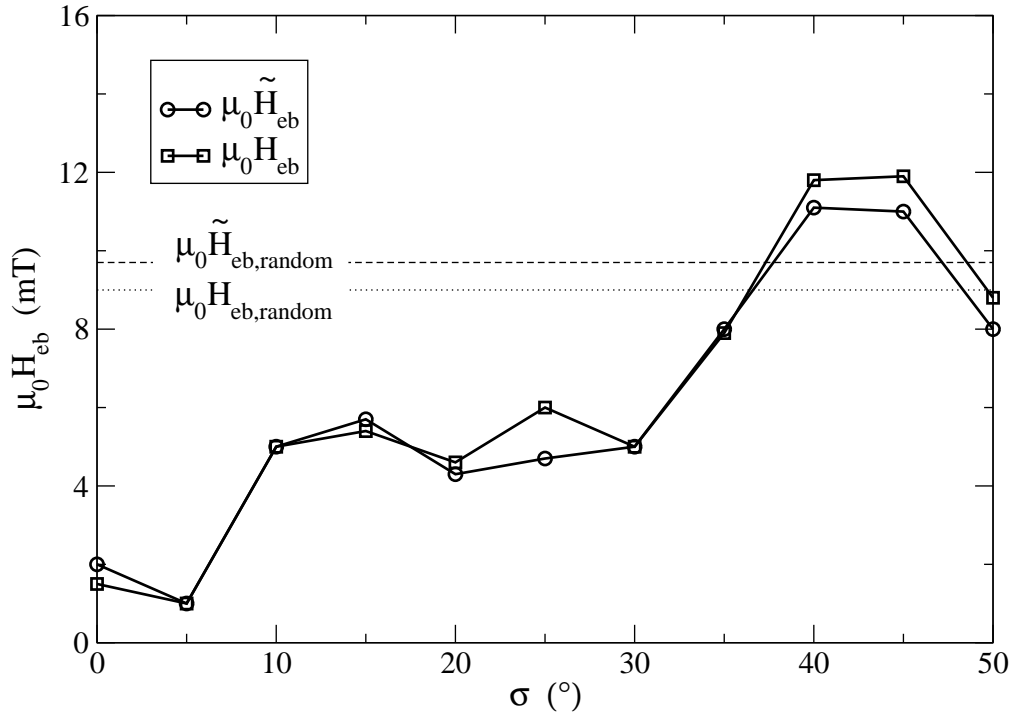


**Figure 4.40:**  $\mu_0 H_{eb}$  and  $\mu_0 \tilde{H}_{eb}$  for uniformly distributed easy axes versus the distribution width  $\sigma$  compared with the results for totally random oriented preferred directions (standard parameters and  $A_F = 0.5 \cdot 10^{-12}$  J/m).  $\sigma$  has to exceed  $\approx 35^\circ$  to provide enough easy directions nearly parallel to the film plane, resulting in high bias fields.

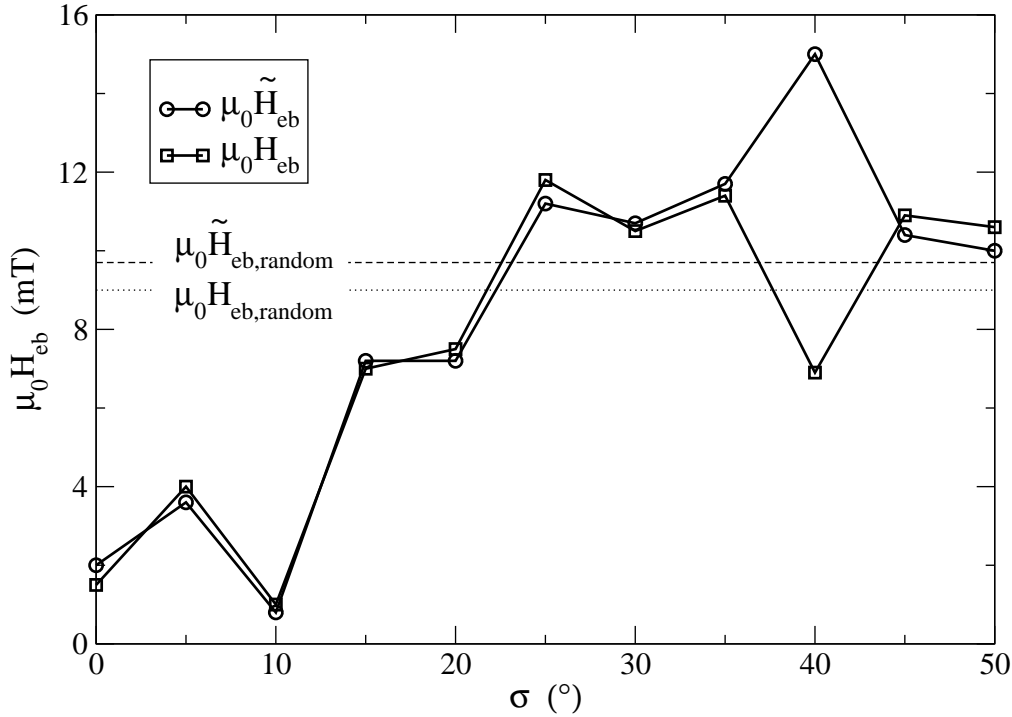


**Figure 4.41:** Dependence of  $\mu_0 H_{eb}$  and  $\mu_0 \tilde{H}_{eb}$  on the standard deviation  $\sigma$  for the Gaussian probability function (standard parameters and  $A_F = 0.5 \cdot 10^{-12}$  J/m). The shift of the hysteresis curve increases more rapidly with increasing  $\sigma$  than for the uniform distribution. At  $\sigma = 40^\circ$  the difference between  $\mu_0 H_{eb}$  and  $\mu_0 \tilde{H}_{eb}$  is considerably large due to stable  $360^\circ$  walls formed within the ferromagnet (see also Fig. 4.43 and Fig. 4.44).

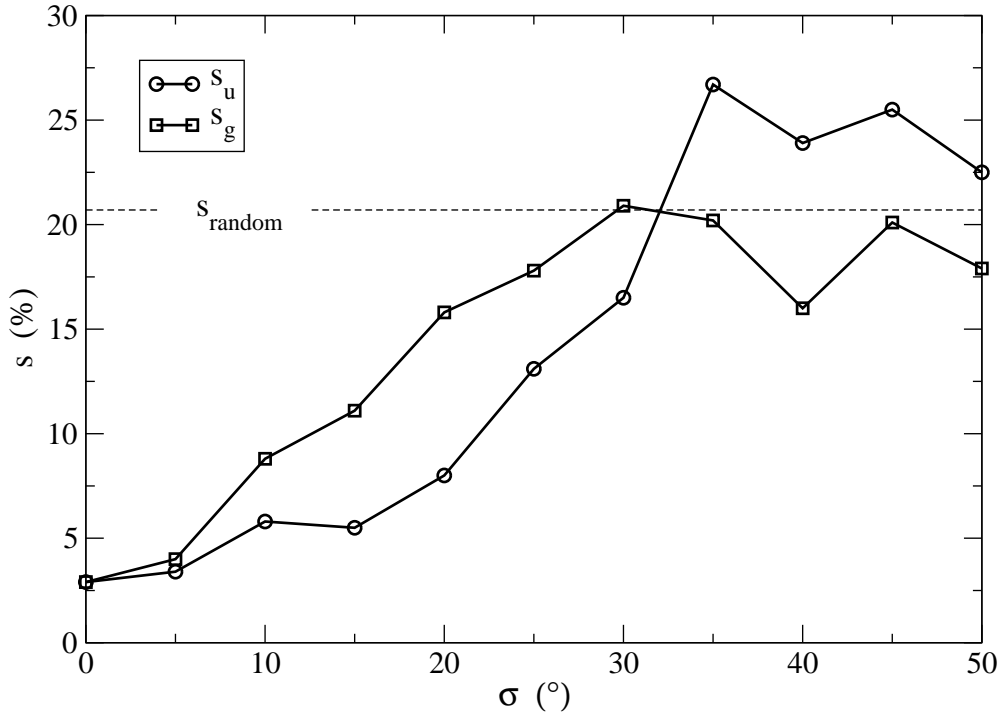


**Figure 4.42:** Dependence of  $s$  on  $\sigma$  for uniform and Gaussian probability functions compared with the percentage  $s_{\text{random}}$  obtained for fully randomly oriented axes (standard parameters and  $A_F = 0.5 \cdot 10^{-12}$  J/m).  $s_g$  increases more rapidly because the probability function is broader than for the uniform one. For  $\sigma \gtrsim 35^\circ$  we found  $s_u > s_g$  due to the fact that the uniform distribution function leads to more grains with easy directions almost in plane than the Gaussian probability function.

Fig. 4.40 gives the calculated bias fields for uniform distribution of the easy axes for different widths  $\sigma$  of the probability function. The results for Gaussian distributed preferred directions are shown in Fig. 4.41. We used the standard parameters and  $A_F = 0.5 \cdot 10^{-12}$  J/m.

The axes distribution has the largest effect on the bias field only when the spread in angles is small. The reason for this is that only the fraction of grains with easy axes relatively well aligned parallel to the interface contribute to exchange bias. In the uniform case the bias field is small in a wide range of  $\sigma$  compared to the random field  $H_{\text{eb,random}}$  because unless  $\sigma \approx 35^\circ$  no easy directions are parallel to the interface ( $\theta = 90^\circ$  means easy axis parallel to the film plane). For Gaussian distribution the bias field starts to increase already at about  $15^\circ$  due to  $\tilde{g}(\pi/2) > 0, \forall \sigma > 0$ .

In both cases easy directions almost perpendicular to the interface ( $\theta \approx 0$ ) are suppressed. Therefore the bias field for randomly distributed axes will in general be less than the bias fields for textured samples with all other factors being equal if the assumption of large

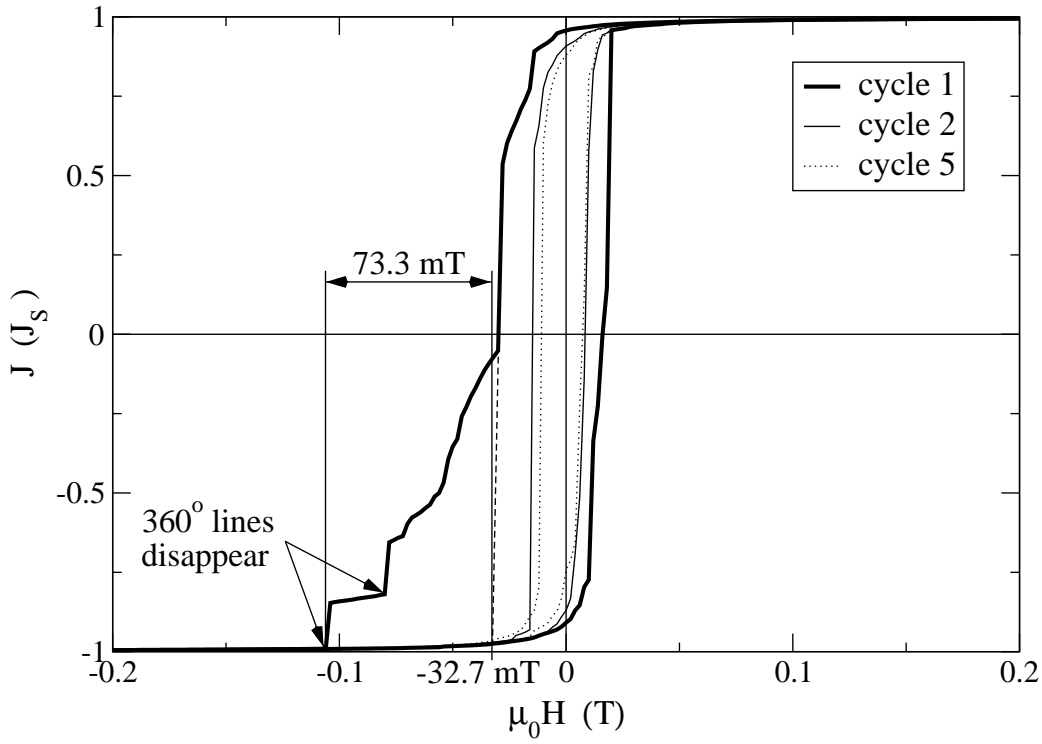


**Figure 4.43:** Hysteresis curves for Gaussian distribution and  $\sigma = 40^\circ$  (standard parameters and  $A_F = 0.5 \cdot 10^{-12}$  J/m). Two stable  $360^\circ$  lines lead to a huge deformation of the first hysteresis cycle in the third quadrant. At  $\mu_0 H = -80$  mT the first line disappears whereas the second remains up to  $\mu_0 H = -106$  mT (see Fig. 4.44).

standard deviations is fulfilled. It is relevant to note that the maximum bias field does not strongly depend on the shape of the probability function.

Fig. 4.42 shows the percentage  $s$  of switched grains, reflecting the characteristics of the bias fields. That is, the width  $\sigma$  of the distribution, the percentage  $s$  of switched grains and the bias shift are clearly correlated. In particular it shows that for  $\sigma \lesssim 30^\circ$  more grains switch irreversibly for the Gaussian distribution.  $C/C_{\max}$  behaves very similar and is therefore omitted.

Contrary to the bias field, the coercive field is not strongly affected by the width of the probability functions and fluctuates almost independently of  $\sigma$  between 15 and 25 mT. Irreversible switching in the antiferromagnet is necessary for bias field formation. Coercivity observed through the ferromagnet may be enhanced by irreversible switching in the antiferromagnet, but ferromagnetic coercivity may also exist independently.

The large difference between  $\mu_0 H_{\text{eb}} = 6.9$  mT and  $\mu_0 \tilde{H}_{\text{eb}} = 15.0$  mT for Gaussian distribution and  $\sigma = 40^\circ$  (see Fig. 4.41) results from extremely stable  $360^\circ$  walls formed in the ferromagnet. Fig. 4.43 shows the hysteresis curve which exhibits a huge deformation in

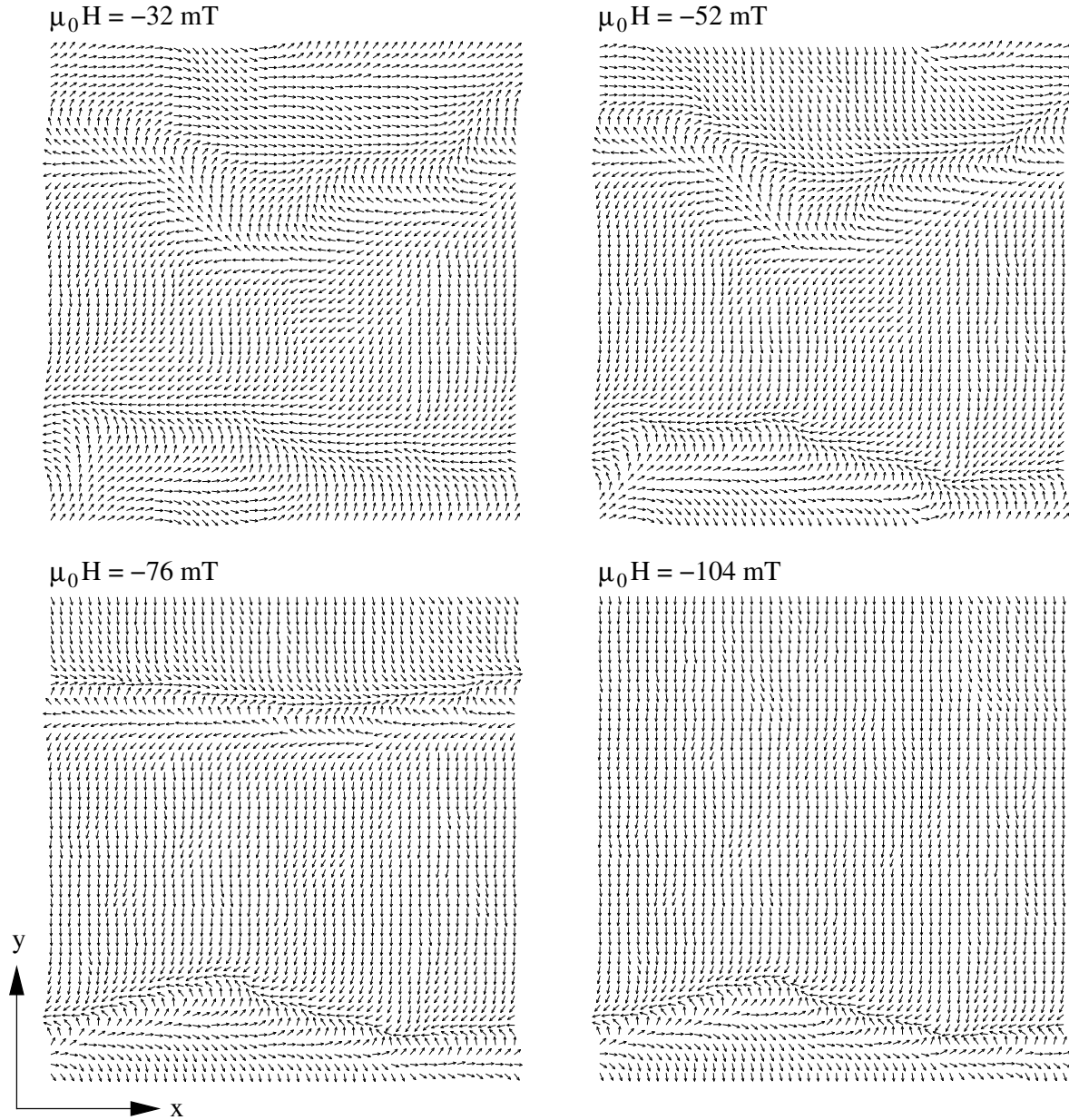


**Figure 4.44:** An image sequence of the formation and disappearance of two extremely stable  $360^\circ$  lines for Gaussian distribution and  $\sigma = 40^\circ$  (standard parameters and  $A_F = 0.5 \cdot 10^{-12} \text{ J/m}$ ). The first line disappeared at  $-80 \text{ mT}$ , the second at  $-106 \text{ mT}$ .

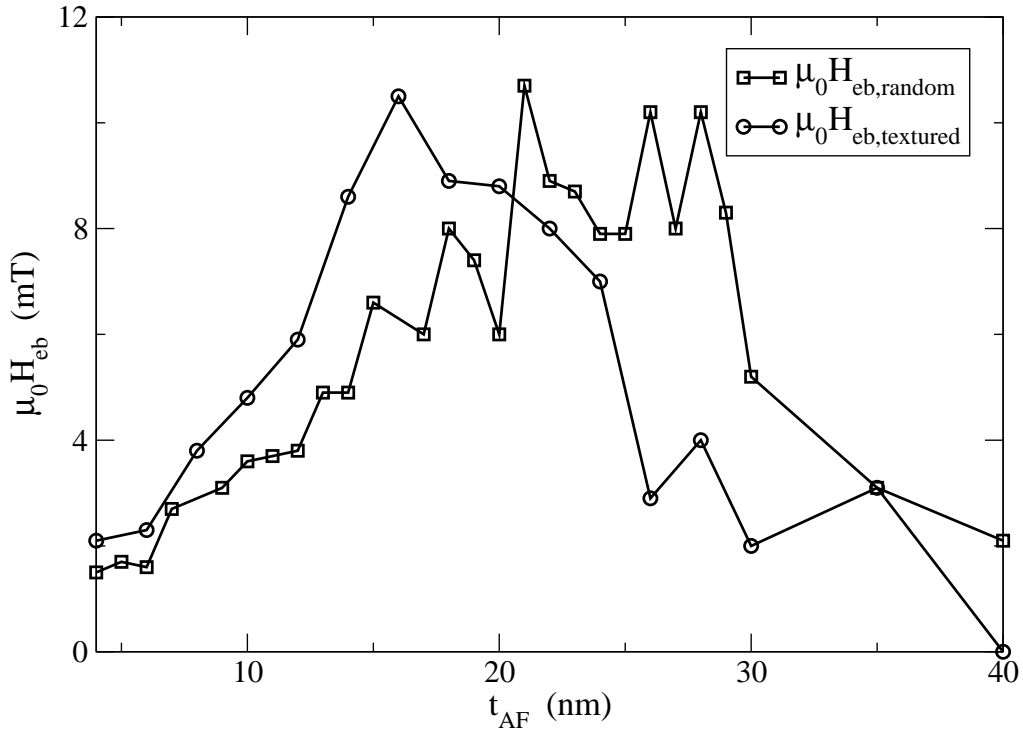


**Figure 4.45:** Exchange bias field as a function of  $t_{AF}$  for textured and untextured films. A Gaussian distribution of the antiferromagnetic easy directions with  $\sigma = 20^\circ$  was used to mimic the textured pinning layer. The maximum clearly shifts towards lower thicknesses for textured films. Namely from between 22 and 28 nm for the untextured film to 16 nm for the textured layer.

the third quadrant due to stable configurations, leading to a three times larger external field ( $-106$  mT) required to saturate the ferromagnet.

Fig. 4.44 presents an image sequence of these stable  $360^\circ$  lines parallel to the x-axis. The upper line disappears at  $\mu_0 H = -80$  mT yielding the first distinct step in the hysteresis curve. An external field of  $\mu_0 H = -160$  mT also annihilates the lower line and saturates the ferromagnetic layer, indicated by the second step in the hysteresis cycle.

### Texture and Antiferromagnetic Thickness

Van Driel et al. [38] explored antiferromagnetic/ferromagnetic bilayers of  $\text{Ir}_{19}\text{Mn}_{81}$  and  $\text{Ni}_{80}\text{Fe}_{20}$  or  $\text{Co}_{90}\text{Fe}_{10}$ , respectively. The exchange bias field was found to depend strongly on the degree of the crystallographic  $\langle 111 \rangle$  texture of the bilayer system. Ta was used as a seed layer to induce  $\langle 111 \rangle$  texture in the antiferromagnetic film, analyzed with TEM. They obtained a shifted maximum of the bias field for textured films as a function of the antiferromagnetic thickness  $t_{AF}$  towards lower thicknesses. A strong similarity was found between the behavior of the  $\langle 111 \rangle$  texture and the bias field as a function of the

antiferromagnetic thickness.

We performed simulations for the standard parameters and Gaussian distribution with  $\sigma = 10^\circ$  and  $\sigma = 20^\circ$ , respectively. However, the bias fields for  $\sigma = 10^\circ$  were too small to point out a tendency of the maximum. Fig. 4.45 thus only shows the results for  $\sigma = 20^\circ$  and untextured films (taken from Fig. 4.29). In fact the textured curve is shifted towards lower  $t_{AF}$ . The maximum for untextured films lies somewhere between 22 and 28 nm whereas the bias field for textured films attains its maximum for  $t_{AF} \approx 16$  nm. That is, the results of our IG model for textured films agree considerably well with experimental observations.

### Positive Exchange Bias

In several simulations the direction of the hysteresis shift depends on the cycle number. For example for Gaussian distribution and  $\sigma = 15^\circ$  ( $A_F = 0.5 \cdot 10^{-12}$  J/m) we found  $\mu_0 H_{eb} = 7$  mT ( $\mu_0 \tilde{H}_{eb} = 7.2$  mT) for the first cycle and  $\mu_0 H_{eb} = \overline{1.9}$  mT ( $\mu_0 \tilde{H}_{eb} = \overline{1.2}$  mT) for the third one although the energy difference  $\Delta E_{\text{tot}, \bar{R}_3 - R_3}$  was still positive. This is an impressive argument of our statement that the knowledge of the energy difference between the remanent states is not sufficient to explain or calculate exchange bias.

Moreover, some simulations lead to negative (i.e. normal) bias fields  $H_{eb}$  but positive  $\tilde{H}_{eb}$ . For instance, for Gaussian distribution and  $\sigma = 20^\circ$  we found for the standard parameters and  $t_{AF} = 2$  nm  $\mu_0 H_{eb} = 0.8$  mT and  $\mu_0 \tilde{H}_{eb} = \overline{0.1}$  mT. The hysteresis curve for this set of parameters is quite narrow and thus extremely sensitive to small variations of the ferromagnetic domain structure.

# Outlook

The influence of finite temperatures on the exchange bias field and the coercivity has not been investigated yet. One of the problems will be that the hysteresis curve depends on the waiting time in the reversed state when the temperature is taken into account.

Our simulations assumed periodic boundary conditions. Experiments show that the magnetization configuration and the hysteresis curve depend on the shape and the size of the bilayer system due to strayfield minimization. Thus, it would be interesting to perform simulations for more realistic boundaries of the bilayer system.

Up to now only a uniaxial anisotropy was considered. It remains to be seen how cubic anisotropy affects the switching behavior and the shift of the hysteresis loop.



# List of Figures

|      |  |    |
|------|--|----|
| 1    | Schematic illustration of a GMR spin-valve head . . . . .  | 9  |
| 1.1  | Illustration of the LLG equation . . . . .   | 16 |
| 2.1  | Experimental characteristics of exchange biased systems . . . . .                                    | 19 |
| 2.2  | Intuitive picture of Meiklejohn and Bean . . . . .   | 21 |
| 2.3  | Domain wall model of Mauri . . . . .   | 23 |
| 2.4  | Koon's spin flop coupling . . . . .  | 25 |
| 2.5  | Polycrystalline model of Stiles and McMichael . . . . .  | 27 |
| 3.1  | Origin of exchange bias in the IG model . . . . .  | 30 |
| 3.2  | Simulation of $3 \times 3$ grains . . . . .  | 32 |
| 3.3  | Geometry of the IG model . . . . .   | 33 |
| 4.1  | Important points of the hysteresis cycle . . . . .   | 40 |
| 4.2  | Difference between reversible and irreversible switching . . . . .                                   | 40 |
| 4.3  | Circumference of switched areas . . . . .  | 41 |
| 4.4  | Total work $A_{1 \rightarrow 2}$ to change the polarization from $J_1$ to $J_2$ . . . . .            | 42 |
| 4.5  | Hysteresis cycles of unbiased and biased ferromagnetic layer . . . . .                               | 43 |
| 4.6  | Schematic illustration of the calculation of $\tilde{H}_{\text{eb}}$ . . . . .                       | 44 |
| 4.7  | Hysteresis curves for the standard parameters . . . . .  | 45 |
| 4.8  | Characteristic fields versus cycle number $n$ . . . . .  | 46 |
| 4.9  | Switched antiferromagnetic grains . . . . .  | 48 |
| 4.10 | Exchange energy of the ferromagnet . . . . .   | 49 |
| 4.11 | Exchange energy of the antiferromagnet . . . . .   | 49 |
| 4.12 | Spin flop energy . . . . .   | 50 |
| 4.13 | Anisotropy energy of the antiferromagnet . . . . .   | 50 |
| 4.14 | Total energy . . . . .   | 51 |
| 4.15 | Ferromagnetic spin configuration in the positive remanent state . . . . .                            | 52 |
| 4.16 | Ferro- and antiferromagnetic domains . . . . .   | 55 |
| 4.17 | Antiferromagnetic domains . . . . .  | 56 |
| 4.18 | $H_{\text{eb}}$ , $\tilde{H}_{\text{eb}}$ and $H_{\text{C}}$ as function of $A_{\text{F}}$ . . . . . | 57 |

|      |   |    |
|------|---|----|
| 4.19 | Domain structure of the ferromagnet in the remanent state . . . . .   | 58 |
| 4.20 | 360° wall loops [14] . . . . .  | 59 |
| 4.21 | Hysteresis loops for $A_F = 0.3 \cdot 10^{-12}$ J/m . . . . .   | 60 |
| 4.22 | Image sequence of a 360° wall loop . . . . .  | 61 |
| 4.23 | $H_{\text{eb}}$ , $\tilde{H}_{\text{eb}}$ and $H_C$ as function of $t_F$ . . . . .                                    | 62 |
| 4.24 | Comparison of $H_{\text{eb}}$ and $H_C$ with $H_{\text{eb,cal}}$ and $H_{C,\text{cal}}$ as function of $t_F$ . . . .  | 63 |
| 4.25 | Stable 360° loop for $t_F = 4$ nm . . . . .   | 65 |
| 4.26 | $H_{\text{eb}}$ , $\tilde{H}_{\text{eb}}$ and $H_C$ as function of $A_{\text{AF}}$ . . . . .                          | 66 |
| 4.27 | $s$ and $C/C_{\text{max}}$ as a function of $A_{\text{AF}}$ . . . . .   | 67 |
| 4.28 | Magnetization configuration in the antiferromagnet for different $A_{\text{AF}}$ . . . .                              | 68 |
| 4.29 | $H_{\text{eb}}$ , $\tilde{H}_{\text{eb}}$ and $H_C$ as function of $t_{\text{AF}}$ . . . . .                          | 69 |
| 4.30 | Two antiferromagnetic grains with parallel easy axes . . . . .  | 70 |
| 4.31 | $C/C_{\text{max}}$ and $s$ versus $t_{\text{AF}}$ . . . . .   | 72 |
| 4.32 | Comparison of $\mu_0 H_{\text{eb}}$ with $\mu_0 H_{\text{eb,cal}}$ as function of $t_{\text{AF}}$ . . . . .           | 72 |
| 4.33 | $s$ and $C/C_{\text{max}}$ as function of $K_1$ . . . . .   | 73 |
| 4.34 | $H_{\text{eb}}$ , $\tilde{H}_{\text{eb}}$ and $H_C$ as function of $K_1$ . . . . .                                    | 74 |
| 4.35 | $H_{\text{eb}}$ , $\tilde{H}_{\text{eb}}$ and $H_C$ as function of $-A_{\text{AF}-F}$ . . . . .                       | 75 |
| 4.36 | $H_{\text{eb}}$ , $\tilde{H}_{\text{eb}}$ and $H_C$ as function of $l$ . . . . .                                      | 76 |
| 4.37 | Unit sphere with surface elements and $(\theta, \phi)$ -diagram . . . . .   | 79 |
| 4.38 | Von Neumann rejection method . . . . .  | 80 |
| 4.39 | Uniform and Gaussian distributions of the easy axes . . . . .   | 81 |
| 4.40 | $\mu_0 H_{\text{eb}}$ and $\mu_0 \tilde{H}_{\text{eb}}$ for uniformly distributed easy axes versus $\sigma$ . . . . . | 82 |
| 4.41 | $\mu_0 H_{\text{eb}}$ and $\mu_0 \tilde{H}_{\text{eb}}$ for Gaussian distribution versus $\sigma$ . . . . .           | 82 |
| 4.42 | $s$ as a function of $\sigma$ for uniform and Gaussian probability functions . . . .                                  | 83 |
| 4.43 | Hysteresis curves for Gaussian distribution and $\sigma = 40^\circ$ . . . . .   | 84 |
| 4.44 | Image sequence of 360° lines for Gaussian distribution . . . . .  | 85 |
| 4.45 | $\mu_0 H_{\text{eb}}$ as a function of $t_{\text{AF}}$ for textured and untextured films . . . . .                    | 86 |

# Bibliography

- [1] **A.E. Berkowitz, K. Takano**, “Exchange anisotropy – a review”, J. Magn. Magn. Mater., vol. 200, p. 552, 1999
- [2] **G. Bertotti**, “Hysteresis in Magnetism”, Academic Press, San Diego, 1998
- [3] **W.F. Brown**, “Micromagnetics”, Interscience Publishers, 1963
- [4] **S.D. Cohen, A.C. Hindmarsh**, “CVODE User Guide”, Lawrence Livermore National Laboratory report UCRL-MA-118618, 1994
- [5] **S.D. Cohen, A.C. Hindmarsh**, “CVODE, a Stiff/Nonstiff ODE Solver in C”, Computers in Physics, vol. 10, p. 138, 1996
- [6] **H. Fujiwara, K. Zhang, T. Kai, T. Zhao**, “Effect of direct exchange coupling between antiferromagnetic grains on magnetic behavior of ferro/antiferromagnetic exchange coupled polycrystalline layer systems”, J. Magn. Magn. Mater., vol. 235, p. 319, 2001
- [7] **H.N. Fuke, K. Saito, Y. Kamiguchi, H. Iwasaki and M. Sahashi**, “Spin-valve giant magnetoresistive films with antiferromagnetic Ir-Mn layers”, J. Appl. Phys., vol. 81, p. 4004, 1997
- [8] **P. Gogol, J.N. Chapman, M.F. Gillies, F.W.M. Vanhelmont**, “Domain processes in the magnetisation reversal of exchange-biased IrMn/CoFe bilayers”, J. Appl. Phys., vol. 92, p. 1458, 2002
- [9] **A.C. Hindmarsh, L.R. Petzold**, “Algorithms and Software for Ordinary Differential Equations and Differential-Algebraic Equations”, Computers in Physics, vol. 9, p. 34 and p. 148, 1995
- [10] **D. Hinzke and U. Nowak**, “Magnetization switching in a Heisenberg model for small ferromagnetic particles”, Phys. Rev. B, vol. 58, pp. 265, 1998
- [11] **Y. Iriji, J.A. Borchers, R.W. Erwin, S.H. Lee, P.J. van der Zaag, R.M. Wolf**, “Perpendicular coupling in exchange-biased  $\text{Fe}_3\text{O}_4/\text{CoO}$  superlattices”, Phys. Rev. Lett., vol. 80, p. 608, 1998

- [12] **H. Kanai, K. Noma, J. Hong**, “Advanced Spin-Valve GMR Head”, FUJITSU Sci. Tech. J., vol. 37, p. 174, 2001
- [13] **J.V Kim, R.L. Stamps, B.V. McGrath and R.E. Camley**, “Angular dependence and interfacial roughness in exchange-biased ferromagnetic/antiferromagnetic bilayers”, Phys. Rev. B, vol. 61, p. 8888, 2000
- [14] **J.P. King, J.N. Chapman, M.F. Gillies and J.C.S. Kools**, “Magnetization reversal of NiFe films exchange-biased by IrMn and FeMn”, J. Phys. D: Appl. Phys., vol. 34, p. 528, 2001
- [15] **E. Kneller**, “Ferromagnetismus”, Springer-Verlag, Berlin/Göttingen/Heidelberg, 1962
- [16] **N.C. Koon**, “Calculations of Exchange Bias in Thin Films with Ferromagnetic/Antiferromagnetic Interfaces”, Phys. Rev. Lett., vol. 78, p. 4865, 1997
- [17] **H. Kronmüller**, “Magnetische Eigenschaften fester Körper”, lecture notes, Inst. f. Theoretische u. Angewandte Physik der Universität Stuttgart und Inst. f. Physik am Max-Planck-Institut f. Metallforschung, 1988
- [18] **R.H. Landau, M.J. Páez**, “Computational Physics”, John Wiley & Sons, New York, 1997
- [19] **A.P. Malozemoff**, “Mechanism of exchange anisotropy”, J. Appl. Phys., vol. 63, p. 3874, 1988
- [20] **D. Mauri, H.C. Siegmann, P.S. Bagus und E. Kay**, “Simple model for thin ferromagnetic films exchange coupled to an antiferromagnetic substrate”, J. Appl. Phys., vol. 62, p. 3047, 1987
- [21] **W.H. Meiklejohn and C.P. Bean**, “New magnetic anisotropy”, Phys. Rev., vol. 102, p. 1413, 1956
- [22] **W.H. Meiklejohn and C.P. Bean**, “New magnetic anisotropy”, Phys. Rev., vol. 105, p. 904, 1957
- [23] **W.H. Meiklejohn**, “Exchange Bias – A review”, J. Appl. Phys., vol. 33, p. 1328, 1962
- [24] **P. Miltényi**, “Mikroskopischer Ursprung der Austauschkopplung in ferromagnetischen/antiferromagnetischen Schichten”, Dissertation, Fakultät für Mathematik, Informatik und Naturwissenschaften, Technische Hochschule Aachen, 2000

- [25] **J. Nogués, D. Lederman, T. J. Moran and Ivan K. Schuller**, “Large exchange bias and its connection to interface structure in FeF<sub>2</sub>-Fe bilayers”, Appl. Phys. Lett., vol. 68, p. 3186, 1996
- [26] **J. Nogués, D. Ledermann, T.J. Moran and Ivan K. Schuller**, “Positive Exchange Bias in FeF<sub>2</sub>-Fe Bilayers”, Phys. Rev. Lett., vol. 76, pp. 4624, 1996
- [27] **J. Nogués, I.K. Schuller**, “Exchange bias”, J. Magn. Magn. Mater., vol. 192, p. 203, 1999
- [28] **U. Nowak, A. Misra and K.D. Usadel**, “Domain state model for exchange bias”, J. Appl. Phys., vol. 89, p. 7269, 2001
- [29] **T.C. Schulthess and W.H. Butler**, “Consequences of spin-flop coupling in exchange biased films”, Phys. Rev. Lett., vol. 81, p. 4516, 1998
- [30] **R.L. Stamps**, “Mechanisms for exchange bias”, J. Phys. D: Appl. Phys., vol. 33, p. 247, 2000
- [31] **M.D. Stiles and R.D. McMichael**, “Model for exchange bias in polycrystalline ferromagnet-antiferromagnet bilayers”, Phys. Rev. B, vol. 59, pp. 3722, 1999
- [32] **M.D. Stiles and R.D. McMichael**, “Coercivity in exchange-bias bilayers”, Phys. Rev. B, vol. 63, p. 64405, 2001
- [33] **D. Suess**, “Micromagnetic simulations of antiferro- and ferromagnetic structures for magnetic recording”, Dissertation, Fakultät für Naturwissenschaften und Informatik, Technische Universität Wien, 2002
- [34] **D. Suess, V. Tsiantos, T. Schrefl, J. Fidler, W. Scholz, H. Forster, R. Dittrich, J.J. Miles**, “Time resolved micromagnetics using a preconditioned time integration method”, J. Magn. Magn. Mater., vol. 248, p. 298, 2002
- [35] **D. Suess, R. L. Stamps, T. Schrefl, J. V. Kim, J. Fidler**, “Exchange bias of polycrystalline antiferromagnets with perfectly compensated interface”, Phys. Rev. B, submitted
- [36] **D. Suess, T. Schrefl, W. Scholz, J. V. Kim, R. L. Stamps, J. Fidler**, “Micromagnetic simulation of antiferromagnetic/ferromagnetic structures”, IEEE Trans. Magn., vol. 38, p. 2520, 2002
- [37] **V.D. Tsiantos, T. Schrefl, J. Fidler, A. Bratsos**, “Cost-Effective Way to Speed-up Micromagnetic Simulations in Granular media”, Appl. Num. Math., vol. 39, p. 191, 2001

- [38] **J. van Driel, F.R. de Boer, K.-M.H. Lenssen and R. Coehoorn**, “Exchange biasing by  $\text{Ir}_{19}\text{Mn}_{81}$ : Dependence on temperature, microstructure and antiferromagnetic layer thickness”, J. Appl. Phys., vol. 88, p. 975, 2000

**Parts of this work have been published:**

- [39] **M. Kirschner, D. Suess, T. Schrefl, J. Fidler, R.L. Stamps, J.V. Kim**, “Exchange Bias and Training Effect in Polycrystalline Antiferromagnetic/Ferromagnetic Bilayers”, MRS Fall Meeting 2002, Boston/USA, Proceedings, in press
- [40] **M. Kirschner, D. Suess, T. Schrefl, J. Fidler, J.N. Chapman**, “Micromagnetic calculation of bias field and coercivity of exchange biased  $\text{IrMn}/\text{NiFe}$  bilayers”, Intermag 2003, Boston/USA, GU-03, IEEE Trans. Magn., submitted
- [41] **D. Suess, M. Kirschner, T. Schrefl, J. Fidler, R.L. Stamps and J.V. Kim**, “Exchange bias of polycrystalline antiferromagnets with perfectly compensated interface”, Phys. Rev. B, in press
- [42] **D. Suess, M. Kirschner, T. Schrefl, W. Scholz, R. Dittrich, H. Forster, J. Fidler**, “Micromagnetic calculations of bias field and coercivity of compensated ferromagnetic/antiferromagnetic bilayers”, MMM 2002, Tampa/USA, HE-14, J. Appl. Phys., in press

# Lebenslauf

Markus Kirschner  
Angergasse 61  
A-7123 Mönchhof

|                    |   |
|--------------------|---|
| Geburtsdatum       | 22. Februar 1975                              |
| Geburtsort         | Mönchhof                                      |
| Eltern             | Annemarie und Josef Kirschner                 |
| Staatsbürgerschaft | Österreich                                    |
| 1981 – 1985        | Volksschule in Mönchhof                       |
| 1985 – 1989        | Hauptschule in Gols                           |
| 1989 – 1994        | HTL für Feinwerktechnik in Mödling            |
| 1994 – 1995        | Präsenzdienst in Bruckneudorf                 |
| ab Okt. 1995       | Studium der Technischen Physik an der TU Wien |
| Februar 2003       | Einreichung der 2. Diplomprüfung              |